NAL PROPOSAL NO. 164 I & II

Scientific Spokesman:
Z. G. T. Guiragossian
High Energy Physics Laboratory
W. W. Hansen Laboratories of Physics
Stanford University
Stanford, California 94305

Telephone:
(415) 327-7800, extension 333

PROPOSAL
TO STUDY AT NAL ENERGIES
I. MULTI-GAMMA-RAY FINAL STATES USING A NEGATIVE BEAM ON HYDROGEN, Cu and Pb TARGETS
II. DEEP INELASTIC ELECTRON SCATTERING WITH A SEARCH FOR MASSIVE LEPTONS AND QUARKS, ON HYDROGEN, DEUTERIUM, Cu AND Pb TARGETS

J. F. Crawford, Z. G. T. Guiragossian, R. Hofstadter, E. B. Hughes
R. E. Rand, R. F. Schilling and M. R. Yearian

The W. W. Hansen High Energy Physics Laboratory and
Department of Physics
Stanford University, Stanford, California 94305

E. V. Hungerford III, G. S. Mutchler, G. C. Phillips
The T. W. Bonner Nuclear Laboratories and Department of Physics
Rice University, Houston, Texas 77001

B. W. Mayes
Department of Physics
The University of Houston
Houston, Texas 77001

December 1971

NAL PROPOSAL NO.

Scientific Spokesman: Z. G. T. Guiragossián
High Energy Physics Laboratory
W. W. Hansen Laboratories of Physics
Stanford University
Stanford, California 94305
Telephone: (415) 327-7800, extension 333

PROPOSAL
TO STUDY AT NAL ENERGIES
I. MULTI-GAMMA-RAY FINAL STATES USING A NEGATIVE BEAM ON HYDROGEN, Cu and Pb TARGETS
II. DEEP INELASTIC ELECTRON SCATTERING WITH A SEARCH FOR MASSIVE LEPTONS AND QUARKS, ON HYDROGEN, DEUTERIUM, Cu AND Pb TARGETS

Submitted by

J. F. Crawford, Z. G. T. Guiragossián, R. Hofstadter, E. B. Hughes
R. E. Rand, R. F. Schilling and M. R. Yearian
The W. W. Hansen/High Energy Physics Laboratory, and
Department of Physics
Stanford University, Stanford, California 94305

and

E. V. Hungerford III, G. S. Mutchler, G. C. Phillips
The T. W. Bonner Nuclear Laboratories, and Department of Physics
Rice University, Houston, Texas 77001

and

B. W. Mayes
Department of Physics
The University of Houston
Houston, Texas 77001

December 1971

CONTENTS

CONTENTS (Cont'd.)

I. PROPOSAL TO STUDY MULTI-GAMMA-RAY FINAL STATES AT NAL ENERGIES, USING A NEGATIVE BEAM ON HYDROGEN, Cu and Pb TARGETS

We propose to utilize an accurate, large acceptance and highly efficient multi-gamma-ray spectrometer system to search for the existence of massive bosons with a mass resolution of $|\Delta M/M| < 2\%$. We also propose to measure the production differential cross sections of such bosons with a momentum transfer resolution which is five times better than expressed in any previous experiment of this type or proposal with which we are familiar. Our experiment is designed to reveal new knowledge both in the states of particle physics and in the exploration of new interaction dynamical phenomena.

Our detection system is based upon the successes derived from a recent development program at HEPL, in the design, fabrication and testing of large NaI(Tl) crystal total absorption (TASC) counters. The experimental method is described in Section B. Briefly, in the proposed experiment, beyond a beam clearing magnet having a matched acceptance, we plan to use these TASC-counters in combination with multi-wire proportional counter planes. In an arrangement where "live" radiators are used for gamma-to-shower conversion, we record the spatial coordinates of the gamma directions with corresponding spatial accuracy of $\pm$ 1.0 mm, measure the energy partition among individual gamma-rays in a system, with an accuracy of $\frac{\Delta E_i}{E_i} \simeq \pm 15\%$, as limited by shower development fluctuations, and measure the total energy of the multi-gamma-ray final state with an accuracy of about $\frac{\Delta E_o}{E_o} = \pm 0.5\%$. The most stringent feature of this spectrometer system lies in the ability to measure the total multi-gamma-ray energy with the stated very sharp energy resolution. Using electron beams having energies up to 15 GeV this expectation has been realized by tests at the SLAC accelerator, and at lower energies at the HEPL Mark III accelerator.[1]

Our experimental conditions are set to trigger on about 1% of the overall beam interactions in the target. Among the interactions of the type:

$$\pi^- p \rightarrow X^o(MM) \qquad (1)$$

where X^o is a multi-gamma-ray system, we expect to collect typically 500-1000 events/machine pulse, during a long beam spill.

Our triggering conditions are defined with the help of veto thin scintillators and veto shower counters surrounding the target. These are used to suppress the production of charged particles or π^o's at large angles. In the case of a hydrogen target, we also utilize the Čerenkov radiation pulse height from the liquid hydrogen cell to measure the interaction vertex positions in reactions having entirely neutral particle final states.

Depending on the beam channel assignment for this part of our proposal, whether it is the 2.5 mrad beam line branch prior to the spectrometer facility at the Meson Laboratory or the beam line at the Proton Laboratory East Enclosure, we plan to run at four different beam energies: at 40 GeV, 80 GeV, 160 GeV and 320 GeV or at the highest possible beam energy compatible with beam intensity requirements at the time of the run. A negatively charged beam having an intensity of 10^6 to 10^7 particles/

pulse and a momentum resolution of $\Delta p/p < \pm 0.5\%$ is desired for a total period of 600 hours, inclusive of data acquisition and equipment testing times. The beam components, π^-, K^-, $\bar{p}$, with relative intensities[2] of about 100:2:1.5 respectively, will be identified by a pair of gas threshold Čerenkov counters and a differential Čerenkov counter set to monitor antiprotons. In the case of the 2.5 mrad beam line usage, we plan to use those Čerenkov counters which are already a part of this beam transport system at NAL. In the case of the Proton Laboratory's beam line usage, we would propose to use only a pair of gas threshold Čerenkov counters which can be in the form of beam pipes instrumented for this purpose by NAL.

Our ability to handle multi-gamma-ray final states other than the π^- charge-exchange reaction, makes this investigation capable of answering several outstanding questions which are otherwise poorly understood or not yet examined. In contrast to earlier experiments, in our case both geometrical acceptance and mass acceptance are such that a good spin-parity analysis can be made. The decay angular distributions in the produced bosons' rest-frame will have a resolution of $\Delta(\cos \theta) \approx 1/100$. Moreover, in the majority of cases, good events will be triggered because the energy resolution of our spectrometer system will make it possible to have a narrow band total energy trigger that corresponds to the energy released in a multi-gamma-ray final state with momentum transfers of $t < 1.5$ $(\mathrm{GeV}/c)^2$. The total energy trigger in this case is defined when events of reaction (1) satisfy the set upper and lower discrimination levels of the TASC pulse height measurement.

The proposed experimental study of multi-gamma-ray final states with our spectrometer system is similar to the CERN boson spectrometer's studies with charged particle multi-pion final states, except that in our case background events are further suppressed because of a rigorous total energy selection criterion. The CERN studies proved to be useful in the identification of boson states that decay into charged pions or kaons. Similarly, we expect to find structure among the multi-gamma-ray final states where the mass resolution requirement is high, in view of the narrow widths in most of these electromagnetic decays of bosons.

A. EXPERIMENTAL PROGRAM

The following categories of events will be studied by the proposed experimental arrangement. The details of our experimental arrangement are presented in Section B. The design principles of the proposed multi-gamma-ray spectrometer system and the modular configuration are discussed in Appendix I.

Single gamma-ray studies:

Together with the measurement of differential cross sections of identifiable multi-gamma states, the cross section for single γ-ray production will also be measured. This is just the inverse of the pion photoproduction reaction:

$$\pi^- p \leftrightarrow \gamma n \qquad (2)$$

The cross section of this reaction can be estimated by using the

Vector Dominance model and the known cross section of the reaction[3] $\pi^- p \rightarrow \rho^o n$:

$$\sigma(\pi^- p \rightarrow \gamma n) \cong \frac{\alpha}{4} \left(\frac{\gamma_\rho^2}{4\pi}\right)^{-1} \cdot \sigma(\pi^- p \rightarrow \rho^o n) \qquad (3)$$

Thus, $\sigma(\pi^- p \rightarrow \gamma n) = (1/274) \cdot 100 \cdot (10/p_\pi)^2 \mu b$ or at 100 GeV, a total reaction cross section of 4 nb.

Two gamma-ray studies:

The two gamma-ray system is characterized by the allowable quantum number of $I^G = (0^+, 1^-)$ for isospin and G-parity, and $J^P = (0^-, 0^+, 2^-, 2^+ \ldots)$ for spin and parity; $J \neq 1$. The charge conjugation quantum number is fixed to $C = +1$. The reactions of interest are of the following type:

$$\pi^- p \rightarrow \eta^o(549)n; \; \eta^o \rightarrow \gamma\gamma, \; 37.5\% \qquad (4)$$

The cross sectional behavior of this reaction is given[4] by $\sigma(\pi^- p \rightarrow \eta^o n; \; \eta^o \rightarrow \gamma\gamma) = 286/(p_\pi)^{1.46} \mu b$, or at 100 GeV, a total reaction cross section of 350 nb. The reaction:

$$\pi^- p \rightarrow X^o(958)n; \; X^o \rightarrow \gamma\gamma, \; 2\% \qquad (5)$$

is particularly interesting because the spin-parity of this particle, after several years of experimentation, has not been determined conclusively. The SU(3) classification of pseudoscalar bosons remains dependent on whether $X^o(958)$ or E(1422) is the missing singlet member of this group. The cross sectional level of this reaction is given[5] approximately by:

$$\sigma(\pi^- p \rightarrow X^o(958)n;\ X^o \rightarrow \gamma\gamma) \sim 700\cdot(3.65/p_\pi)^2 \text{ nb} , \text{ or}$$

at 100 GeV, a total reaction cross section of ~ 1 nb.

Our experimental arrangement would also be sensitive to the detection of a 2γ decay mode of the A_2 and f^o mesons. In these cases, the 2γ decay mode so far has not been observed.

Three gamma-ray studies:

The three gamma-ray system is restricted to the quantum numbers of $J \neq 0$ and $C = -1$. As such, this system is best suited for the search of new vector mesons heavier than the ρ^o, ω^o, ϕ^o. Otherwise, the allowable states are those with the quantum numbers of $I^G = (0^-, 1^+)$, $J^P = (1^-, 1^+, 2^-, 2^+ \ldots)$ and $C = -1$. A specific reaction of interest to dynamical phenomena is:

$$\pi^- p \rightarrow \omega^o n;\quad \omega^o \rightarrow \pi^o\gamma,\ 9.4\% \qquad (6)$$

The cross sectional level of this reaction is given[6] by $\sigma(\pi^- p \rightarrow \omega^o n,\ \omega^o \rightarrow \pi^o\gamma) \sim 5\mu b\cdot(10/p_\pi)^2$, or at 100 GeV, a total reaction cross section of 50 nb. In this category, in addition to the $\pi^o\gamma$ system, boson decay modes of $\eta^o\gamma$ and $X^o\gamma$ can be examined. These are of great interest to the SU(3) theory of electromagnetic interactions.[7]

Four gamma-ray studies:

The four gamma-ray system can be examined in the form of $\pi^o\pi^o$, $\eta^o\eta^o$, and $\eta^o\pi^o$ categories. The allowable quantum numbers are $I^G = 0^+$ for $\pi^o\pi^o$ and $\eta^o\eta^o$ and $I^G = 1^-$ for $\eta^o\pi^o$; $C = +1$ in all cases. Moreover, Bose statistics restricts the $\pi^o\pi^o$ system to J = even and parity = +1. A rich structure in the $\pi^o\pi^o$ system can be expected which can be very informative for the clarification of unestablished states such as ABC(320), $\sigma(410)$, $\epsilon(700)$. A typical reaction in this final state is:

$$\pi^- p \rightarrow f^o n; \qquad f^o \rightarrow \pi^o\pi^o \tag{7}$$

which has a cross section[8] of 20 $\mu b\cdot(10/p_\pi)^2$, or at 100 GeV, a total reaction cross section of 200 nb. A very interesting structure reported[9] at a mass of 1060 MeV, if it is established to have a $J^P = 2^+$, could be the lowest lying particle on the Pomeranchuk Regge trajectory which is exchanged in diffractive scattering processes. The cross sectional level in this case is: $\sigma(\pi^- p \rightarrow P(1060)\, n;\ P \rightarrow \pi^o\pi^o) \simeq 40\ \mu b/4\cdot(4/p_\pi)^2$, or at 100 GeV, 16 nb. The $\eta^o\pi^o$ system should be very useful for the study of effects in the A_2 (1300) region. The cross sectional level for the reaction:

$$\pi^- p \rightarrow A_2^o n; \quad A_2^o \rightarrow \eta^o\pi^o,\ (\eta^o \rightarrow \gamma\gamma), \sim 3\% \tag{8}$$

is found[10] to be $\approx 4\ \mu b\cdot(10/p_\pi)^{1.4}$, or at 100 GeV, a total reaction cross section of 100 nb. Other $I^G = 1^-$ states, such as the $\delta(966)$, may also have substantial $\eta^o\pi^o$ decay modes.

Non-resonant multi-gamma ray studies:

Using the one-pion-exchange dynamical mechanism features we expect to measure the unique cross-section of $\pi^-\pi^+ \rightarrow \gamma\gamma$ at high center-of-mass energies, possibly prior to the realizations of high energy e^+e^- colliding beam facilities. This information can be extracted from the reaction:

$$\pi^- p \rightarrow \gamma\gamma n \qquad (9)$$

where the exchanged π^+ is almost on its mass-shell at small momentum transfer values. Well known theoretical methods[11] allow the expression of cross sections in the form of:

$$\frac{d\sigma}{dm_{\gamma\gamma}}(\pi^- p \rightarrow \gamma\gamma n) = \frac{G^2}{4\pi} \cdot \frac{F(m_{\gamma\gamma}, t)}{p_\pi^2} \cdot \sigma(\pi^-\pi^+ \rightarrow \gamma\gamma)$$

Assuming a broad resonant-type form[12] for the cross section of the reaction:

$$\pi^-\pi^+ \rightarrow \gamma\gamma \qquad (10)$$

$$\sigma(\pi^-\pi^+ \rightarrow \gamma\gamma) = \frac{2\pi\alpha^2}{S_{\gamma\gamma}}\left[1 - \frac{4m_\pi^2}{S_{\gamma\gamma}}\right]^{1/2} \cdot \frac{m^4}{(S_{\gamma\gamma} - m^2)^2 + m^2\Gamma^2},$$

$$\Gamma = 100 \text{ MeV}, \quad m = 1000 \text{ MeV}, \quad S_{\gamma\gamma} = m_{\gamma\gamma}^2$$

we find a cross section for reaction (9) at the level of 13.5 nb$\cdot(40/p_{\pi})^2$. Similarly, studies on non-resonant 3-γ and 4-γ reactions will be made to find the $\pi\rho$ or $\pi\pi$ couplings to these channels. The cross-sectional level in these cases should be the same as in the 2-γ case.

The experimental results on the electromagnetic decays of bosons, or their strong decays in the form of $\pi^o\pi^o$, are summarized in Figs. 1 and 2. These are results obtained mainly from heavy-liquid bubble chambers and also with conventional shower counters. Both of these methods yield results with very limited statistics and poor mass resolution. We expect to improve the results in both areas. Assuming an average of 5×10^6 π/pulse, 600 pulses/hr, and a 1 meter long liquid hydrogen target or its equivalent, our event collection rate becomes: 12.7 events/hr/nb; or 7000 events/nb in 550 hours of actual data acquisition beam time. Details on our spectrometer system's mass resolution are discussed in Section B.

Inclusive reaction studies:

The important studies of inclusive or semi-inclusive reactions with leading single γ, π^o, η^o, and K_s^o will also be made under separate triggering conditions, to measure the double differential cross sections $d^2\sigma(\theta_x, E_x, E_o)/dE_x\, d\Omega_x$ in the following reactions:

$$\pi^- p \rightarrow \gamma \text{ (MM)} \qquad (11)$$

$$\pi^- p \rightarrow \pi^o\text{(MM)};\ \pi^o \rightarrow \gamma\gamma,\ 100\% \qquad (12)$$

$$\pi^- p \rightarrow \eta^o\text{(MM)};\ \eta^o \rightarrow \gamma\gamma,\ 37.5\% \qquad (13)$$

$$\pi^- p \rightarrow K_s^o\text{(MM)};\ K_s^o \rightarrow \pi^o\pi^o,\ 31.3\% \qquad (14)$$

$$K^- p \rightarrow K_s^o\text{(MM)} \qquad (15)$$

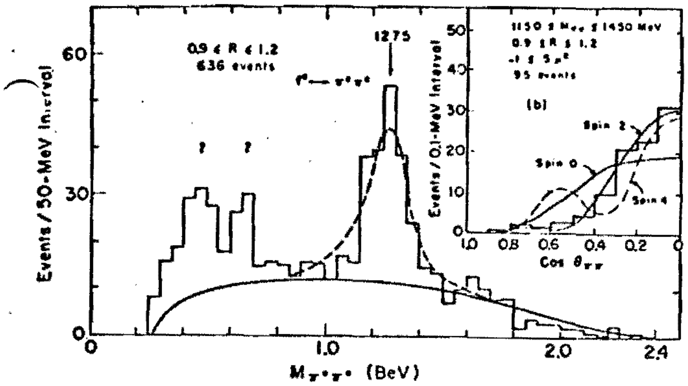

Fig. a Data of Wahlig et al.: $\pi^+ p \rightarrow \pi^0\pi^0 n$ at 10 BeV/c, obtained in a spark chamber experiment. The insert shows evidence for spin 2^+ for the f^0 meson.

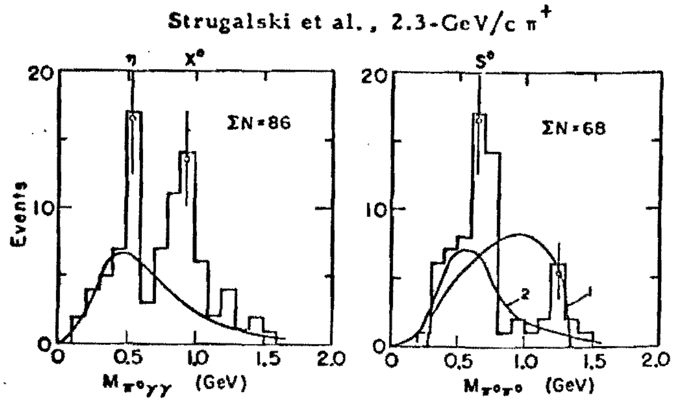

MUB 13196

Fig. b Data of Strugalski et al., obtained in work with a xenon bubble chamber. Mass distributions for $\pi^0\gamma\gamma$ events and $\pi^0\pi^0$ events.

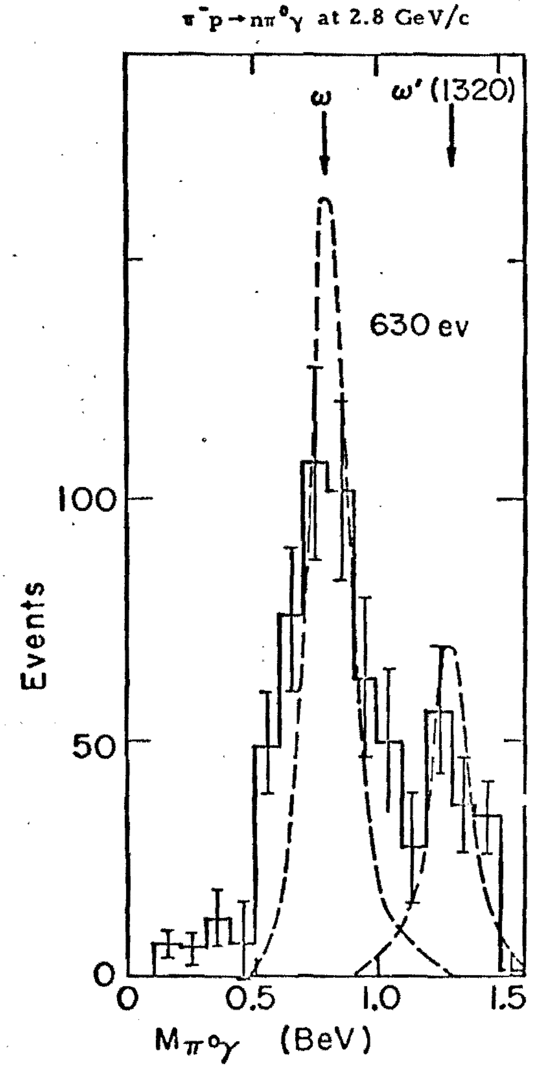

MUB 13191

Fig. C Data of Barmin et al. in a propane-xenon bubble chamber: the $\pi^0\gamma$ mass distribution.

FIGURE 1

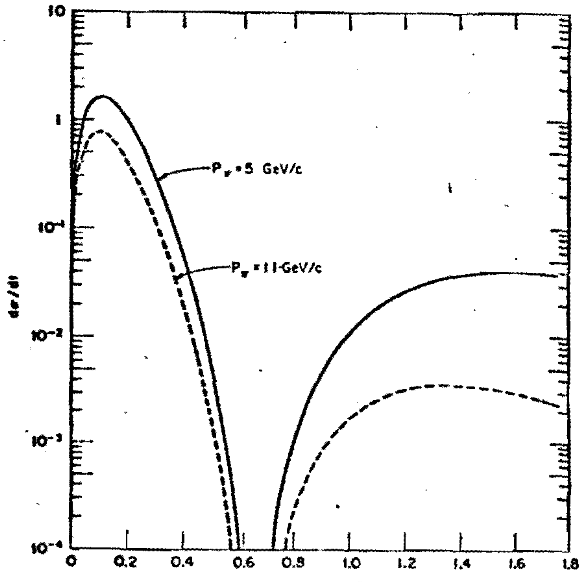

Fig. d Differential cross sections for $\pi + N \rightarrow \omega + N$

L.L. Wang, Phys. Rev. Lett. 16, 756 (1966

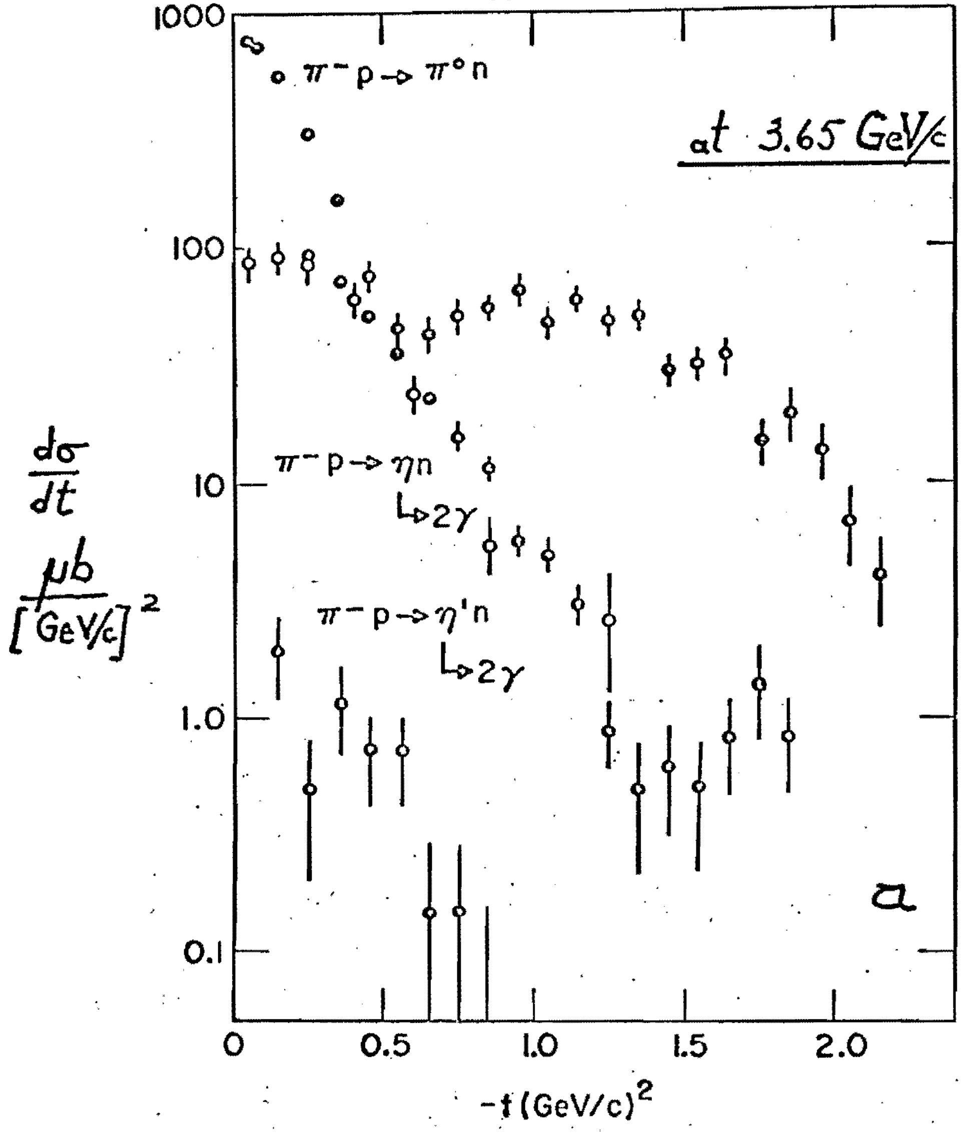

Volume 33B, number 7 PHYSICS LETTERS 7 December 1970

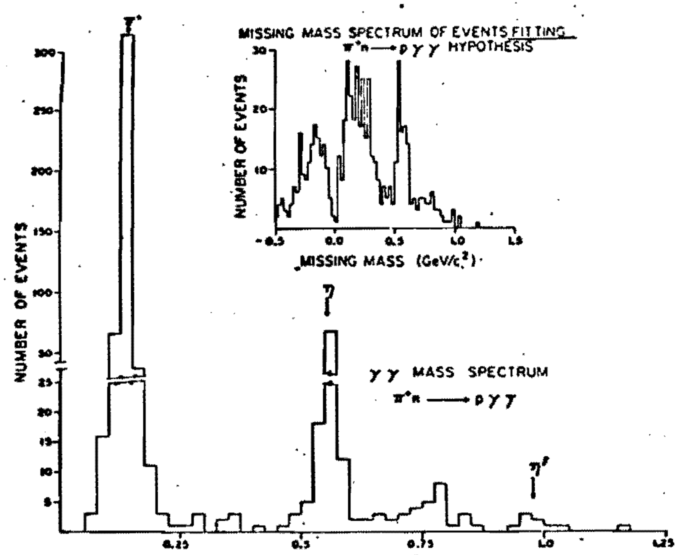

b. Mass plot of the 2γ system for events constrained by energy and momentum conservation to fit the hypothesis $\pi^+ d \to p(p)\gamma\gamma$. Note the absence of background at the η'(960) mass. Insert shows the same spectrum calculated as a missing mass without use of γ measurements.

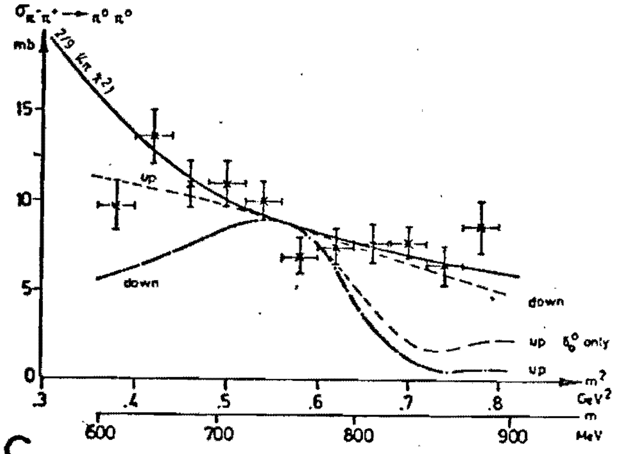

c. Values of the $\pi^-\pi^+ \to \pi^0\pi^0$ cross section extrapolated as a function of the (mass)^2 of the dipion (linear extrapolation of the function $-F(\omega, \Delta^2)(\mu^2/\Delta^2)$.
full line: unitarity limit for s-wave $\pi^-\pi^+ \to \pi^0\pi^0$ scattering in $I = 0$ state
dashed and dashed-dotted: cross section calculated from the various solutions for δ_0^0 and δ_0^2 of Malamud

FIGURE 2

$$K^- p \rightarrow \pi^0 \text{ (MM)} \qquad (16)$$

$$\bar{p} p \rightarrow \pi^0 \text{ (MM)} \qquad (17)$$

The cross sectional estimates at 100 GeV for the reactions (12), (14), (15) and (16) are at the level of 10-30 μb in each case. These measurements would complement similar studies proposed at NAL by others, where instead of neutrals as in our case, leading charged particles are detected in the above reactions. Data on leading charged particles and leading neutral particles, as we are proposing to acquire, together would aid in the process of choosing among possible theoretical models[13] of inclusive reactions. In particular, the need to study the energy dependence of these reactions is also stressed[14].

Among the above inclusive reactions only reaction (15) is measured[15] at CERN in a recent hydrogen bubble chamber compilation at 10 GeV. The results of this study are shown on Fig. 3. On reactions (12) and (13), a recent proposal from HEPL[16] is approved and scheduled to run at SLAC during the first quarter of 1972, using a pair of large NaI(Tl) TASCs at 10 and 16 GeV pion energies. The experience gained during the forthcoming SLAC run could benefit greatly the improvement and testing of the spectrometer system proposed for NAL.

Studies with targets of Complex Nuclei

Besides hydrogen we propose to use targets of complex nuclei (Cu and Pb) and measure the momentum transfer dependence of the following reactions:

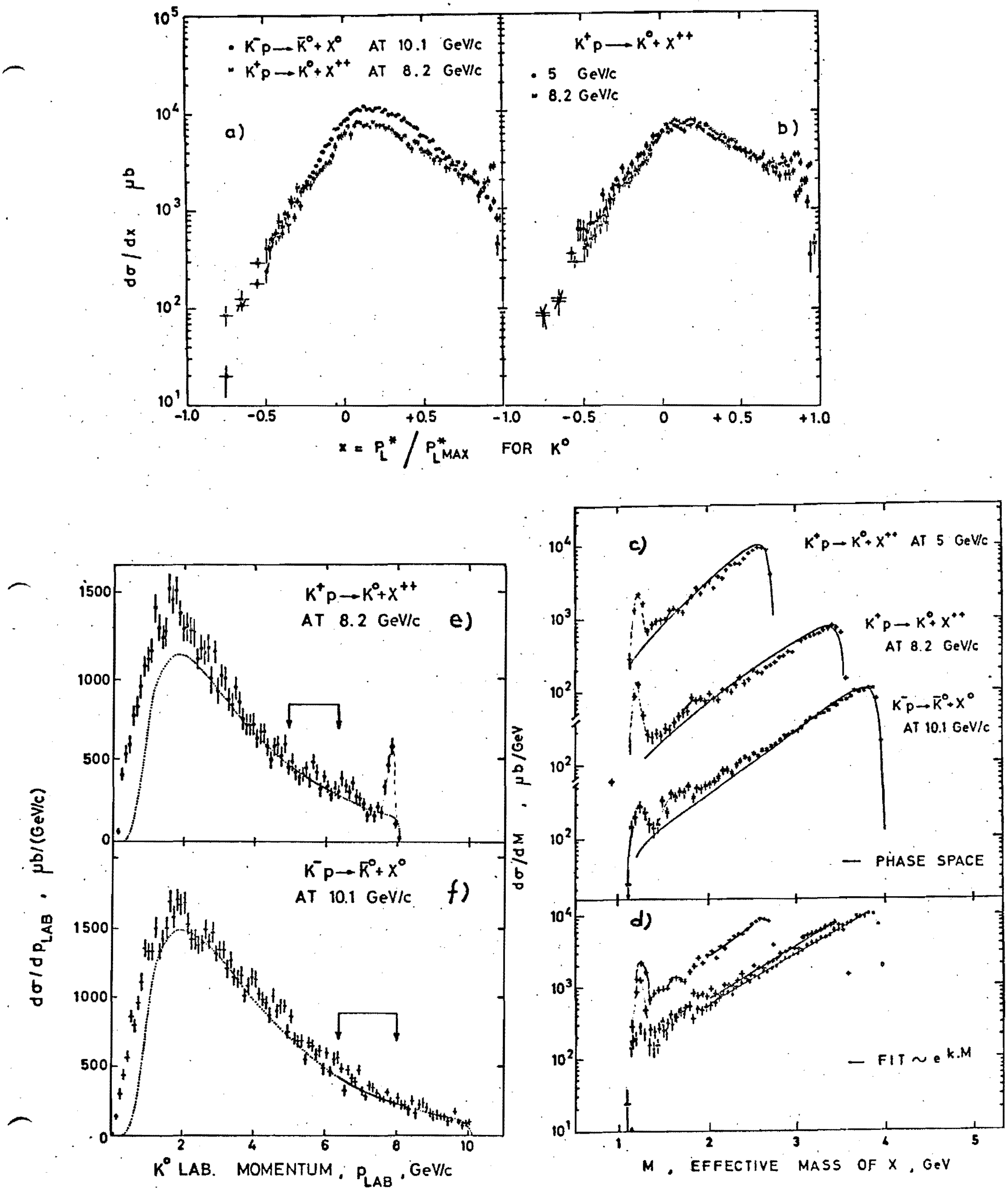
K⁻p → K̄° + X° AT 10.1 GeV/c
K⁺p → K° + X⁺⁺ AT 8.2 GeV/c
a)
K⁺p → K° + X⁺⁺
5 GeV/c
8.2 GeV/c
b)
10⁵
10⁴
10³
10²
10¹
dσ / dx μb
-1.0
-0.5
0
+0.5
-1.0
-0.5
0
+ 0.5
+1.0
x = P*_L / P*_LMAX FOR K°
c)
K⁺p → K° + X⁺⁺ AT 5 GeV/c
K⁺p → K° + X⁺⁺ AT 8.2 GeV/c
K⁻p → K̄° + X° AT 10.1 GeV/c
PHASE SPACE
d)
FIT ~ e^{k.M}
dσ/dM , μb/GeV
M , EFFECTIVE MASS OF X , GeV
1
2
3
4
5
10⁴
10³
10²
10¹
K⁺p → K° + X⁺⁺
AT 8.2 GeV/c
e)
K⁻p → K̄° + X°
AT 10.1 GeV/c
f)
1500
1000
500
0
dσ / d p_LAB , μb/(GeV/c)
2
4
6
8
10
K° LAB. MOMENTUM , p_LAB , GeV/c

FIGURE 3

$$\pi^- A \rightarrow \pi^o A^* \quad ; \quad \pi^o \rightarrow \gamma\gamma, 100\% \qquad (18)$$

$$\pi^- A \rightarrow \eta^o A^* \quad ; \quad \eta^o \rightarrow \gamma\gamma, 37.5\% \qquad (19)$$

$$\pi^- A \rightarrow X^o A^* \quad ; \quad X^o \rightarrow \gamma\gamma, 2\% \qquad (20)$$

$$K^- A \rightarrow K_s{}^o A^* \quad ; \quad K_s{}^o \rightarrow \pi^o \pi^o, \ 31.3\% \qquad (21)$$

at the indicated beam energies. In our case, the A^* is guaranteed to be only an excited nucleus state by the veto-house triggering condition. The reactions (18) - (21) on complex nuclei so far have not been measured. The cases A = 1 (liquid hydrogen target) of these reactions have been studied between 3 - 18 GeV/c and there are NAL proposals[17] to carry out these measurements at NAL energies. In our case, although the A = 1 measurements nominally would be redundant, they serve the important function of establishing the relationship:

$$\frac{d\sigma}{dt}(\pi^- + {}_Z A_N \rightarrow X^o + {}_{Z-1}A^*_{N+1}) = \frac{d\sigma}{dt}(\pi^- p \rightarrow X^o n)G(t)Z_{eff} \qquad (22)$$

where we should have the A = 1 data acquired under the same experimental conditions and make the above comparisons independent of experimental normalizations. The primary goal of this investigation is the measurement of Z_{eff}, the effective number of protons participating in the interaction of pions with complex nuclei, and in particular, the detection of changes in the values of Z_{eff} as a function of beam incident energies.

The above comparison between hydrogen and complex nuclear data is simplified at a regime where $G(t) \rightarrow 1$. In Equation (22), G(t) is defined to be the quantity: one minus the squared nuclear form factor. The behavior of $G(t)$ can be estimated in the weak scattering limit of the Fermi gas model, where $G(t)$ is expected to become unity near $t \sim (2K_F)^2$; $K_F \simeq 0.250$ GeV/c is the average nuclear Fermi momentum. Thus, at the momentum transfer values of $t \sim [0.25 - 0.40](\text{GeV}/c)^2$ the nuclear coherent process diminishes and the nuclear incoherent process dominates, allowing for π^o, η^o, X^o absorption by individual nucleons. Using this fact, a direct measurement of neutral-boson-nucleon total cross sections will be obtained: $\sigma_{tot}(\pi^oN)$, $\sigma_{tot}(\eta^oN)$, $\sigma_{tot}(X^oN)$. Our method of measuring these total interaction cross sections is similar to that of $\sigma_{tot}(\rho^oN)$, obtained from coherent ρ^o photoproduction measurements on complex nuclei. These charge-exchange type incoherent reactions, at moderate t values, measure the transmission of produced neutral bosons through nuclear matter in a regime where nuclear effects contribute the least and therefore the sensitivity on the parameters $\sigma_{tot}(X^oN)$ is enhanced. This observation is stressed in several theoretical[18] recent treatments. Fig. 4 reveals the sensitivity of this method. Z_{eff}/Z is displayed as a function of nuclear mass A, for several values of $\sigma_{tot}(\pi^oN)$. For example, at $A = 208$, a 20% change in Z_{eff}/Z yields a 25% change in the expected value of $\sigma_{tot}(\pi^oN)$. Since the primary measurement determines Z_{eff}, this cross section enters as a parameter in a two dimensional integral expression of Z_{eff}.

In the cross sectional measurement of reactions (18 - 21), we are very much interested to search for an energy dependence of Z_{eff} in relation (22). The energy dependent observation of such an important effect would be due to nuclear transmission of neutral or charged bosons which are mediated by particle fluctuations with coupled inelastic channels.

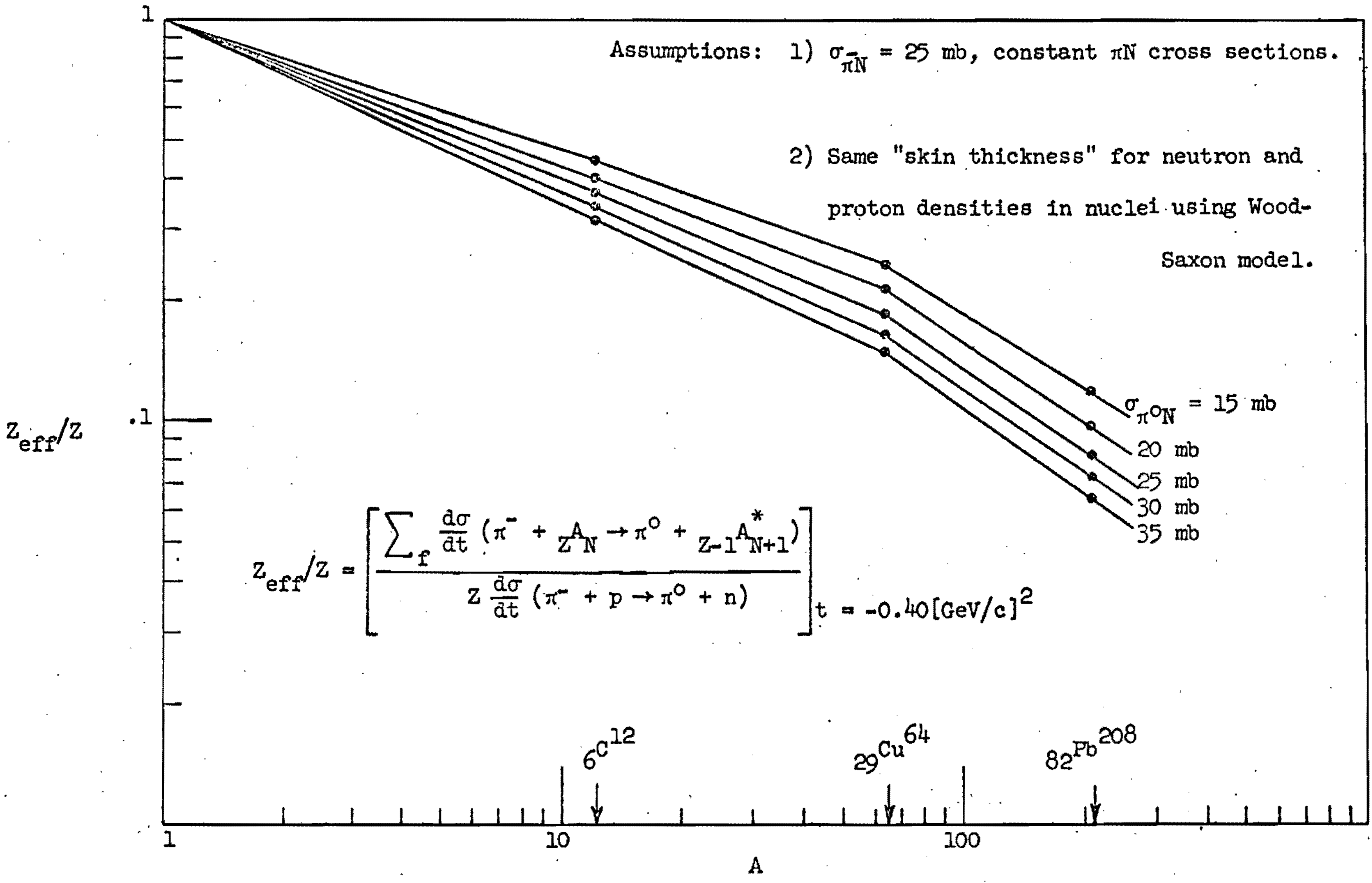
1
.1
Z_{eff}/Z
Assumptions: 1) $\sigma_{\pi^- N}$ = 25 mb, constant πN cross sections.
2) Same "skin thickness" for neutron and proton densities in nuclei using Wood-Saxon model.
$\sigma_{\pi^0 N}$ = 15 mb
20 mb
25 mb
30 mb
35 mb
$$Z_{eff}/Z = \left[\frac{\sum_f \frac{d\sigma}{dt}(\pi^- + {}_ZA_N \rightarrow \pi^0 + {}_{Z-1}A^*_{N+1})}{Z\,\frac{d\sigma}{dt}(\pi^- + p \rightarrow \pi^0 + n)}\right]_{t = -0.40[\mathrm{GeV}/c]^2}$$
${}_6C^{12}$
${}_{29}Cu^{64}$
${}_{82}Pb^{208}$
1
10
100
A

FIGURE 4

In this picture, the phenomenon is explained by saying that particle propagation, at ultra-relativistic energies, occurs through fluctuations between the fundamental particle state and the states of connected inelastic channels having the same quantum numbers as the propagating particle. For example, in the case of π^- charge exchange on complex nuclei, the interaction of pions with nuclear matter would be mediated by the $A_1(1080)$ state, very much like the interaction of photons seems to proceed via the ρ^o state.

We find that the A_1 - dominance process of interacting pions can best be detected in the energy dependence of charge-exchange type cross sections, rather than in the energy dependence of $\sigma_{tot}(\pi^- A)$ measurements on complex nuclei. Figure 5 reveals the sensitivity of inelastic channel nuclear shadowing effects in charge exchange cross sections of pions on complex nuclei. This calculation is based on the uniform density nuclear model and the two-step process of $\pi^- \rightarrow A_1 \rightarrow \pi^o$, via the $\pi\pi\pi$ measured coherent mass spectrum,shown on Fig. 5(a). The calculation in Fig. 5(b) is presented as a ratio: with the A_1-dominant process causing nuclear shadowing over that which is without the A_1 effect. Based on this calculation[19] we can expect a 10-14% reduction of cross sections of the type (18) - (21) at high energies. In comparison with charge-exchange processes, a similar effect in the measurement of $\sigma_{tot}(\pi^- A)$ is estimated to cause a cross sectional reduction of only 3.5% which shows the sensitivity of our proposed method.

B. EXPERIMENTAL METHOD

Our experimental method relies upon current and new experimental instrumentation techniques. The detection system in our proposed work is optimized to make maximum use of the available beam intensities of NAL at the highest possible detection efficiency for the study of multi-gamma-ray final states.

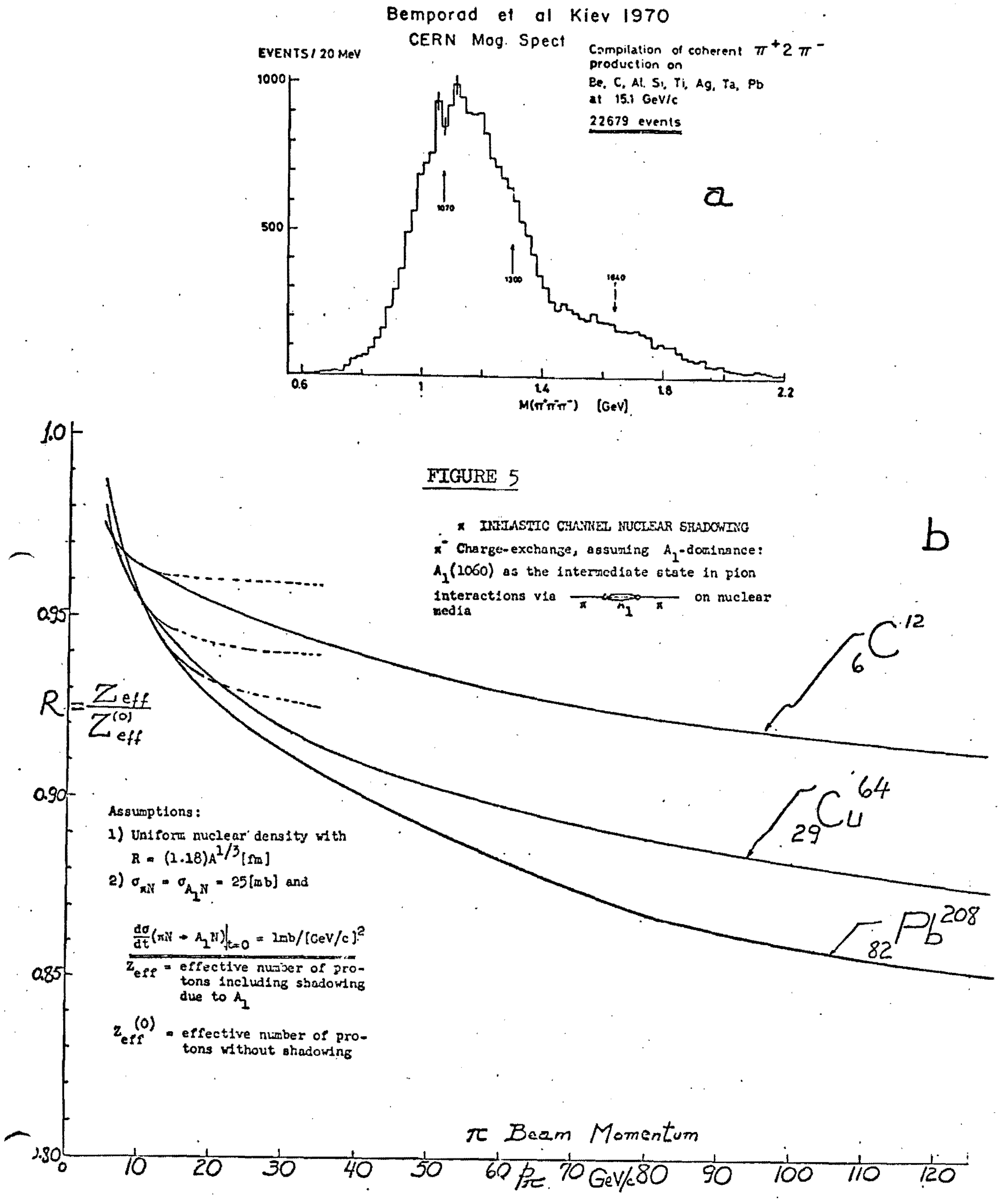

FIGURE 5

* INELASTIC CHANNEL NUCLEAR SHADOWING

*⁻ Charge-exchange, assuming A_1-dominance: $A_1(1060)$ as the intermediate state in pion interactions via π — A_1 — π on nuclear media

Assumptions:

1) Uniform nuclear density with $R = (1.18)A^{1/3}$ [fm]

2) $\sigma_{\pi N} = \sigma_{A_1 N} = 25$ [mb] and

$$\frac{d\sigma}{dt}(\pi N \to A_1 N)\Big|_{t=0} = 1\text{mb}/[\text{GeV}/c]^2$$

Z_{eff} = effective number of protons including shadowing due to A_1

$Z_{eff}^{(0)}$ = effective number of protons without shadowing

Large NaI(Tl) TASC crystals developed, tested and available at HEPL, measure the total energy of gamma-rays to an accuracy better than 1% (FWHM) at the NAL energies of interest. Fig. 6 shows the energy resolution of such a crystal assembly, 16" diameter 24" thick, tested with electron beams at SLAC and the HEPL Mark III accelerators. With regard to spatial resolution, a recent effort[20] has yielded the direct and clear observation of electromagnetic showers in a 4" x 4" x 10" NaI(Tl) crystal, viewed by a three-stage image intensifier. The showers were generated by 0.5 - 15 GeV electrons and a few thousand photographs were obtained. We conclude from the study of these photographs that in the case of 15 GeV electrons or photons, at the shower's maximum electron multiplicity depth, ~ 95% of the electrons are found inside a shower width of ~ 0.7". We have also clearly observed the shower width's narrowing effect with increasing incident energies.

Mass resolution

Our mass resolution for bosons decaying into multi-gamma-ray final states is greatly improved by the total energy measurement resolution. For example, we consider the two-gamma-ray decay of a neutral boson with mass M, gamma-ray energies E_1 and E_2 and an opening angle θ between the gamma-rays.

$$M = 2\sqrt{E_1 E_2}\,\sin(\theta/2) \tag{23}$$

In a detector system such as ours where the total energy $E_0 = E_1 + E_2$ is measured with an accuracy far superior than in the individual energy measurements, the boson mass can be evaluated by the equivalent formula:

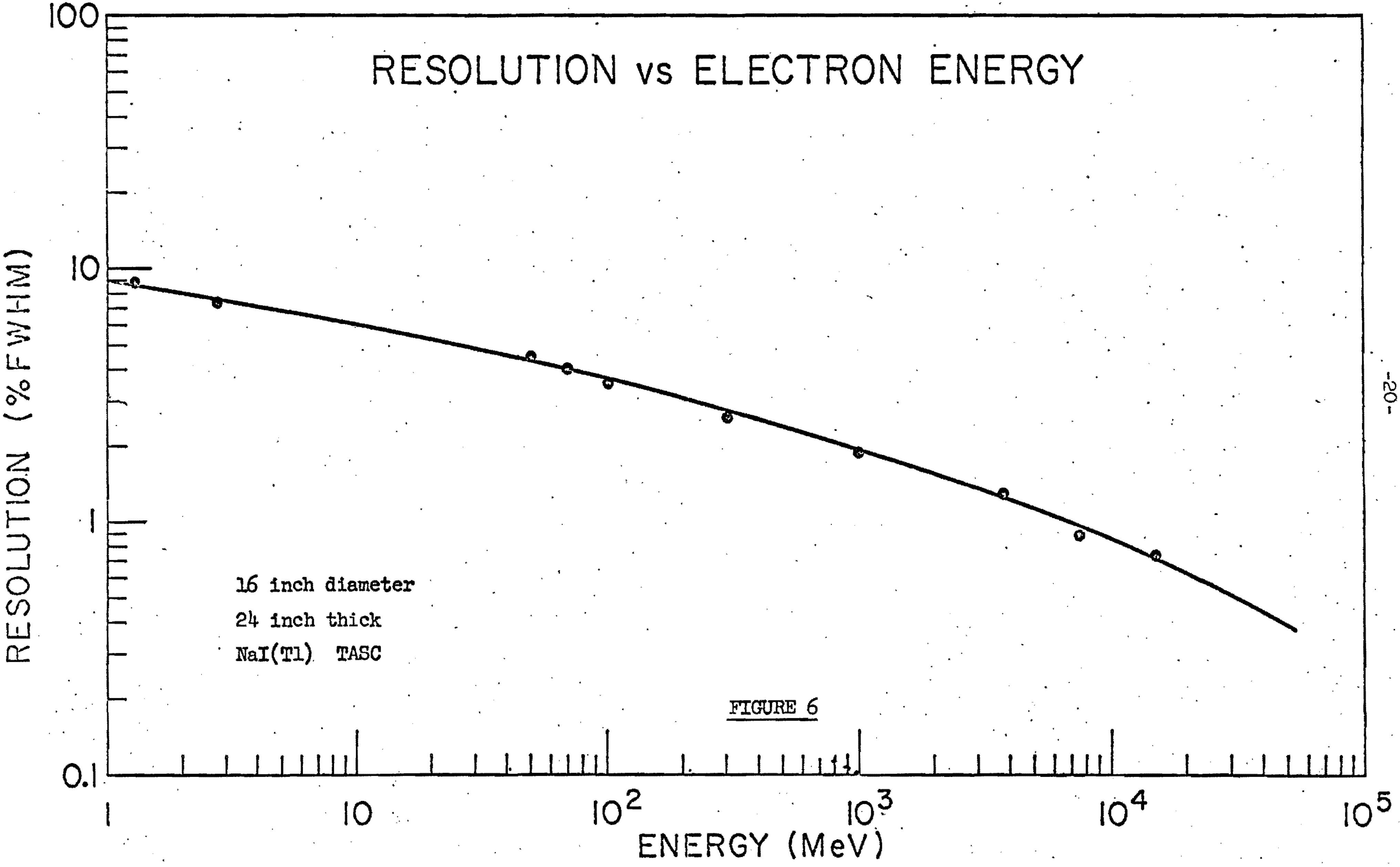
RESOLUTION vs ELECTRON ENERGY
RESOLUTION (% FWHM)
100
10
1
0.1
ENERGY (MeV)
1
10
10^2
10^3
10^4
10^5
16 inch diameter
24 inch thick
NaI(Tl) TASC

FIGURE 6

$$M = \frac{2E_o \sin(\theta/2)}{\sqrt{\frac{E_1}{E_2}} + \sqrt{\frac{E_2}{E_1}}} \qquad (24)$$

The following graph[21] shows the difference between terms entering in Equation (23) and (24) which are dependent on the measurements of E_1 and E_2.

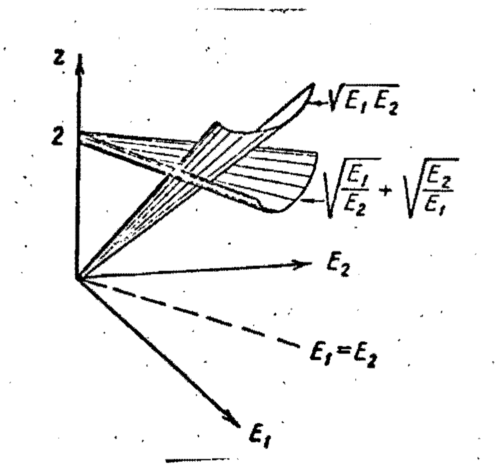

Therefore, to first order our mass measurement is almost independent of the E_1 and E_2 values, if E_o is very well known so that equation (24) can be used. In this case the mass resolution is determined mainly by the quadratic sum of the total energy resolution and the opening angle resolution.

We have developed similar relations for the cases of three-gamma and four-gamma final states. We conclude that the mass resolution of neutral bosons using our spectrometer system is $\frac{\Delta M}{M} < 2\%$ for ~ 90% of the events.

Liquid hydrogen target/Čerenkov counter

We propose to use a 1 meter long liquid hydrogen target to take maximum advantage of beam intensities at NAL.

This target assembly is designed to have the capability of detecting Čerenkov light from the hydrogen medium. (This has already been done in practice, cf. reference 22). In the special cases of interest to us where beam interactions yield entirely neutral final states, i.e., a neutron and several gamma-rays, the Čerenkov light pulse-height is a direct measure of the interaction's vertex position inside the liquid hydrogen target. Multiple reflections of the 24.2° Čerenkov radiation in hydrogen can be minimized by slightly tapering the liquid hydrogen cylindrical vessel. Since the beam's attenuation due to interactions inside the target is small, we would expect to find a uniform distribution of pulse-heights when these are selected according to our overall triggering conditions. Deviations from such a uniform distribution would be caused primarily by Čerenkov light attenuation from multiple reflections over the internal surface of the aluminized target vessel. In this manner, for the particular events of interest, we have a self-calibrating method of establishing linearity between Čerenkov light pulse-height and interaction vertex position.

This target will be prepared at HEPL. We plan to provide such a target cell with the radiation shield and associated Čerenkov counter instrumentation at NAL, after making a prototype LH_2 target/Čerenkov counter at HEPL and testing it with pion beams at SLAC. The LH_2 target cell and radiation shield will be constructed according to the flange design specifications of NAL. We plan to use one of the closed cycle helium refrigeration equipment systems at NAL,to liquify hydrogen gas and monitor the target's performance. Also, according to NAL specifications, sealed nitrogen gas bags will surround the photomultiplier bases which view counters placed at this target or at its vicinity.

Using this method, we expect to measure the vertex positions of our interactions to within 3 cm., (FWHM), over the 1 meter length of the hydrogen target. This method would make a great contribution in the space resolution of our detector system. It would enhance further the resolution in both multi-gamma-ray effective mass and momentum transfer determinations. With this precise type of information, our momentum transfer resolution δt would be about 5 - 7 times better than in any other similar experiment.

While this method was devised by us independently, recently we became aware that in a CERN experiment by the Karlsruhe-Pisa group,[22] a target with the above specifications was designed, successfully tested and used in an experiment. Figure 7 shows the results of this effort, indicating that interaction vertex positions can be determined with typical resolution of $\delta \ell = 3$ cm (FWHM) for the event types of interest to our proposal. Figure 8 displays the preliminary design details of our target with a summarized functional description on the attached caption.

Beam clearing magnet

A 100 kgauss-meters clearing magnet is required for the purposes of sweeping the primary beam away from the spectrometer system and clearing all charged particles produced at the target, to prevent their entrance to our multi-gamma-ray spectrometer. Both requirements are essential to having a spectrometer operation free of electronic pile-up problems and free of total energy measurement distortions. (We remark that forward neutrons from the target dynamically are constrained to have small kinetic energies so that they would not cause such a distortion.)

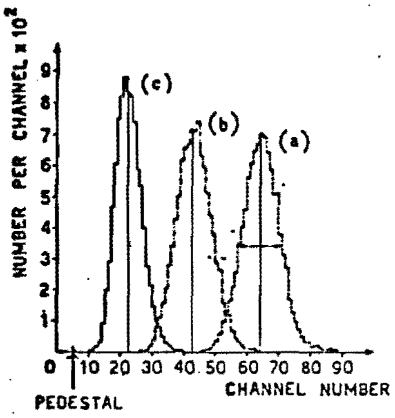

Typical pulse height spectra at different diaphragm positions: $Z = 17.5$ cm (a); 7.5 cm (b); 1.5 cm (c).

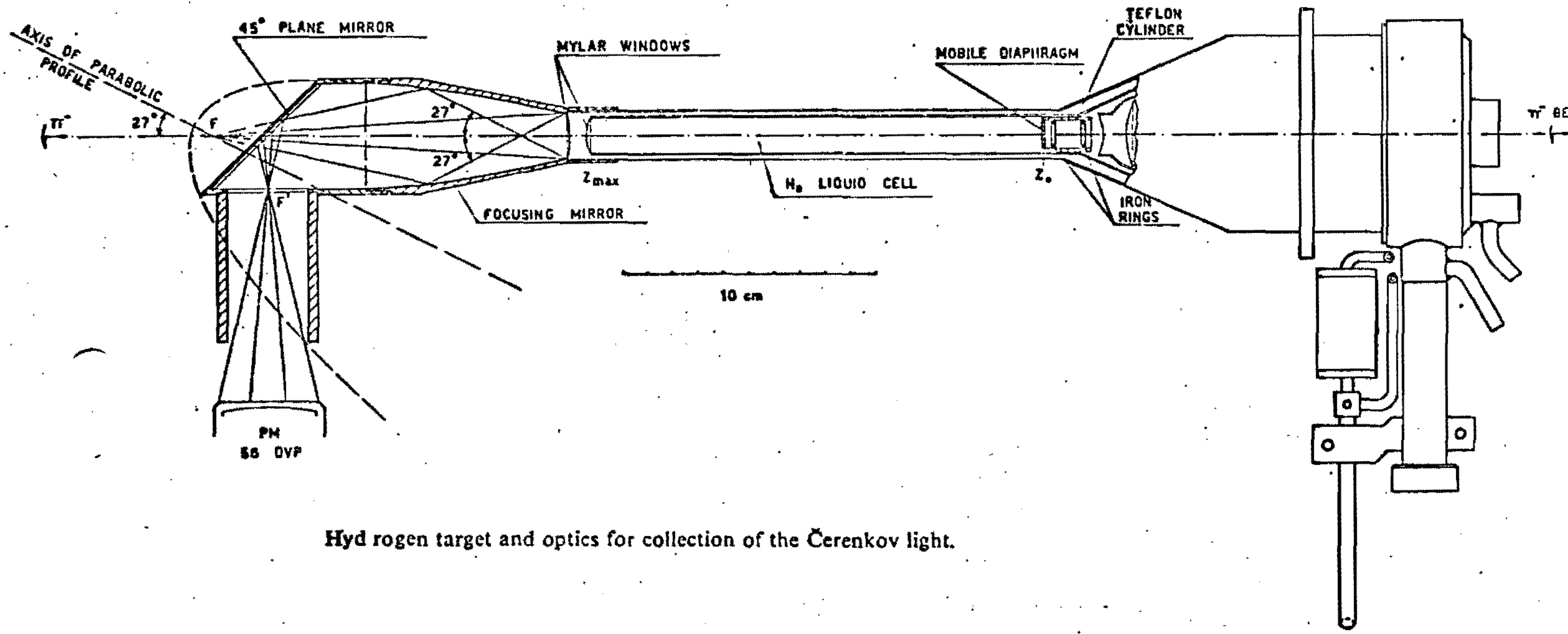

Hydrogen target and optics for collection of the Čerenkov light.

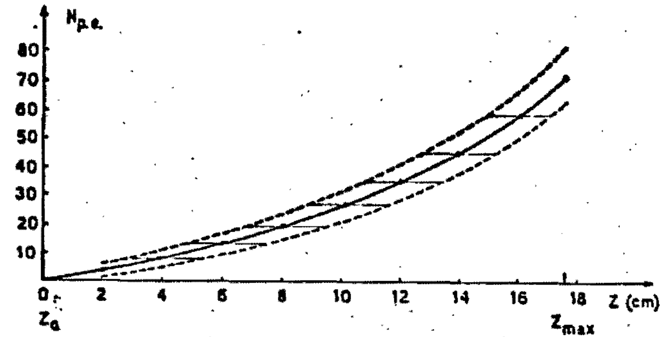

FIGURE 7

Calibration curve for neutral interactions. The vertical distance between the curve and the dashed lines represents the standard deviation in pulse height at a given Z; the horizontal segments give a measure of the corresponding degree of accuracy in the localization of neutral interactions; Z_0 and Z_{max} are respectively the beginning and the end of the target; $N_{p.e.}$ is an estimate of the number of photoelectrons.

LIQUID HYDROGEN TARGET/ČERENKOV COUNTER

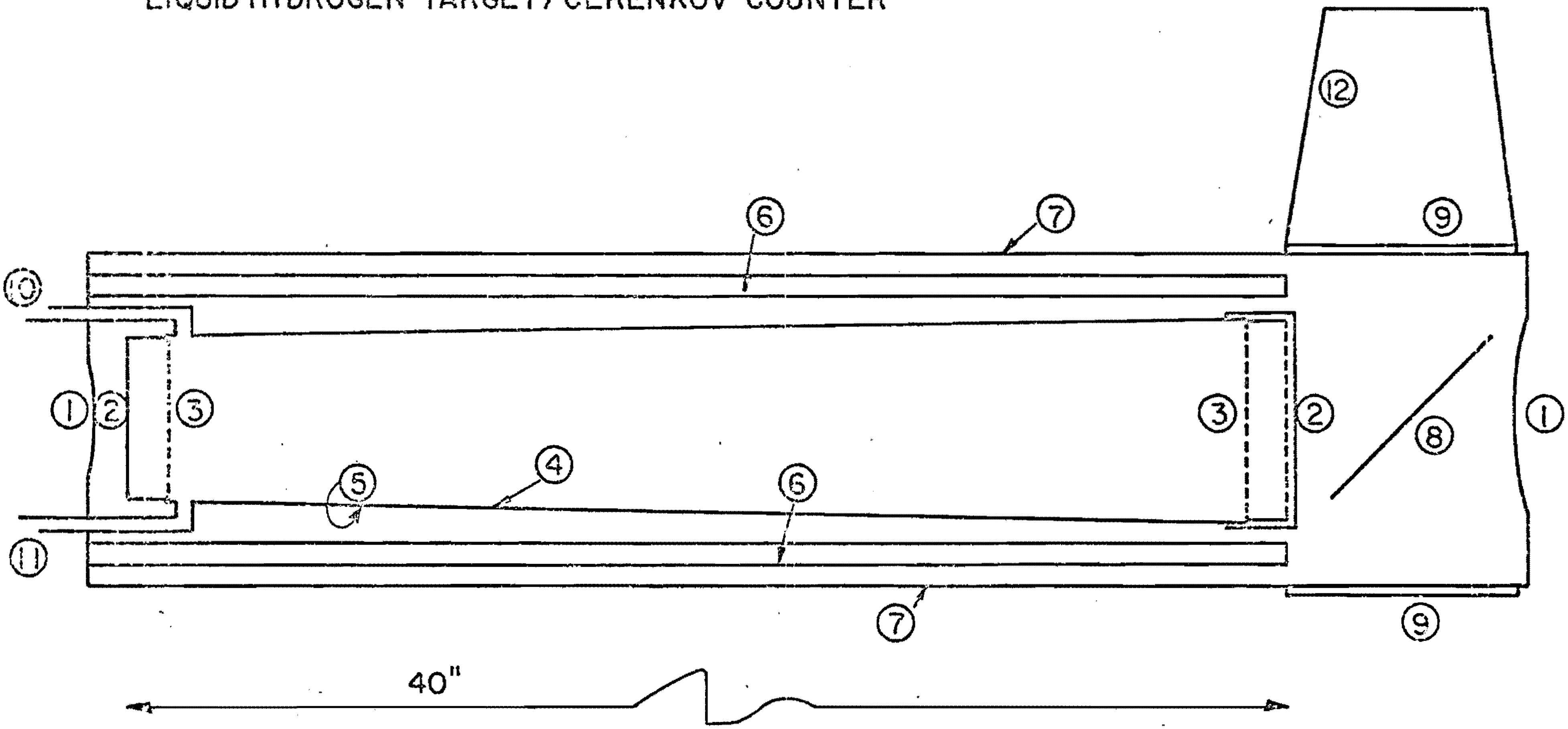

FIGURE 8

FIGURE 8. 1.0 m long liquid-hydrogen-target/Čerenkov-counter.

1. Al beam entrance/exit thin windows of thickness 5 mils.
2. Transparent mylar, target vessel thin windows, 10 mils thick.
3. Cu support rings at beam entrance/exit sides which also act as temperature equalizers.
4. Target vessel, Al, interior polished tube, 3" diameter at beam exit side and tapered down to 2" diameter at beam entrance side, 40" long.
5. Superinsulation wrapping on the exterior of target vessel surface.
6. Plastic scintillator box, four strips of 1/2 " x 4" x 40" scintillators glued together at overlapping edges. The beam exit side of each scintillator has two (1/2 " x 2") lucite adiabatic light guides. The light guides are optically coupled to small quartz windows.
7. 50 mils thick Al, radiation shield cylinder, attached to liquid nitrogen reservoir to reduce hydrogen boil-off. The radiation shield is also optically sealed.
8. Aluminized mylar reflector of Čerenkov light, oriented at 45°.
9. Quartz windows, 4" diameter, on three sides--top for Čerenkov light viewing, sides for scintillator box viewing through adiabatic light guide couplings.
10. Inlet of liquid hydrogen from reservoir.
11. Outlet of liquid hydrogen boil-off.
12. Čerenkov light 5" photomultiplier assembly.

Utilizing this magnet to full advantage, we also propose to place a simple counting system downstream where the swept primary beam would land. This counting system would serve to measure directly the beam's attenuation due to interactions in the target and make π^-, K^-, $\bar{p}$ total cross section measurements possible for the complete calibration of our experimental results. It would also serve to determine the muon contamination of the beam since the dominant hadronic components of the beam would be absorbed in a thick iron block.

We have designed this magnet with several criteria in mind. Foremost in our consideration is an optimized design which economizes the construction cost and the power consumption level. The magnet's length, aperture and field parameters are chosen to yield a matched acceptance with our multi-gamma-ray spectrometer system. At the chosen beam momenta values of our proposal, the combined acceptance of the magnet and the TASC spectrometer produces a mass acceptance of multi-gamma-ray final states with upper limits of 2.2 GeV and 3.1 GeV. Moreover, the magnet's acceptance is made flexible enough, so that the same magnet can be utilized subsequently, in the following part of our proposal which has a somewhat more stringent dependence on the performance of this magnet.

Without the use of this magnet for the detection of multi-gamma-ray final states, we would be forced to use a two-arm spectrometer system instead of the single forward-placed spectrometer in this proposal (cf. Fig. 10). This option would greatly reduce our multi-gamma-ray handling capability, severely cut our mass acceptance, remove our ability of making a spin analysis of the produced bosons, limit the detection efficiency and in general bias the data collection. We maintain that these limitations are severe and that they would not allow us to improve on previous experimental results. We are also aware that such a magnet at NAL would be very useful in several other applications and as such, we are prepared to release this magnet to NAL after its utilization in both parts of our proposed experimental work.

We have made a preliminary design of this magnet and we propose to provide this magnet at NAL. Presently and for a limited time period, at HEPL we have excellent facilities for the construction of this magnet. However, we hope that a decision from NAL would be made sufficiently early in time so that the magnet's construction schedule would not interfere with other current efforts at HEPL. We have designed this magnet, (as to the coils' current density and number of turns) such that existing NAL power supplies can be used. A pair of 500-5 NAL Main Ring power supplies is required, connected serially to power this magnet. Each power supply delivers 5000 amp. at 100 v.

The magnet's dimensions and the associated relevant information are given in Fig. 9. In both coils the number of turns is 48, 8 turns horizontally and 6 turns high, with ~ 1" x 1" conductor cross section.

The spectrometer system

Several ideas have contributed to improving our current multi-gamma-ray spectrometer configuration. These ideas will be tested and refined further during an approved testing program, SLAC Proposal No. T-56, using the SLAC 15 GeV test beam facility.

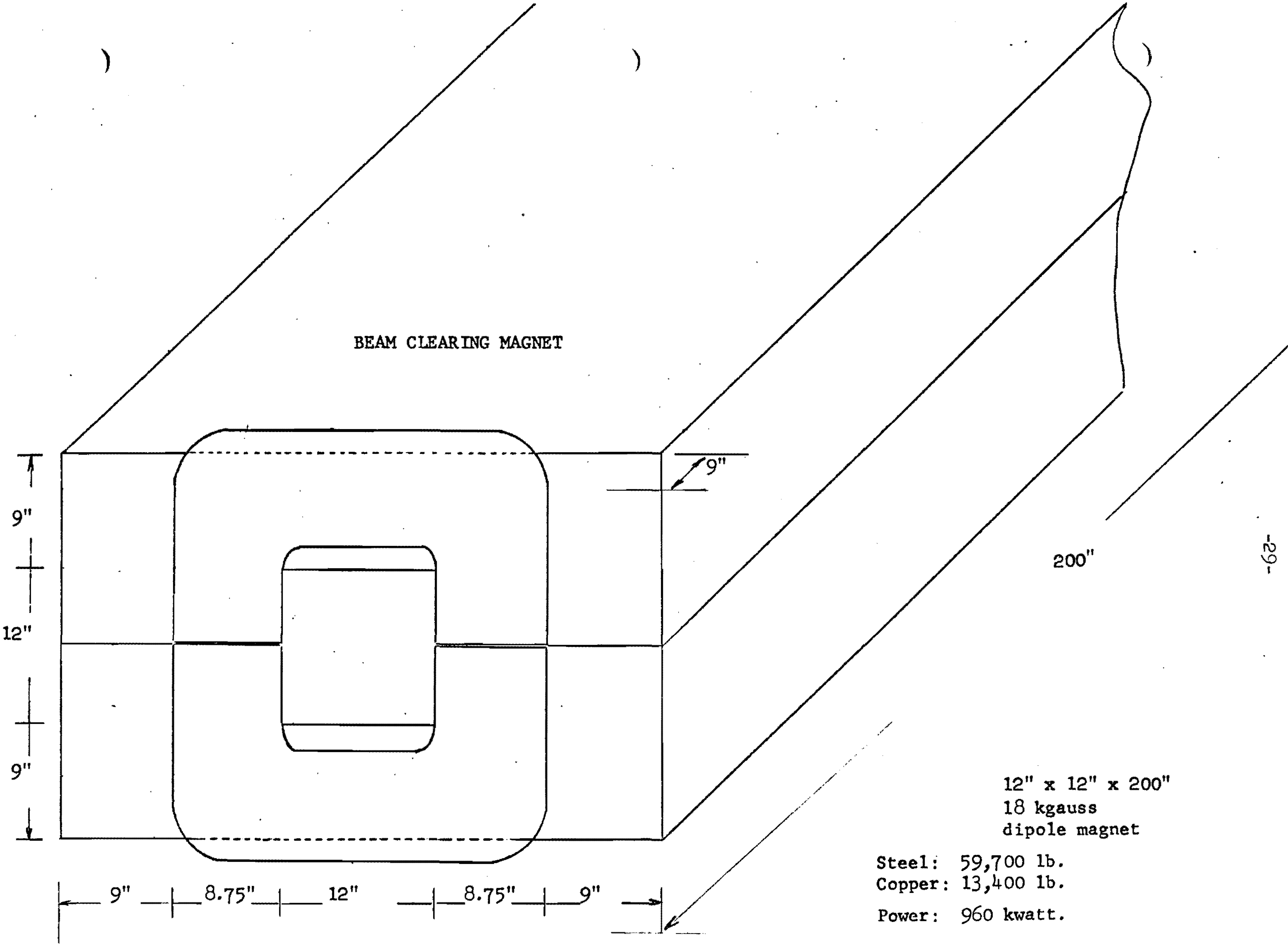

12" x 12" x 200"
18 kgauss
dipole magnet

Steel: 59,700 lb.
Copper: 13,400 lb.

Power: 960 kwatt.

FIGURE 9

The design principles are based on the following. On the one hand, in order to have high detection efficiency of multi-gamma-ray events the gamma-ray "live converter" should be about 4 radiation lengths thick. On the other hand, the space coordinate measurement resolution requires that we sample the gamma-to-shower conversions at an early stage in the shower's development. Although the behavior of showers on the average is very well known, individual shower characteristics fluctuate, especially with regard to in depth where a shower's maximum electron multiplicity will occur.[23] Taking present calculations into consideration, the "live converter" in our spectrometer system will be a pair of 2" thick 30" diameter NaI(Tl) crystals in separate assemblies; (the radiation length of NaI is $\simeq$ 1"). Detailed considerations of the spectrometer's modular design are based on shower fluctuation studies. These are presented in Appendix I.

The shower coordinates are recorded by multi-wire proportional chambers. At the first two "live converter" planes these chambers will contain four wire orientations, i.e.: 0°, 60°, 90°, 150°, to encode the space coordinates of several showers with a minimum of ambiguity and confusion (< 1%). The spatial resolution at this point is expected to be ± 1.0 mm. Multi-wire proportional chambers will also be used to measure individual shower pulse-heights at four different depths, defined by the "live converters" and a pair of 3.5" thick, 30" diameter, NaI(Tl) crystals. The pulse-height measuring chambers would be the same as the coordinate measuring chambers.

In one of the methods which we have investigated, in which the information is treated digitally from the beginning, this task is accomplished by connecting together successively groups of ten wires. In this case, each group would have attached to it a 4 bit pulse-height encoding electronics module. The number of wires in a group is set by the behavior of shower widths at NAL energies. The positional information is acquired by interrogating each wire separately in a conventional manner. This method not only simplifies the readout electronics but it also makes it possible to measure a shower's pulse height, especially when the shower has spread at maximum electron multiplicity. Alternately, an analog signal processing method can be used, with fast 400 MHz ECL electronics where the chambers' readout system now is based on the electromagnetic delay line principle which has been developed recently at HEPL.

The spectrometer's last module is a pair of 10" thick 30" diameter NaI($T\ell$) crystal assemblies which serve to contain totally the multi-gamma-ray generated showers at NAL energies. Using altogether ~30 radiation lengths, the mixed signals from all of the crystals form a pulse height sum TASC measurement of the total multi-gamma-ray energy. The overall experimental layout is shown in Fig. 10 and the major apparatus functions are discussed below.

Regarding the experimental arrangement displayed on Fig. 10, we remark that we plan also to take advantage of the availability of our second identical TASC-spectrometer module which we intend to use in the next phase of this proposal. Under actual experimental conditions, after examining the performance of the single module TASC arrangement, we may

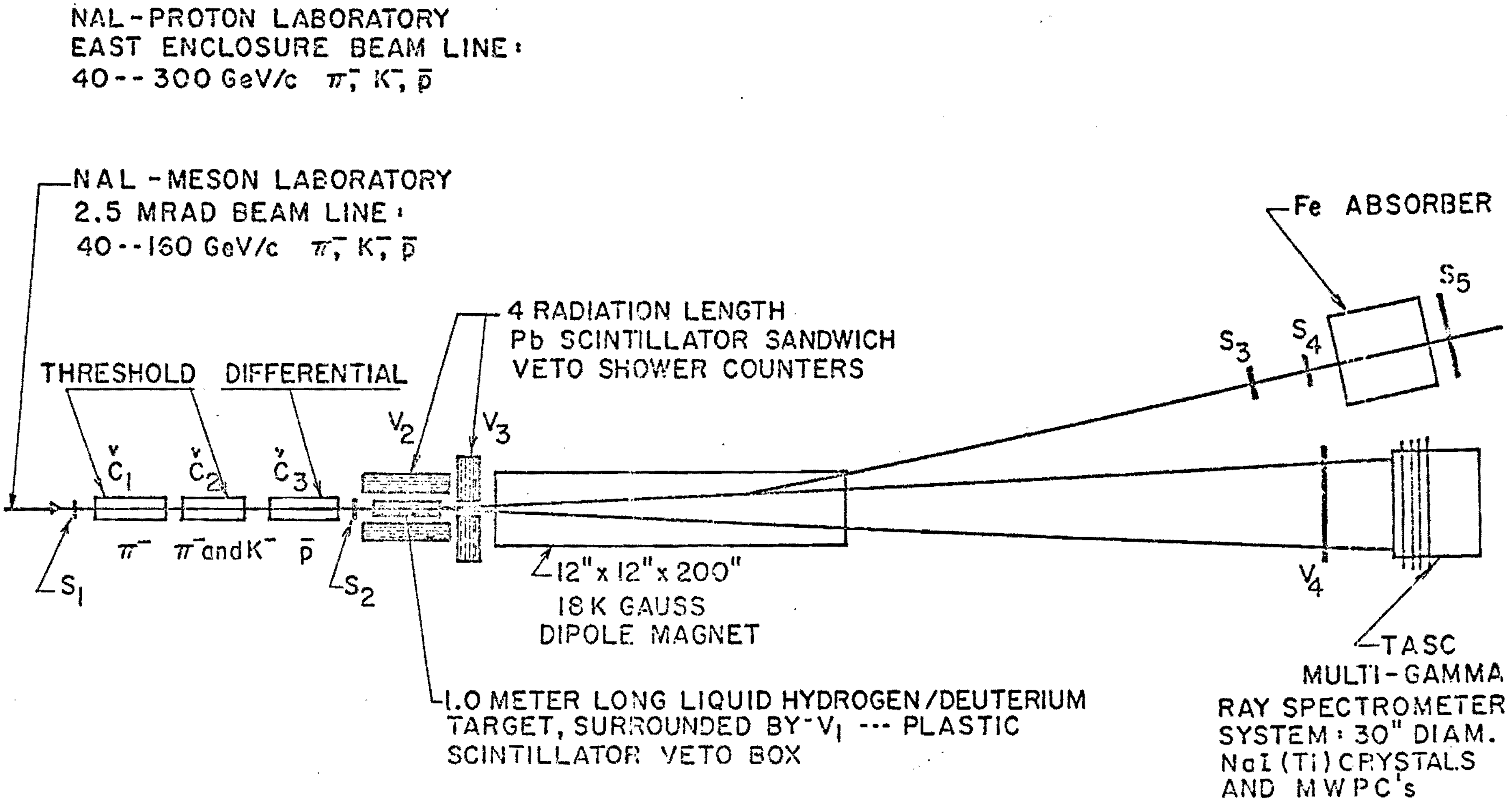

SCHEMATIC EXPERIMENTAL SETUP

(NOT TO SCALE)

FIGURE 10

wish to include the second TASC module and form an integral detector system made of two major elements. The experimental layout in this eventuality would still be the same as shown in Fig. 10.

Data Triggering Conditions and Veto Counters

In the experimental arrangement displayed in Fig. 10, a valid-beam trigger is derived with the help of beam telescope counters, $S_1 - S_5$, and the three (or two) Čerenkov counters. For valid event triggers, the beam is defined by the condition of $B_1 = S_1 \cdot S_2 \cdot \overline{S_3} \cdot \overline{S_4} \cdot \overline{S_5}$. Beam attenuation due to interactions at the target is obtained by the signal $B_2 = S_1 \cdot S_2 \cdot S_3 \cdot S_4 \cdot \overline{S_5}$, to yield a total cross section target transmission measurement $\sim B_1/B_2$. The muon contamination of the beam is monitored by detecting transmission through a thick iron absorber and the signal $B_3 = S_1 \cdot S_2 \cdot S_3 \cdot S_4 \cdot S_5$. In the case of the 2.5 mrad beam line usage, two gas threshold Čerenkov counters and one differential Čerenkov counter would be used, all of which already are a part of this beam transport system. In the case of the Proton Laboratory's East Enclosure beam line usage, only two gas threshold Čerenkov counters would be used. As shown in Fig. 10, the beam's dominantly hadronic components are signaled by having $\check{C}_1$ just below the kaon threshold and $\check{C}_2$ just below the proton threshold, while $\check{C}_3$ is set differentially on $\overline{p}$'s. Thus, the signals are: $\pi^- = \check{C}_1 \cdot \check{C}_2 \cdot (\overline{\check{C}_3})$; $K^- = \overline{\check{C}_1} \cdot \check{C}_2 \cdot (\overline{\check{C}_3})$ and [and $\overline{p} = \overline{\check{C}_1} \cdot \overline{\check{C}_2} \cdot \check{C}_3$]. The information from these Čerenkov counters are recorded by gated latches and examined during the data analysis phase of our experiment.

In the case of neutral final states, the 1.0 meter long liquid hydrogen target's Čerenkov radiation pulse height signal, $\check{C}_T$ is proportional to an event's position. The $\check{C}_T$ pulse height distribution will have a characteristic peak due to beam non-interacting tracks, traversing the entire target length. Higher pulse height values, beyond this peak, are due to beam interacting tracks, producing charged particles at the target. Lower pulse height values, below this peak, are due to beam interacting tracks, producing neutrons and multi-gamma-ray final states. After a full spectrum is generated experimentally, the $\check{C}_T$ signals would be discriminated differentially and encoded digitally.

The veto counters are designated V_1 - V_4 on Fig. 10. The plastic scintillator box, V_1 surrounds the liquid hydrogen target cell, inside the target's radiation shield (cf. Fig. 8). This counter is most sensitive to the presence of slow charged particles which are produced at the target coincident with a valid beam trigger. The 4-5 radiation length lead-scintillator sandwich type veto counters, V_2 and V_3 are sensitive to the presence of faster charged particles and large angle π^o's but they are ~ 95% transparent to neutrons. The veto counter signals are mixed to provide an overall veto V. In the case of inclusive reaction studies V is just the signal from V_4 .

The remaining trigger counters are found at the multi-gamma-ray spectrometer module (cf. Figure 1 of Appendix I). These are thin plastic scintillator trigger-counters, T_1 - T_4 which serve to define the spectrometer's acceptance and to provide fast time pickoff to the multi-wire proportional chambers, P_1 - P_4 . Moreover, a fourfold coincidence among these, $T = T_1 \cdot T_2 \cdot T_3 \cdot T_4$ would serve to certify that electromagnetic showers, having a total energy greater than a lower limit, are generated.

Using the above counter signals, an overall event triggering signal is formed, $G = B_1 \cdot T \cdot \overline{V}$ to gate the acceptance of pulse height information from the six NaI(Tl) crystal segments and the four MWPC planes of our spectrometer. Thanks to the excellent duty cycle of the NAL accelerator, basically we do not have an electronics pileup problem, even though scintillation light in NaI(Tl) has a decay time constant of 250 nsec. We remark that our sharp energy resolution relies entirely on encoding the fast leading pulse height information of NaI(Tl) signals. Therefore, if it becomes necessary, the trailing part of this signal can be clipped [cf. Appendix I for further discussion]. By clipping the NaI(Tl) signals to a broad width of 250 nsec, our pileup rate is only 0.1% - 0.5% where the beam instantaneous rates are 5×10^6 π's/sec and 10^7 π's/sec, respectively, at a 1 meter long liquid hydrogen target.

Data Acquisition

We plan to use an on-line data acquisition and data analysis system which is basedon the DEC PDP-11/45 central processor and we plan to provide this at NAL for the proposed experimental program.

In our electronics setup, the status of all scintillation counters, the contents of scalers and the encodings of analog-to-digital converters are accumulated through core memory onto a disk storage unit, for the duration of an accelerator pulse. Subsequently, in between accelerator pulses, a preliminary data analysis is made and the condensed data is recorded on an IBM compatible magnetic tape unit. With this facility we can make several multi-parameter analyses on a real time basis and monitor the quality of the data. This capability is also essential to the initial calibration runs of NaI(Tl) crystals, multiwire proportional chambers, the shower counters and the target/Čerenkov signals. With respect to the data collection phase of the experiment we find that the available computer, with a core memory of 32 thousand words in 16 bits, and the mass storage unit and 4 direct-memory-address channels are adequate to handle several hundred events per NAL machine pulse.

REFERENCES

1. Robert Hofstadter, Science, 164, 1471 (1969).
2. T. G. Walker, NAL Summer Study 1968, volume II, p. 59.
3. J. Ballam, G. B. Chadwick, Z. G. T. Guiragossián, W. B. Johnson, D. W. G. S. Leith and K. Moriyasu, Phys. Letters 31B, 489 (1970). For a summary of VDM relations see: Zaven G. T. Guiragossián, SLAC-PUB-694 and proceedings of International Seminar of Vector Mesons and Electromagnetic Interactions, Dubna, 1969, JINR 2-4816.
4. M. A. Wahlig and I. Mannelli, Phys. Rev. 168, 1515 (1968).
5. M. Basile, D. Bollini, P. Dalpiaz, P. L. Frabetti, T. Massam, F. Nevach, F. L. Navarria, M. A. Schneegans and A. Zichichi, CERN preprint 71-1934 (1971); E. H. Harvey, E. Marquit, E. A. Peterson, T. G. Rhoades, H. Romer, K. Ruddick and J. K. Randolph, Minn-Mich, preprint 71-2018 (1971).
6. E. Shibata and M. Wahlig, Phys. Letters 22, 354 (1966).
7. M. Gourdin, CERN TH 1320 and Proceedings of International Conference on Meson Resonances and Related Electromagnetic Phenomena, Bologna, 1971.
8. M. Wahlig, E. Shibata, D. Gordon, D. Frisch, and I. Mannelli, Phys. Rev. 147, 941, (1966).
9. D. H. Miller, L. J. Gutay, P. B. Johnson, V. P. Kenney and Z. G. T. Guiragossián, Phys. Rev. Lett. 21, 1489, (1968).
10. For a summary see: D. R. O. Morrison, CERN PHYS. 71-10 (1971) and proceedings of XVth International Conference on High Energy Physics, Kiev, 1970.
11. See for examples: H. Pilkuhn, The Interactions of Hadrons, North-Holland publishing Co., Amsterdam, 1967.
12. S. J. Brodsky, T. Kinoshita and M. Terazawa, CLNS-152 preprint (1971); and D. M. Lyth Nucl. Physics, B30, 195 (1971).
13. R. P. Feynman, Phys. Rev. Lett., 23, 1415 (1969); J. Benecke, T. T. Chow, C. N. Yang and E. Yen, Phys. Rev., 188, 2159 (1969); T. T. Chow and C. N. Yang, Phys. Rev. Lett., 25, 1027 (1970).
14. J. Ellis, J. Finkelstein, P. H. Frampton and H. Jacob, CERN TH. 1316 (1971).
15. Aachen-Berlin-CERN-London-Vienna and Bruxelles-CERN Collaborations, CERN PHYS 70-52/Rev. (1971).

16. R. Ford, R. Hofstadter, E. B. Hughes, L. H. O'Neill, R. Schilling and R. Wedemeyer, HEPL, July 1971; SLAC proposal No. 79, Rev.

17. T. L. Jenkins, W. M. Smith, A. G. Strelzoff, C. R. Sullivan, D. H. Miller, S. L. Meyer, G. Micks and D. Freytag. NAL proposal No. 135, April 1971; R. Gomez, A. V. Tollestrup, R. L. Walker, D. Eartley, O. Dahl, R. Kenney, M. Pripstein and M. Wahlig, NAL proposal No. 111, February 1971.

18. O. Kofoed-Hansen and B. Margolis, Nucl. Phys. B11, 455 (1969); and E. J. Moniz, private communication (Stanford University, 1971).

19. We Thank Dr. E. J. Moniz for making this calculation and for making it avalable to us prior to publication.

20. J. F. Crawford and R. Hofstadter, Bull. Amer. Phys. Soc. 16, 658 (1971), abstract KN-10.

21. G. I. Kopylov and M. S. Khvastunov, Sov. Journ. Nucl. Phys. 4, 567 (1968), (translation).

22. E. Bertolucci, I. Mannelli, F. Martorana, G. Pierazzini, A. Scribano, F. Sergiampietri and M. L. Vincelli, Nucl. Instr. Meth. 69, 21 (1969). We thank Dr. I. Mannelli for a valuable communication on the design and performance of a liquid hydrogen target Čerenkov counter, recently applied in a CERN experiment by the Karlsruhe-Pisa group.

23. G. Backenstoss, B. D. Hyams, G. Knop and U. Stierlin, Nucl. Inst. Meth. 21, 155, (1963).

II. DEEP INELASTIC ELECTRON SCATTERING WITH A SEARCH FOR MASSIVE LEPTONS AND QUARKS ON HYDROGEN, DEUTERIUM, Cu AND Pb TARGETS

The high energy and intensity of primary proton beams at NAL, especially at the Proton Laboratory, make it possible to prepare an electron beam of high purity in the energy range of 40 - 200 GeV and with an intensity of 10^8 electrons/pulse. With sufficient care in the design of beam transport optics, we find that a good quality electron beam can be obtained such that it can be used directly on an experimental target for the purpose of studying electroproduction processes. The electron beam qualities, required for this experiment, are specified in Section B.

The large acceptance and high resolution qualities of our NaI(Tl) TASC spectrometers compensate sufficiently well for the moderate value of the NAL electron beam intensity. This is an important reason why a significant and important electroproduction experimental program can be made at NAL.

Motivated by these considerations, we are proposing an experiment for the study of deep inelastic electron scattering processes, using hydrogen deuterium, Cu and Pb targets. Concurrently, the excellent duty cycle at NAL makes it possible for us to perform coincidence measurements involving multi-gamma-ray final states by using a rather simple experimental arrangement. This arrangement is discussed in Section C. Briefly one of the arms of our spectrometer system detects scattered electrons and the other is placed to intercept one or more gamma-rays. The latter arm is set so that it is also ideally suited for the detection of quark production in electron production processes.

Together with experiments involving deep inelastic muon scattering (proposals No. 26 and 98) and wide angle electron pair production by protons (proposal No. 70), our proposed experiment would make a valuable contribution to the understanding of nucleon structure and the electron muon difference or universality. This experiment would complete and complement further the knowledge that can possibly be derived from massive photon interactions with hadrons and employs the additional benefit of our high resolution detectors to great advantage.

A. EXPERIMENTAL PROGRAM

In the past the measurement of cross sections for the inclusive scattering process:

$$e^- p \rightarrow e^- W \tag{1}$$

has revealed new knowledge on the inelastic scattering nucleon structure functions. In these studies usually only the scattered electron is detected using a single arm magnetic spectrometer system without the detection of W , the hadronic missing mass states. A major part of this effort was made at SLAC with the 8 GeV and 20 GeV spectrometers. Other important work has been done at DESY, Cornell and CEA. Similar measurements were also made at SLAC on the equivalent muon induced process:

$$\mu^- p \rightarrow \mu^- W \tag{2}$$

to test for μ - e universality in both electromagnetic processes.

Subsequently, deep inelastic electron scattering cross sections were also measured at SLAC using targets of deuterium, Be, Cu and Au. These measurements have served to examine inelastic nucleon structure function differences between protons and neutrons and to search for nuclear shadowing effects with massive virtual photons.

Deep inelastic lepton scattering is characterized by the structure functions $W_1(Q^2,\nu)$ and $\nu W_2(Q^2,\nu)$ where $Q^2 = 4\,E_0 E \sin^2(\theta/2)$ and $\nu = E_0 - E$. The double differential scattering cross section is given by:

$$\frac{d^2\sigma}{dEd\Omega} = \frac{\alpha^2}{4E_0{}^2 \sin^2(\theta/2)} \cdot (\mathrm{ctn}^2(\theta/2) \cdot W_2 + 2W_1) \quad . \quad (3)$$

The concept of scale invariance requires that the structure functions depend only on the variable $\omega = 2M\nu/Q^2$ and not have a decoupled dependence on both variables ν and Q^2 . Moreover, it is evident from equation (3) that the separation of W_1 and W_2 from cross sectional measurements requires measurements at both very small laboratory scattering angles and at large enough angles to account for the $\mathrm{ctn}^2(\theta/2)$ effect. The SLAC measurements were carried between 1.5° (the smallest angular capability of the spectrometer) and 34° with E_0 ranging between 4.5 GeV and 18 GeV. In this case, the ratio of the minimum and maximum angles in $\mathrm{ctn}^2(\theta/2)$ is 543. In practical terms, the structure functions are separately determined by collecting data at two or more electron scattering angles θ, for fixed values of the kinematical variables

E_o and E or Q^2 and W^2, where $W^2 = M^2 + 2M\nu - Q^2$ is the square of the total hadronic mass in the final state. These are called the cross-over points. An equivalent representation of relation (3) is given in terms of the virtual photon flux Γ and the virtual photon cross sections with transverse and longitudinal polarization modes, σ_T and σ_L :

$$\frac{d^2\sigma}{dEd\Omega} = \Gamma\,(\sigma_T + \epsilon\;\sigma_L) \tag{4}$$

$$\Gamma = \frac{\alpha}{4\pi^2}\cdot\frac{E}{E_o}\cdot\frac{K}{Q^2}\cdot\left(\frac{2}{1-\epsilon}\right)$$

$$W_1 = \frac{K}{4\pi^2\alpha}\cdot\sigma_T$$

$$W_2 = \frac{K}{4\pi^2\alpha}\cdot\left(\frac{\sigma_T+\sigma_L}{1+\nu^2/Q^2}\right)$$

$$R = \sigma_L/\sigma_T \quad .$$

In the above, ϵ is the longitudinal-transverse polarization ratio of massive virtual photons as provided by the scattered electrons:

$$\epsilon^{-1} = 1 + 2\tan^2(\theta/2)\cdot\left(1+\frac{\nu^2}{Q^2}\right) \quad ; \quad 0 \le \epsilon \le 1 \tag{5}$$

and K is the equivalent virtual photon energy to produce a hadronic mass W :

$$K = (W^2 - M^2)/2M \tag{6}$$

By evaluating the cross sections at the cross-over points, as a function of ϵ , the extrapolated values of these normalized cross sections effectively measure the function W_2 at $\epsilon = 1$ and W_1 at $\epsilon = 0$.

In our experimental arrangement, our spectrometers have the capability of making measurements between the electron scattering angles of $1/8^o$ and 8^o for a very wide band of scattered electron energies. At $E_o = 100$ GeV , the $\theta \lesssim 8^o$ limitation is imposed by the counting rate requirements (see Table III). Hence, in our case a very favorable lever arm is obtained in which the ratio in $\mathrm{ctn}^2 (\theta/2)$ is 4050, and cross-over point cross sections can be derived as a function of ϵ , in the range $0.5 \lesssim \epsilon \lesssim 1$.

Figure 1 summarizes the results [1,2] obtained at SLAC from studies of reaction (1) and (2). In Fig. (1b) the ratio of experimental cross sections from muons divided by those from electrons are indicated as ρ . Recently a thorough review on the search for electron muon differences has been presented.[3]

As is demonstrated below, our proposed experimental arrangement together with a good quality electron beam at NAL will make it possible for us to acquire electron data of equal statistical and kinematical significance comparable with those obtained with muons for which a large momentum-acceptance magnetic spectrometer system is used at NAL (cf. proposal No. 98). The two experiments will be very significant in making detailed electron-muon comparisons.

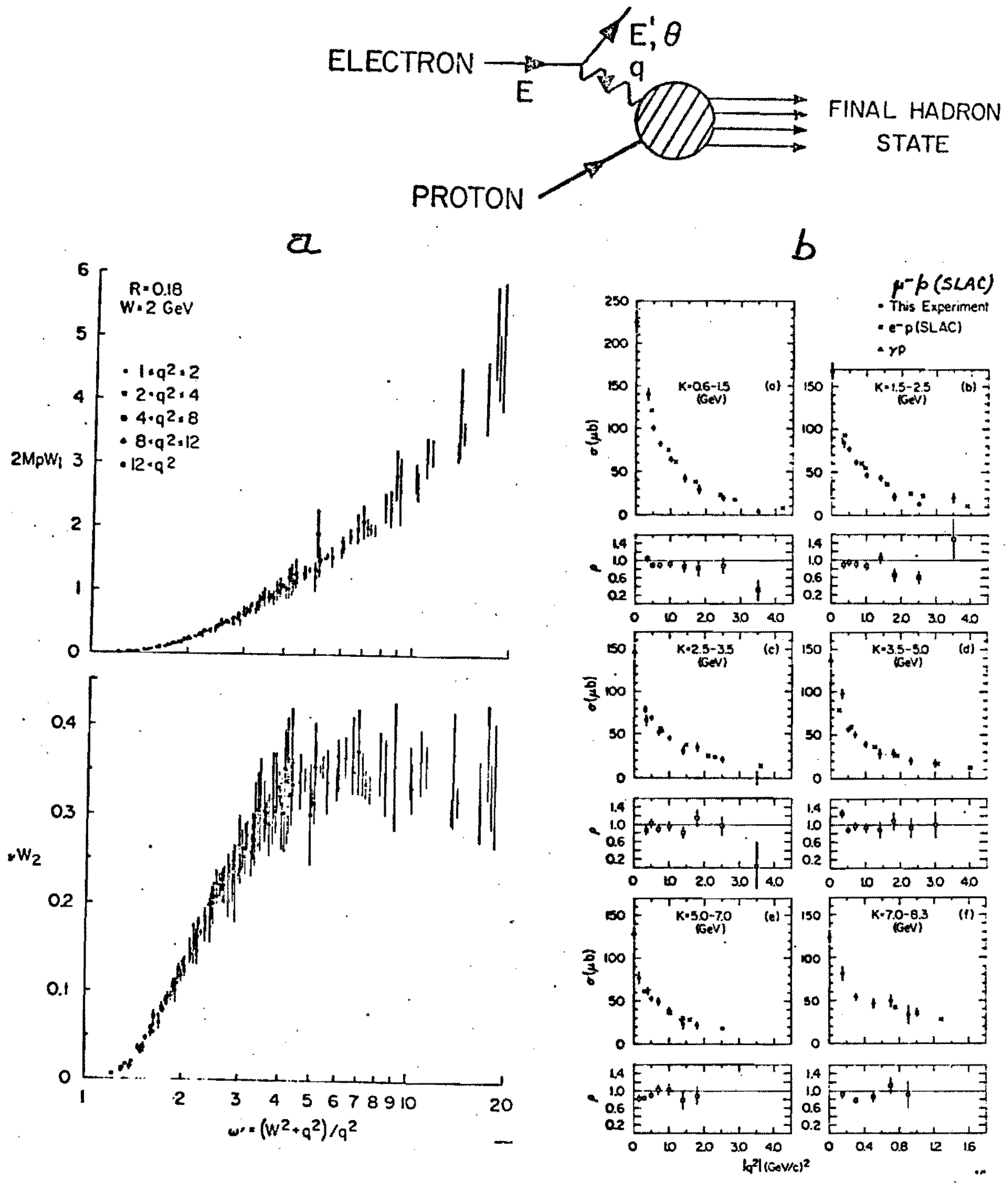
ELECTRON
E
E', θ
q
PROTON
FINAL HADRON STATE
a
R=0.18
W>2 GeV
1<q²<2
2<q²<4
4<q²<8
8<q²<12
12<q²
2MpW₁
νW₂
ω' = (W²+q²)/q²
b
μ⁻p (SLAC)
This Experiment
e⁻p (SLAC)
γp
σ(μb)
ρ
K=0.6-1.5 (GeV) (a)
K=1.5-2.5 (GeV) (b)
K=2.5-3.5 (GeV) (c)
K=3.5-5.0 (GeV) (d)
K=5.0-7.0 (GeV) (e)
K=7.0-8.3 (GeV) (f)
|q²| (GeV/c)²

FIGURE 1

TABLE I

RELATIVE RATE COMPARISON OF DEEP INELASTIC ELECTRON AND MUON SCATTERING EXPERIMENTS AT NAL

	This Proposal: electrons	Proposal 98: muons
Beam Intensity with 10^{13} interacting protons/pulse	10^8	5×10^6
Geometric acceptance $\Delta \phi/2\pi$	0.15 - 1.0 average: 0.25	1.0
LH_2 target length (m)	0.25	1.0
$I \cdot \Delta\phi/2\pi \cdot t$	6.25×10^6	5×10^6

Our experimental arrangement is also designed to have our detectors be sensitive to small electron scattering angles and a wide range of Q^2 values. The various kinematical region acceptances are displayed in Section C on Experimental Method. We wish to stress that the small angle measurements in our case, namely $\theta \simeq 1/8^\circ - 1^\circ$, will be very useful for the determination of total hadronic photoproduction cross sections $\sigma_{tot}(\gamma p)$ and $\sigma_{tot}(\gamma n)$, obtained by a $Q^2 \rightarrow 0$ extrapolation procedure to yield the cross sections of equivalent real photons. This method has been tested at SLAC and provided an independent measurement of these cross sections as a function of equivalent photon energy K, given by relation (6). Figures 2 (a-d) show the extrapolation method used in small angle electroproduction measurements and Figures 3 (a,b) display the abstracted photoproduction cross sections from the 20 GeV spectrometer work in comparison with other

FIGURE 2

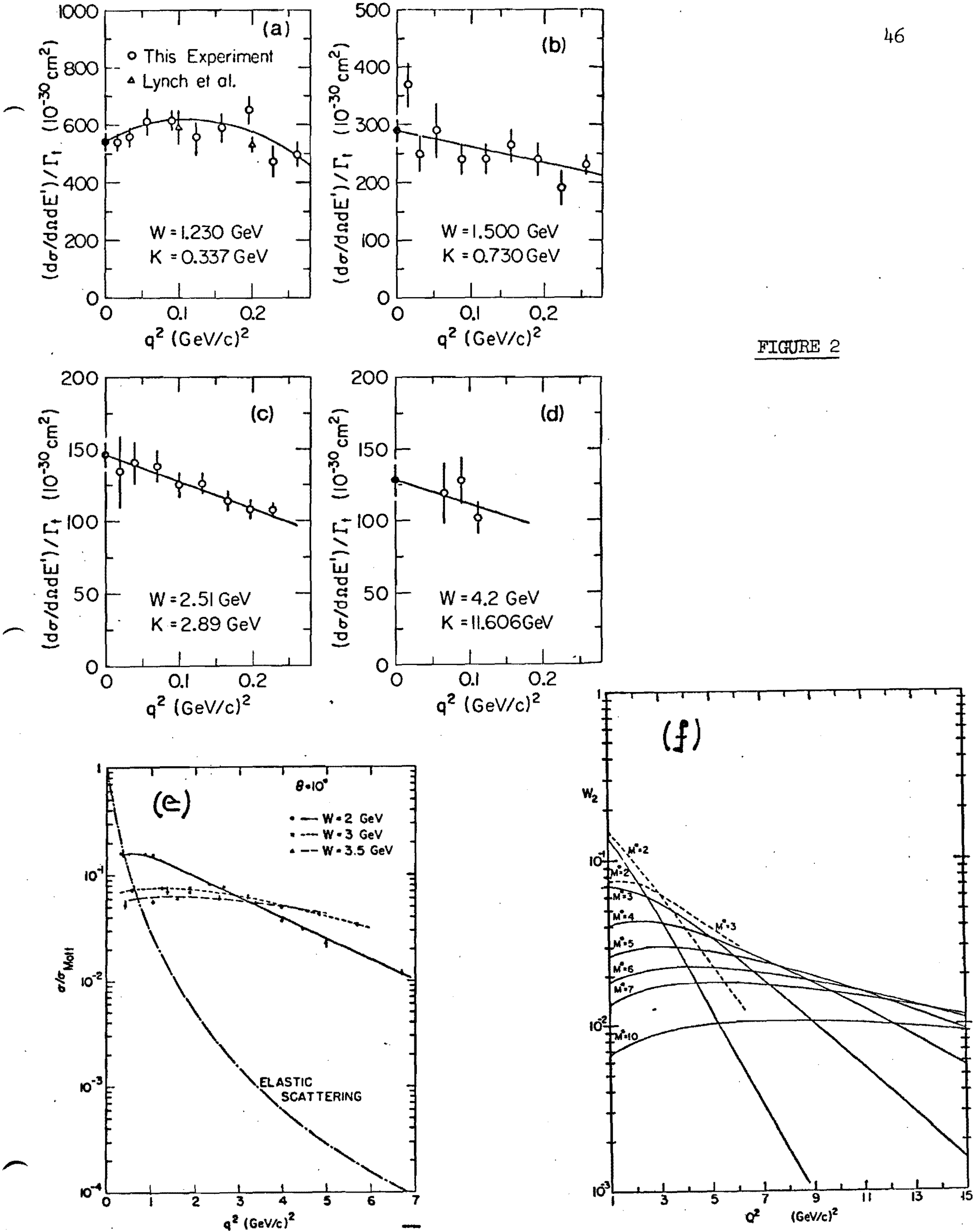

Numerical results for $W_2(Q^2,\nu)$ at fixed M^*,
H.T.Nieh and J.M.Wang Phys.Rev.Lett. 26,1139 (1971).

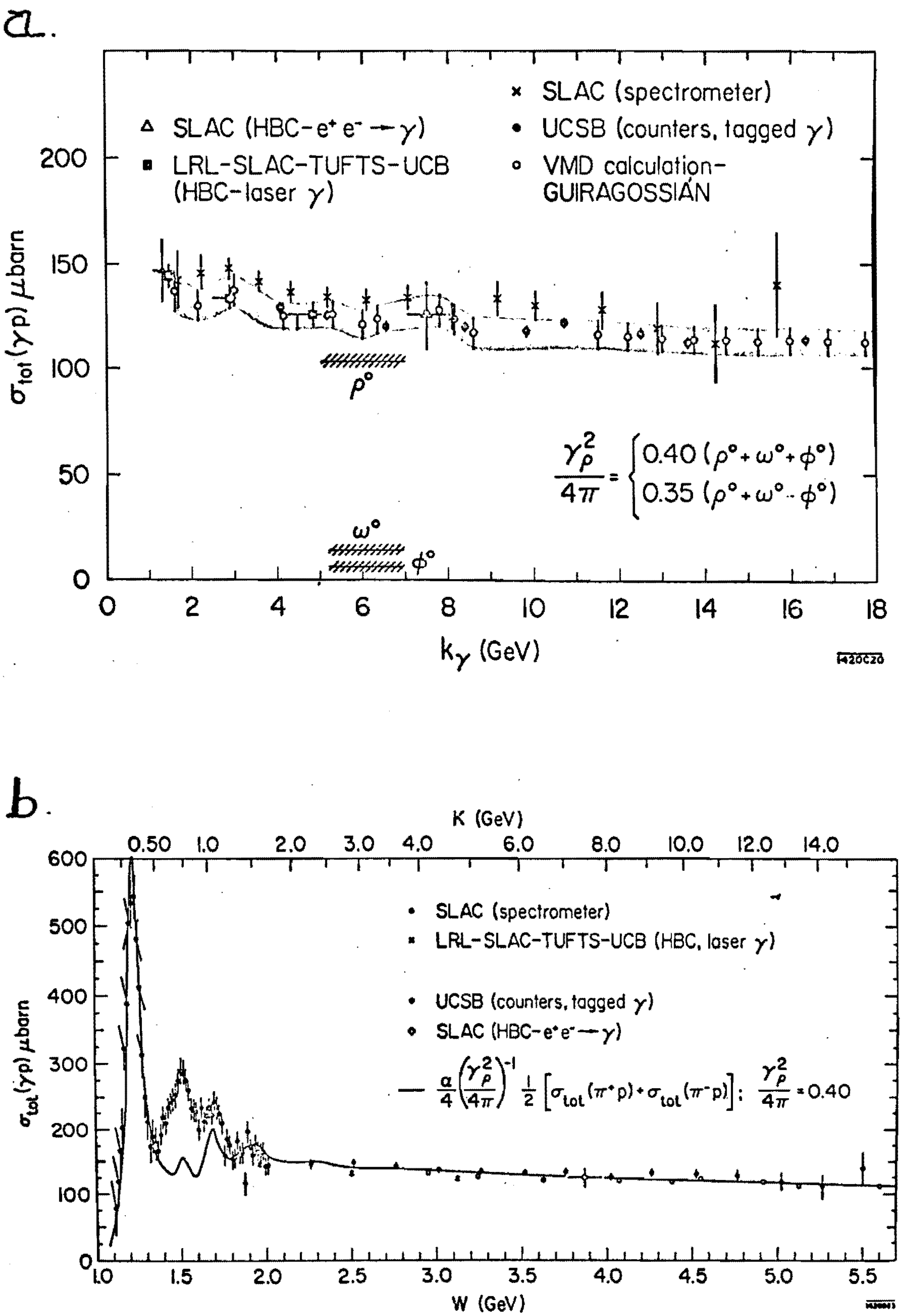
a.
× SLAC (spectrometer)
△ SLAC (HBC-e⁺e⁻ → γ)
● UCSB (counters, tagged γ)
■ LRL-SLAC-TUFTS-UCB (HBC-laser γ)
○ VMD calculation-GUIRAGOSSIAN
σ_tot (γp) μbarn
0
50
100
150
200
0
2
4
6
8
10
12
14
16
18
k_γ (GeV)
ρ°
ω°
φ°
γ_ρ²/4π = 0.40 (ρ° + ω° + φ°)
0.35 (ρ° + ω° - φ°)
1420C20
b.
K (GeV)
0.50
1.0
2.0
3.0
4.0
6.0
8.0
10.0
12.0
14.0
• SLAC (spectrometer)
× LRL-SLAC-TUFTS-UCB (HBC, laser γ)
• UCSB (counters, tagged γ)
◇ SLAC (HBC-e⁺e⁻ → γ)
— a/4 (γ_ρ²/4π)⁻¹ ½ [σ_tot(π⁺p) + σ_tot(π⁻p)]; γ_ρ²/4π = 0.40
σ_tot (γp) μbarn
0
100
200
300
400
500
600
1.0
1.5
2.0
2.5
3.0
3.5
4.0
4.5
5.0
5.5
W (GeV)

FIGURE 3

measurements from photon beams. It would be very important to make a similar comparison at NAL energies (cf. proposal No. 25) to check for consistency of results obtained by two independent methods of measurements [cf. Fig. 1(b)]. A similar comparison also applies with muon production derived cross sections [cf. proposal No. 98].

Deep inelastic electron scattering measurements on deuterium targets are almost as important as those on hydrogen targets. Cross sections from both targets are required for the probing of neutron structures and the sorting out of several theoretical models which are too numerous to be discussed here. Recent SLAC measurements from hydrogen and deuterium targets [4] are shown in Figures 4(a), 5(d), 6(a,b), as a function of several scaling variables. The relevant information is found in the variation of the structure function ratio W_2^n/W_2^p as a function of $x = Q^2/2M\nu$ [cf. Fig. 4(a)] and in the behavior of the difference $\nu W_2^p - \nu W_2^n$ [cf. Fig. 5(d)] as a function of x, ω, or another scaling variable.

In contrast to the above work on nucleons, deep inelastic electron scattering measurements on targets of complex nuclei are designed to reveal new knowledge on the nature of photons and their interaction mechanism with nuclear matter. In some respect, far more fundamental questions are raised by such measurements. For example, recent measurements of this type on Be, Cu and Au targets [4] show no evidence of nuclear shadowing in the case of massive virtual photon interactions [see Fig. 4(b-d)] whereas, nuclear shadowing effects are observed in the case of real photon interactions [5] with nuclear matter. Both types of experiments

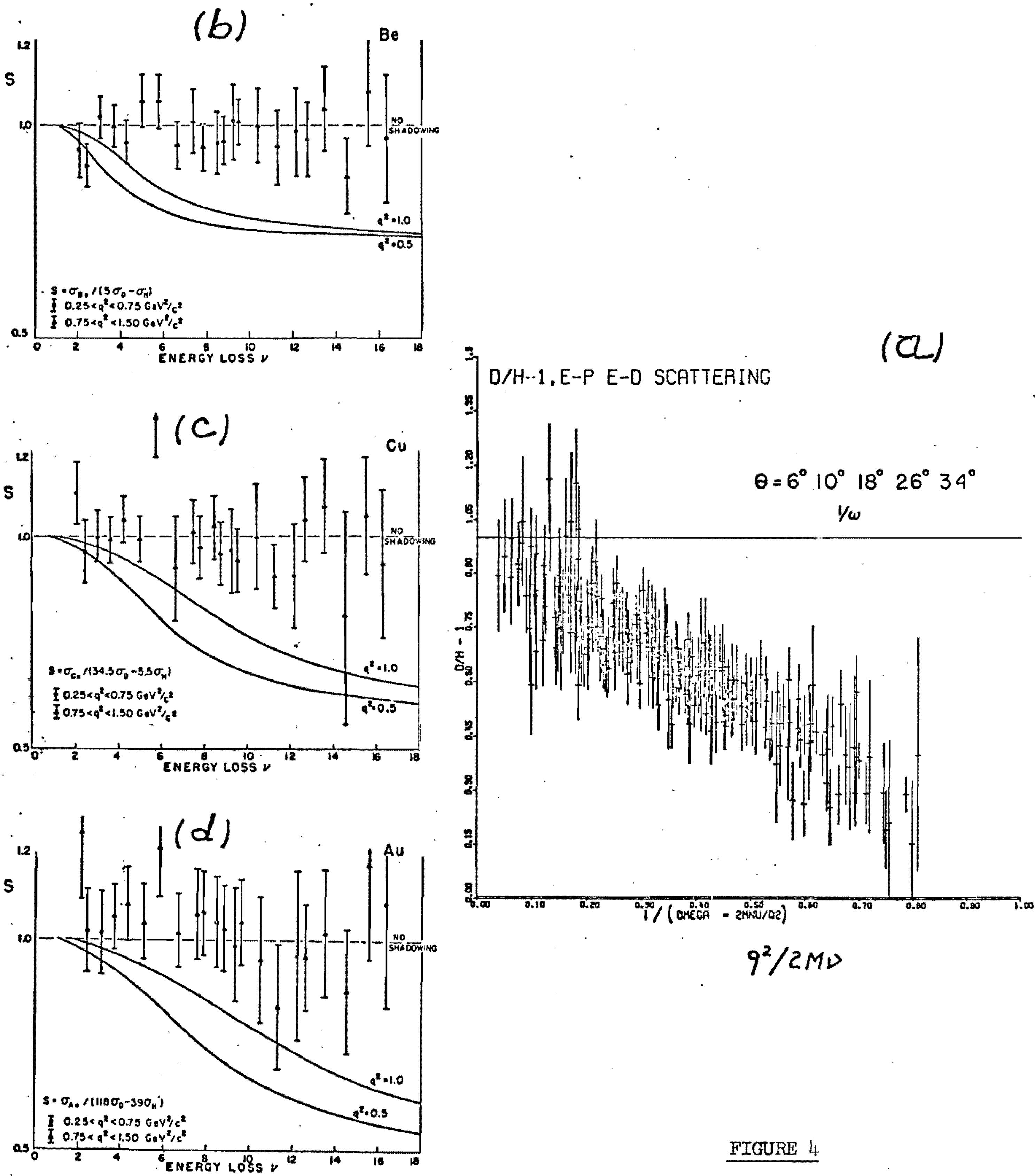
(b)
Be
S
1.2
1.0
0.5
NO SHADOWING
$q^2=1.0$
$q^2=0.5$
$S=\sigma_{Be}/(5\sigma_D-\sigma_H)$
$0.25<q^2<0.75$ GeV^2/c^2
$0.75<q^2<1.50$ GeV^2/c^2
0 2 4 6 8 10 12 14 16 18
ENERGY LOSS ν
(c)
Cu
S
$S=\sigma_{Cu}/(34.5\sigma_D-5.5\sigma_H)$
$0.25<q^2<0.75$ GeV^2/c^2
$0.75<q^2<1.50$ GeV^2/c^2
ENERGY LOSS ν
(d)
Au
S
$S=\sigma_{Au}/(118\sigma_D-39\sigma_H)$
$0.25<q^2<0.75$ GeV^2/c^2
$0.75<q^2<1.50$ GeV^2/c^2
ENERGY LOSS ν
(a)
D/H--1, E-P E-D SCATTERING
$\theta=6°$ 10° 18° 26° 34°
1/ω
D/H - 1
1.0 1.35 1.20 1.05 0.90 0.75 0.60 0.45 0.30 0.15 0
0.00 0.10 0.20 0.30 0.40 0.50 0.60 0.70 0.80 0.90 1.00
1/(OMEGA = 2MNU/Q2)
$q^2/2M\nu$

FIGURE 4

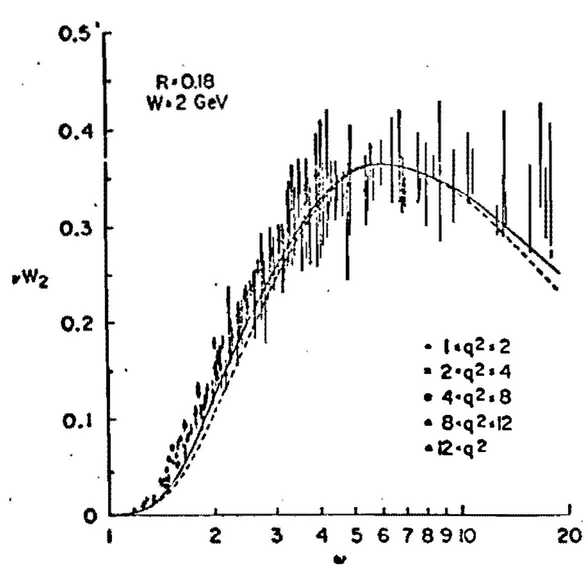

a). Structure function νW_2 for ep scattering - comparison of theory and experiment. The solid curve is νW_2 calculated from eq. (7), with $\bar{n}_1 = 0.5$, plus about 15% contribution from $n\rho^+$ channel, i.e. $\nu W_2\sigma_L/(\sigma_L+\sigma_T)$, as calculated by Lee. For $1 < \omega \lesssim 2$, this curve gives the asymptotic positions of the experimental points. The dashed curve is νW_2 of eq. (7) alone, with $\bar{n}_1 = 0.6$.

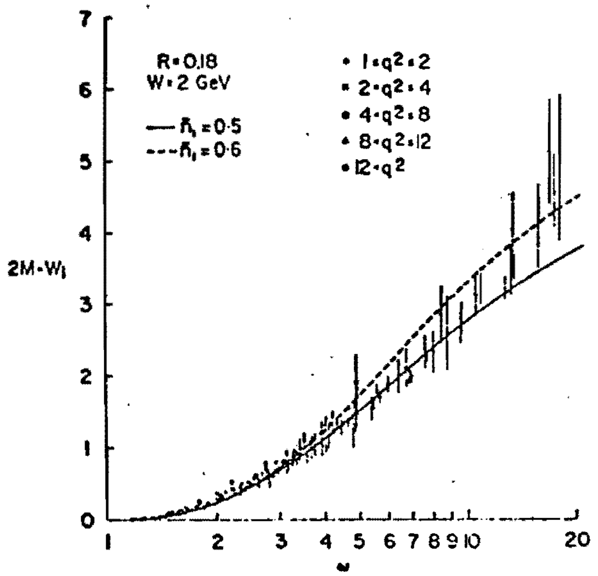

b). Structure function $2MW_1$ for ep scattering - comparison of theory and experiment. The solid curve is the theoretical curve calculated from νW_2 of eq. (7) with $\bar{n}_1 = 0.5$ gives simultaneous good fits to $2MW_1$ and νW_2.

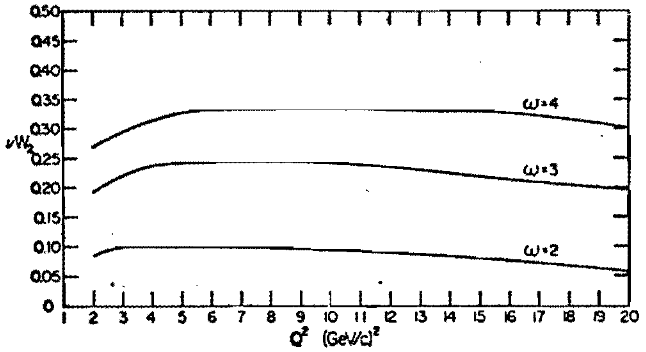

c). Numerical results for $W_2(Q^2,\nu)$ at fixed ω

H.T.Nieh and J.M.Wang Phys.Rev.Lett. 26,1139 (1971).

d).

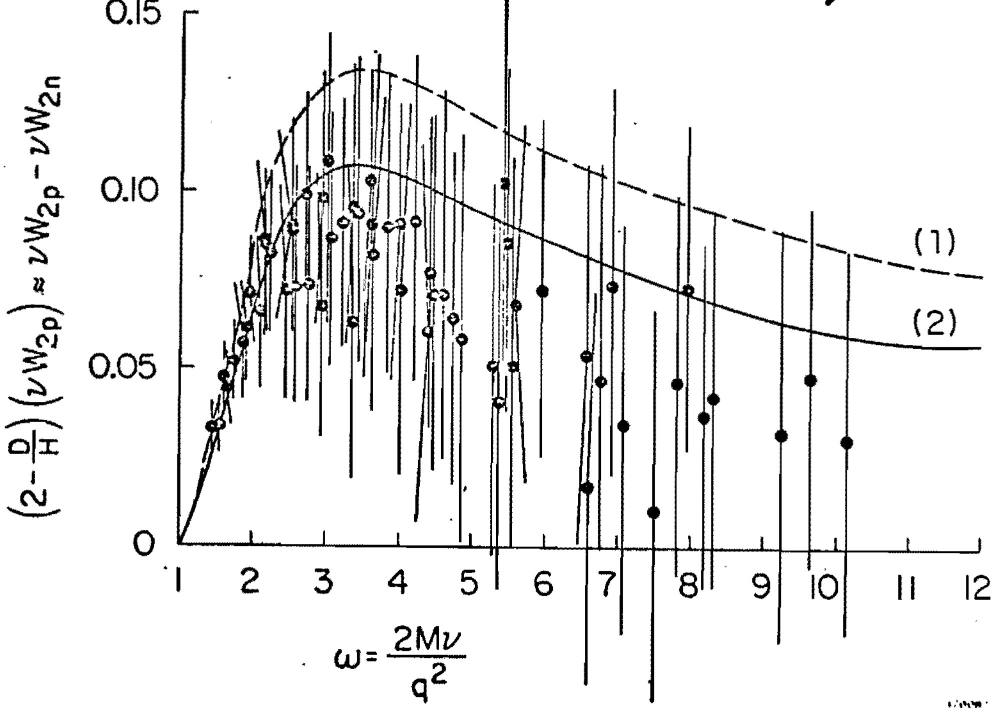

FIGURE 5

FIGURE 6

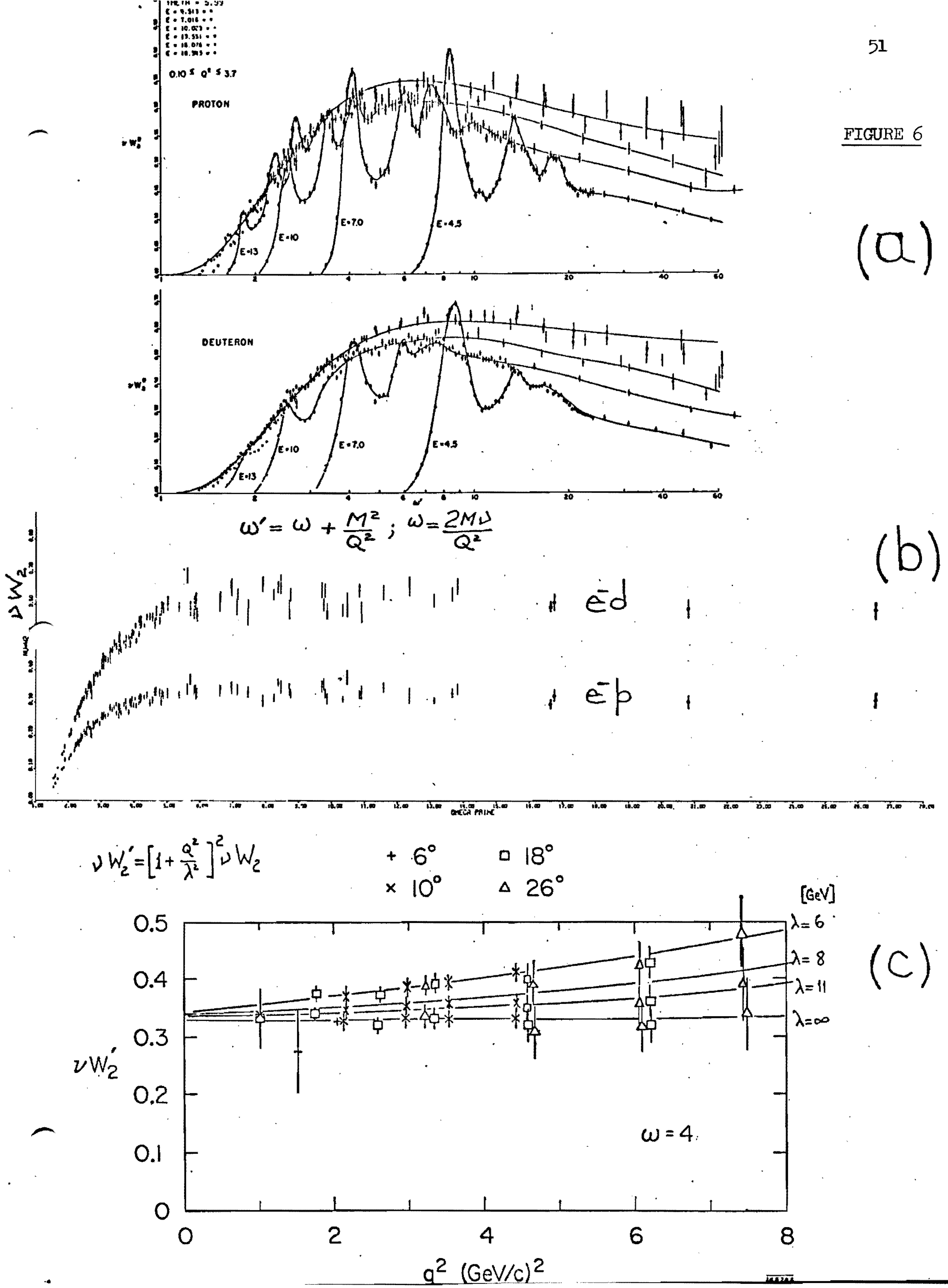
(a)
0.10 ≤ Q² ≤ 3.7
PROTON
DEUTERON
νW₂
E=13
E=10
E=7.0
E=4.5
ω
ω' = ω + M²/Q² ; ω = 2Mν/Q²
(b)
νW₂
e⁻d
e⁻p
OMEGA PRIME
(c)
νW₂' = [1 + Q²/λ²]² νW₂
+ 6°
□ 18°
× 10°
△ 26°
[GeV]
λ = 6
λ = 8
λ = 11
λ = ∞
νW₂'
ω = 4
0.5
0.4
0.3
0.2
0.1
0
0
2
4
6
8
q² (GeV/c)²

are required to reach an understanding of the hadronic components in photon interactions and to probe the space-time structure of real and massive photon absorption phenomena in nuclear matter.[6]

These are some of the reasons why we are motivated to measure deep inelastic electron scattering cross sections on deuterium as well as on Cu and Pb targets, under identical experimental conditions as those of hydrogen.

We are also very much interested in examining the coincidence spectrum of scattered electrons with multi-gamma-ray final states. The sharp energy resolution of our detectors permit the separation of inclusive electroproduction channels from channels having fixed masses in the final states. As is shown in the first part of our proposal, the good space resolution and energy resolution of the spectrometer modules are designed to identify fixed mass components in a multi-gamma-ray system. The coincidence is obtained between two arms of our spectrometer system, one which detects electrons and the other multi-gamma-ray final states. Therefore, concurrently with measurements of deep inelastic electron scattering, the following reactions will be studied also:

$$e^- p \rightarrow e^- \gamma\, p \qquad (7)$$

$$e^- p \rightarrow e^- \gamma (M\,M) \qquad (8)$$

$$e^- p \rightarrow e^- \pi^o p \qquad (9)$$

$$e^- p \rightarrow e^- \pi^o (M\,M) \qquad (10)$$

The wide angle bremsstrahlung (WAB) process of reaction (7) should be studied carefully at NAL energies because it may reveal a breakdown of quantum electrodynamics (QED) for either time-like or space-like momentum transfer regions of lepton propagators. The breakdown in QED could occur quite abruptly as a function of the time-like momentum transfer:

$$q_t^2 = M_{e'\gamma}^2 = 4\, p'k \sin^2 (\theta_{e'\gamma}/2) \tag{11}$$

where $\theta_{e'\gamma}$ is the angle between the outgoing electron and gamma-ray with energies of p' and k. This type of QED breakdown would be due to the formation of massive lepton states[7] in the form of excited electrons:

$$e^{-*} \rightarrow e^- \gamma \ . \tag{12}$$

We distinguish such states from those of "heavy" leptons where new types of neutrinos associated with these "heavy" leptons should also exist. The "massive" leptons in the form of excited electrons would still be associated with the electron neutrino.

Recently, experiments have been performed with electrons at the Cornell electron accelerator[8] and with muons at BNL[9] to study the WAB process. In these experiments QED has been found to be valid up to a mass of $M_{e'\gamma} \simeq 1$ GeV.

We find that there are compelling reasons why the experimental investigation of QED breakdown should be made concurrently with the experimental exploration of scale invariance breakdown in deep inelastic electron scattering. There are possible reasons to expect that the scale invariance breakdown, in the behavior of the structure function νW_2 $(\omega = 2M\nu/Q^2)$, might just be a reflection of modifications in QED at large

Q^2 values.[10] That is, the introduction of a Q^2 dependence in νW_2, could be due entirely to a QED modification of the propagator function in the one photon-exchange Feynman diagram. This point is illustrated in Fig. 6(c) with several values of the QED cut-off parameter, λ .

Reaction (7) is described by two Bethe-Heitler diagrams, the WAB process with time-like and space-like lepton propagation, and the interference of these with the virtual photon Compton scattering diagram. As a function of M, the propagator virtual electron mass and Q^2_N , the momentum transfer to the target nucleus, the WAB cross section is given by:

$$\sigma \sim \frac{1}{Q_N^4} \cdot \left(\frac{1}{M^2 - m_e^2}\right)^2 . \qquad (13)$$

To estimate a cross section at large values of M, we rely on the higher energy measurements of 12 GeV muon bremsstrahlung.[9] At NAL energies, kinematically lower Q^2_N values are accessible to us than it is in the above experiment. The minimum value of Q^2_N has the following energy dependence:

$$Q^2_N(\mathrm{min}) = \left[\frac{(M^2 - m_e^2)}{2E_o}\right]^2 . \qquad (14)$$

Therefore, the experimental rates at NAL energies are increased substantially for this process. Without taking into consideration this enhancement, we estimate that the WAB cross section, as a function of the virtual propagator electron mass M, is given by:

$$\frac{d\sigma}{dM} \cong 2.5 \times 10^{-33} \left(\frac{1\ \text{GeV}}{M}\right)^{4} \quad [\text{cm}^2/\text{GeV}] \qquad (15)$$

or at a value of $M = 8$ GeV, $d\sigma/dM \simeq 1.5 \times 10^{-36} [\text{cm}^2/\text{GeV}]$. The WAB rates compare favorably with the rates of deep inelastic electron scattering [cf. Table III].

Due to the total energy constraint in reaction (7), the experimental investigation of this process, at NAL energies, is made possible by the good energy resolution in both arms of our spectrometer system and the good quality electron beam transport system envisaged in this proposal.

The cross section estimates of reactions (8-10) could not be made with the available meager experimental information. Also, theoretically these are very model dependent. We estimate that the rates of these reactions are at about the 5% level of the total electron deep inelastic scattering rates. Coincidence measurements of this type, until now were not made possible at higher energies where the final states are free of resonance formation.

We remark that in one of the experimental arrangements, discussed in Section C, a configuration is obtained which is also ideally suited for the detection of quarks. The pair porduction of quarks might occur at high Q^2 values associated with deep inelastic electron scattering. With increasing Q^2's, the size of virtual massive photons may decrease[11] as $\sim Q^{-1}$ and the virtual photons become finer probes for the exploration of constituents in the structure of nucleons. In the proposed experimental configuration following the production target, "potential quarks" are magnetically selected and intercepted by one of the arms of our spectrometer system. The quarks would be detected by the amount of their energy loss in thick segments of

NaI(Tl) crystals. For this purpose, we have devised a signal analysis method for the six segments of NaI(Tl) crystal scintillators where the Landau tail is entirely eliminated in the energy loss pulse height distribution. This method is also presented in Section C.

At the large Q^2 values which are experimentally accessible at NAL energies and electron beam intensities, the radiative cross sections for electron and muon deep inelastic scattering are essentially the same. This can be appreciated in a better way by evaluating the equivalent radiator formula for the case of electrons and muons:

$$t = \frac{3}{4}(\alpha/\pi)[\ell n(Q^2/m_\ell^2) - 1] \qquad (16)$$

where, at $Q^2 = 20(\text{GeV}/c)^2$, we obtain a value of $t = 0.0201$ (in radiation length units) for muons and a similar value of $t = 0.053$ for the case of electrons. This result supports further the feasibility of our proposed electron experiment at NAL and it also places the electron-muon comparison work at NAL on equal levels of experimental simplicity.

The radiative corrections for deep inelastic lepton scattering are formulated and programmed in a detailed fashion.[12] These corrections necessarily include the radiative tail contribution of elastic lepton scattering at radiatively reduced incident energies. The following is nearly the radiative correction procedure: The measured cross sections are corrected first for the straggling in the target of incident and scattered electrons and for the internal bremsstrahlung effect. Next, the elastic scattering radiative tails are subtracted from the above corrected cross sections. Fully corrected cross sections are obtained for deep inelastic lepton scattering and these are used to make the structure function separation and theoretical comparisons. Table II lists the radiative correction effects in the experimental cross section of electrons and muons at a typical kinematical region.

Although we could use a 1.0 meter long liquid hydrogen target at high Q^2 scattering regions, we prefer to be conservative and propose to utilize a 25 cm long LH_2 target. It may also be possible that we would use either one of these target lengths, in the different configurations of our experimental arrangements. One might be used for the high Q^2 region and the other for the low Q^2 scattering. Both configurations are discussed in Section C. We remark that thin hodoscope elements would be located at the last stage of the electron beam transport system, as is discussed in Section B. During the experiment's analysis, radiative effects due to these elements can be treated in the same manner as those caused by the thin windows of the liquid hydrogen target.

For the purpose of radiative corrections as well as the strong physics interest, we plan to run at 40 GeV intervals, in the range of 40-200 GeV electron beam energies. The five electron beam settings, at 40 GeV, 80 GeV, 120 GeV, 160 GeV and 200 GeV, and at about the same intensity level of 10^8 electron/pulse can be reached by a proton beam starting with 200 GeV and going up to 500 GeV.

We have made counting rate estimates for several electron scattering angle spectrometer acceptance settings. These are based upon the integration of equation (3) in the approximation where we ignore the contribution of W_1 and take $\nu W_2 \simeq 1/3$:

TABLE II

TYPICAL VALUES OF RADIATIVE CORRECTIONS FOR DEEP INELASTIC ELECTRON AND MUON SCATTERING, DUE TO CONTRIBUTIONS FROM THE ELASTIC SCATTERING TAIL AND, STRAGGLING OF INCIDENT AND SCATTERED LEPTON.

(Cross sections are given in units of 10^{-36} cm^2/GeV/sterad)

```
ANGLE =  3.0  DEGREES       ES = 160.00  GEV

 ELASTIC RADIATIVE TAIL

     EP           TAILEL             TAILMU



   12.97        3.973D 03         2.521D 03
   25.94        4.141D 02         3.806D 02
   38.91        1.105D 02         1.085D 02
   51.88        4.001D 01         3.976D 01
   64.85        1.613D 01         1.609D 01
   77.81        6.596D 00         6.586D 00
   90.78        2.480D 00         2.477D 00
  103.75        6.863D-01         6.855D-01
  116.72        6.431D-02         6.389D-02
  123.47        5.107D-03         4.539D-03
  123.72        4.531D-03         3.947D-03
  123.98        4.028D-03         3.425D-03
  124.24        3.590D-03         2.968D-03
  124.50        3.215D-03         2.570D-03
  124.76        2.898D-03         2.228D-03
  125.02        2.642D-03         1.936D-03
  125.28        2.426D-03         1.691D-03
  125.54        2.257D-03         1.488D-03
  125.80        2.131D-03         1.324D-03
  126.06        2.048D-03         1.196D-03
  126.32        2.005D-03         1.100D-03
  126.58        1.992D-03         1.035D-03
  126.84        2.038D-03         9.991D-04
  127.10        2.118D-03         9.916D-04
  127.36        2.247D-03         1.013D-03
  127.62        2.435D-03         1.066D-03
  127.88        2.698D-03         1.157D-03
  128.13        3.067D-03         1.297D-03
  128.39        3.598D-03         1.507D-03
  128.65        4.402D-03         1.833D-03
  128.91        5.743D-03         2.353D-03
  129.17        8.405D-03         3.485D-03
  129.43        1.625D-02         6.734D-03
```

```
ANGLE =  3.0  DEGREES       ES =  160.00  GEV

    EP        XMM        QSQ         X      CBORN       CEXPEL      CEXPMU


   12.97     16.47       5.69      0.02   2.856E 03   6.645E 03   3.682E 03
   25.94     15.53      11.38      0.05   1.504E 03   2.676E 03   1.839E 03
   38.91     14.53      17.06      0.07   1.300E 03   1.878E 03   1.488E 03
   51.88     13.45      22.75      0.11   1.325E 03   1.679E 03   1.449E 03
   64.85     12.29      28.44      0.16   1.431E 03   1.649E 03   1.511E 03
   77.81     11.00      34.13      0.22   1.548E 03   1.646E 03   1.585E 03
   90.78      9.54      39.81      0.30   1.572E 03   1.547E 03   1.561E 03
  103.75      7.81      45.50      0.43   1.291E 03   1.168E 03   1.238E 03
  116.72      5.56      51.19      0.62   5.038E 02   4.121E 02   4.634E 02
```

$$\frac{d^2\sigma}{dEd\Omega} \simeq \frac{\alpha^2 \operatorname{ctn}^2(\theta/2)}{4E_o^{\,2} \sin^2(\theta/2)} \cdot \frac{(\nu W_2)}{\nu} \tag{17}$$

$$\sigma = \frac{4\pi}{3} \cdot \frac{\alpha^2}{E_o^{\,2}} \cdot \ln\left(\frac{\nu_{max}}{\nu_{min}}\right)\left(\frac{1}{\theta_{min}^{2}} - \frac{1}{\theta_{max}^{2}}\right)\left(\frac{\Delta\phi}{2\pi}\right) \tag{18}$$

The integrated cross sections are given in Table III.

Based on the above analysis, we propose an experimental program at NAL, using the electron beam as specified in Section B which is optimised to take full advantage of the available electron intensities of NAL. The experimental program is centered on the measurement of deep inelastic electron scattering cross sections with the following major goals:

1) Test of scale invariance of the structure function νW_2 for protons and neutrons.
2) Separation of the structure function W_1 for protons and neutrons.
3) Test of scale invariance in W_1 for protons and neutrons.
4) Determination of the hadronic nature of virtual massive photons in their absorption on complex nuclei and measurements of deep electron scattering cross sections on Cu and Pb targets.
5) Measurement of the total hadronic photoproduction cross sections on protons and neutrons and complex nuclei, by an independent method.
6) Testing μ-e universality in deep inelastic lepton scattering processes and search of μ-e differences.
7) Measurement of inclusive electroproduction cross sections with multi-gamma-ray final states.

TABLE III

DEEP INELASTIC ELECTRON SCATTERING RATES AT NAL

Estimates are made for a 100 GeV electron beam [± $\Delta p/p \cdot \Delta\Omega = 3\ \mu$str.%] $10^8 e^-$/pulse, 600 pulses/hour, on a 25 cm long liquid hydrogen target, using a 30" diameter NaI(Tl) - TASC spectrometer system with a 12" × 12" × 200" magnet to yield an average azimuthal acceptance of $\Delta\phi/2\pi \simeq 1/4$. θ is the electron scattering angle; $\nu = E_o - E$ [GeV] is the virtual photon energy.

θ_{min}(deg)	θ_{max}(deg)	ν_{min}	ν_{max}	E_{min}	E_{max}	σ_{accept}(nanobarn)	Events/hour
1/8	1	2	90	10	98	1720	108,500
1	2	5	90	10	95	15.4	971
2	3	10	90	10	90	2.2	140
3	4	18	90	10	82	0.56	36
4	5	26	97	3	74	0.21	13
5	6	34	97	3	66	0.09	6
6	7	42	97	3	58	0.045	3
7	8	50	97	3	50	0.022	1.5
8	9	55	97	3	45	0.013	0.8

These settings cover the Q^2 region of $Q^2 = 0.5 - 40.0\ (\text{GeV}/c)^2$, and hadronic missing mass values of $W = 3.0 - 13.5$ GeV.

8) Making a concurrent search of massive leptons in the form of excited electrons.

9) Examining possible QED breakdown in the wide angle bremsstrahlung process.

10) Performing a concurrent search of quarks electroproduced at high Q^2 values.

We propose to run with 25 cm long liquid hydrogen and deuterium targets and with 0.05 radiation lengths thick Cu and Pb targets. We estimate that 550 hours of beam time would be required for each target. Thus, our total beam request time at NAL, for Part II of our program, inclusive of data acquisition and equipment setup would be 2200 hours.

B. ELECTRON BEAM CONSIDERATIONS

Electron yield calculations and electron beam studies for a high energy proton accelerator have been made independently at HEPL. We present our electron yield estimates for a 200 GeV and 300 GeV proton beam in Fig. 7, and for a 400 GeV and 500 GeV proton beam in Fig. 8, as a function of production angles. We believe that these calculations are realistic estimates of electron beam intensities at the indicated energies and production angles because such predictions have already been tested with a 30 GeV electron beam using a 70 GeV proton accelerator.[13]

In the design of an electron beam at NAL, our principal consideration is focussed on the objective of achieving a beam with good energy and angle resolution where the electron purity is also high, while the valuable electron beam intensity is maintained at a level which is the same as the

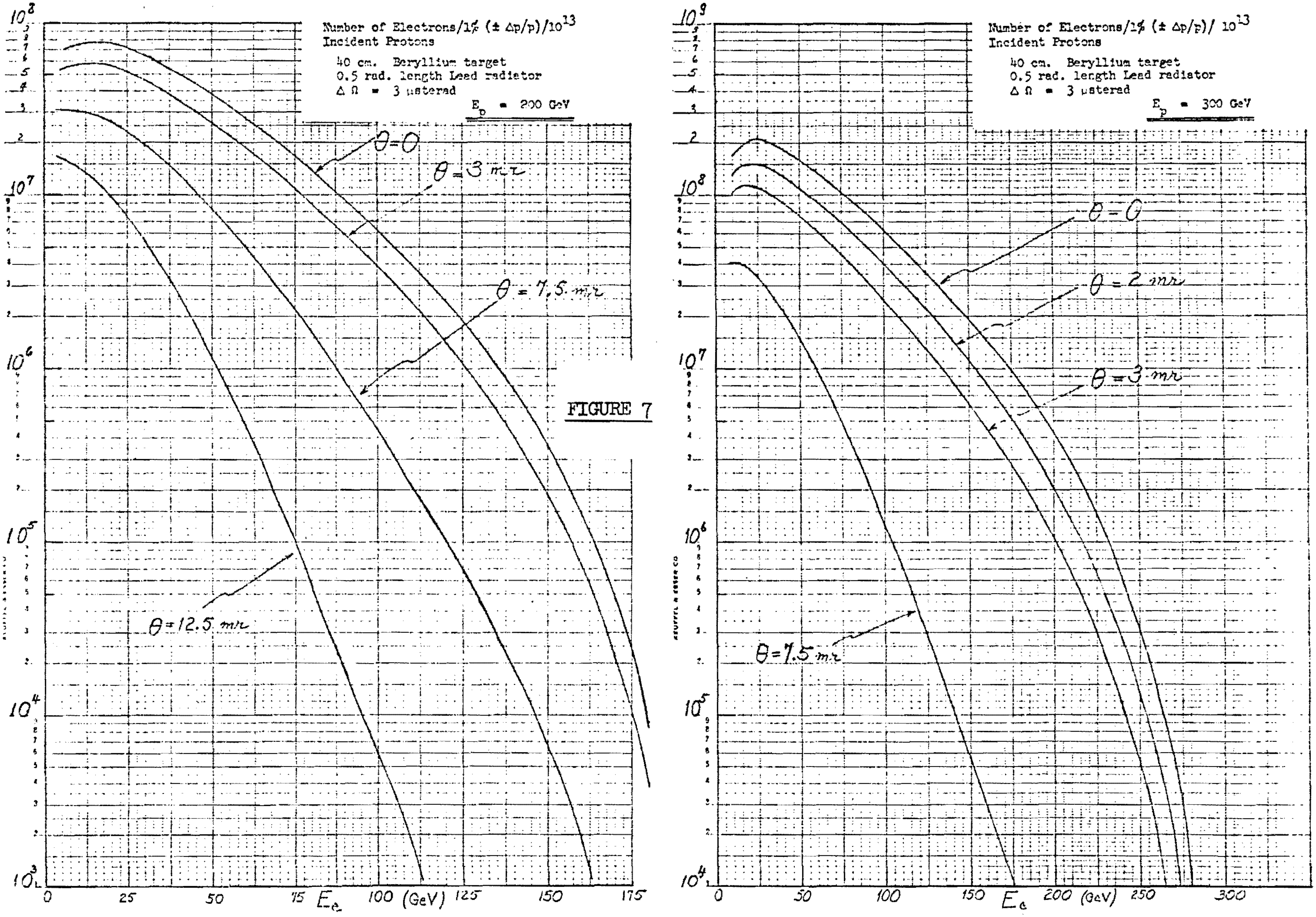

Number of Electrons/1% (± Δp/p)/10^13
Incident Protons
40 cm. Beryllium target
0.5 rad. length Lead radiator
Δ Ω = 3 μsterad
E_p = 200 GeV
θ=0
θ=3 mr
θ=7.5 mr
θ=12.5 mr
10^8
10^7
10^6
10^5
10^4
10^3
0
25
50
75
100
125
150
175
E_e (GeV)
Number of Electrons/1% (± Δp/p)/ 10^13
Incident Protons
40 cm. Beryllium target
0.5 rad. length Lead radiator
Δ Ω = 3 μsterad
E_p = 300 GeV
θ=0
θ=2 mr
θ=3 mr
θ=7.5 mr
10^9
10^8
10^7
10^6
10^5
10^4
0
50
100
150
200
250
300
E_e (GeV)

FIGURE 7

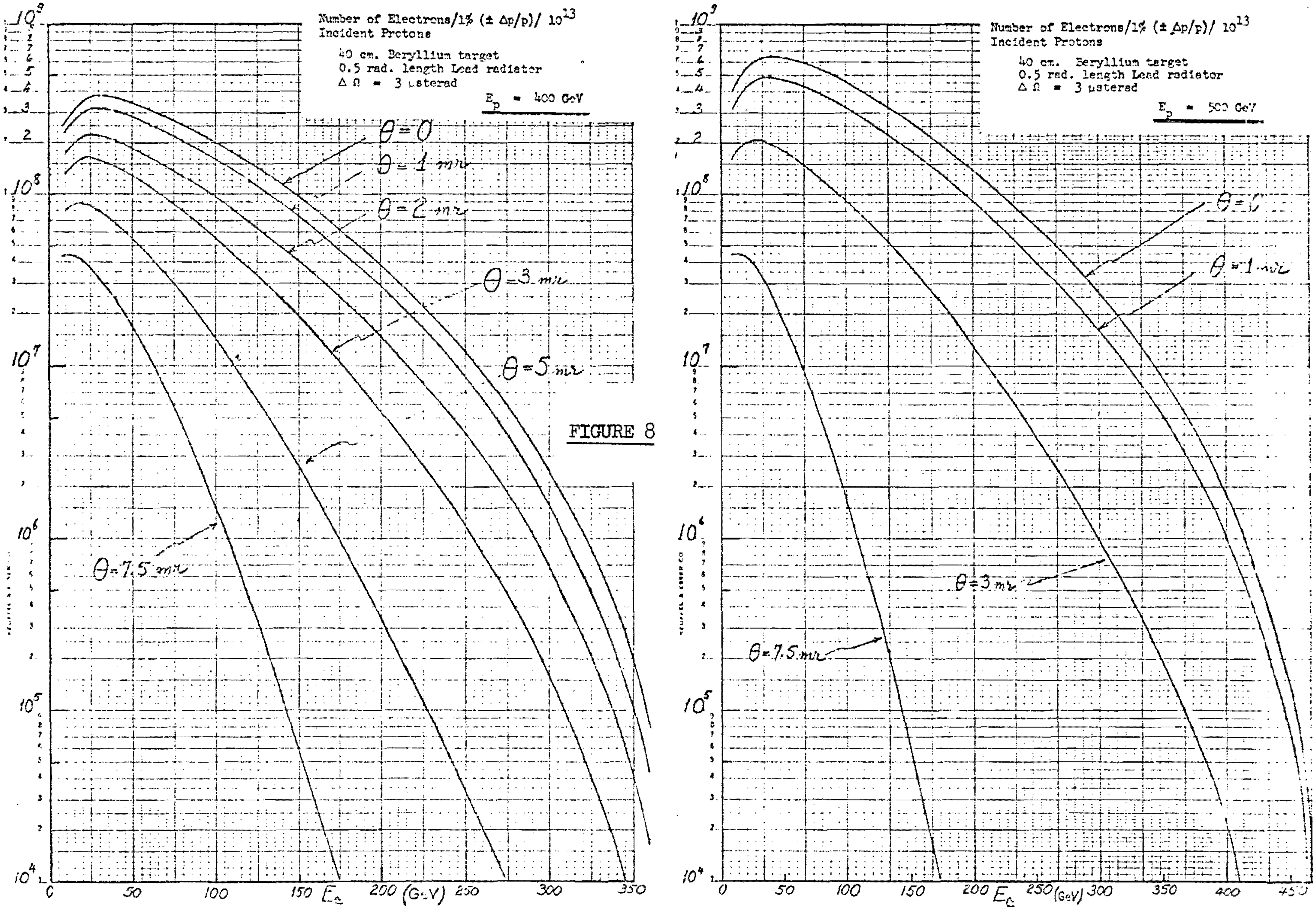
Number of Electrons/1% (± Δp/p)/ 10^13
Incident Protons
40 cm. Beryllium target
0.5 rad. length Lead radiator
Δ Ω = 3 μsterad
Ep = 400 GeV
θ = 0
θ = 1 mr
θ = 2 mr
θ = 3 mr
θ = 5 mr
θ = 7.5 mr
10^9
10^8
10^7
10^6
10^5
10^4
0
50
100
150
200
250
300
350
Ec (GeV)
Number of Electrons/1% (± Δp/p)/ 10^13
Incident Protons
40 cm. Beryllium target
0.5 rad. length Lead radiator
Δ Ω = 3 μsterad
Ep = 500 GeV
θ = 0
θ = 1 mr
θ = 3 mr
θ = 7.5 mr
10^9
10^8
10^7
10^6
10^5
10^4
0
50
100
150
200
250
300
350
400
450
Ec (GeV)

FIGURE 8

intensities produced at the production targets. At the same time, guiding practical considerations must also be met, as to economy in the cost of such a beam, flexibility in its experimental usage and simplicity in its instrumentation.

These objectives can be reached only if we have at least a four stage beam transport system. The beam optics must be chosen consistently from the beginning to be compatible with appropriate sextupole correcting elements. We wish to be helpful in NAL's endeavor in designing and constructing a good quality electron beam, and for this purpose we have made a careful analysis of a realistic set of specifications for this beam. We have arrived at these specification figures after working out a practical beam design which agrees with the above mentioned objectives. This beam design could serve as a possible example which we will discuss later in another context [cf. Appendix II].

To produce a good quality electron beam at NAL, at least four stages are required. The following functions are performed at each stage of the beam transport system. The first stage is used to define the beam's momentum and angular acceptance. A figure of $\pm \Delta p/p \cdot \Delta \Omega = (3 - 4)$ μsterad.% is specified (angular acceptance of ± 0.5 mrad. and ± 1.0 mrad., momentum acceptance of $\Delta p/p \cong 2.5\%$). At the first dispersed focus F_1, the momentum resolution should be $\lesssim 0.5\%$ so that chromatic aberrations do not cause further image size increases. The first pion clean up is made at the first vertical focus by a vertical collimator. We specify that second order aberrations should be as small as possible at the vertical collimator, for the purpose of improving the electron purity in the beam. At the second stage of the beam, momentum recombination takes place to yield an achromatic focus F_2 both horizontally and vertically.

This is where tagged photon beams are generated, essentially without any further collimation of the electron beam. For the purpose that will become necessary in the following stages, we specify that the effective beam spot size at F_2 should be $\leq \pm 0.25''$ in the bending plane and $\leq \pm 0.35''$ in the non-bending plane. This spot size is achieved by making second order corrections with sextupole elements and not by any further collimation of the beam. For our purposes, outside these spot size limits we would collimate the beam at F_2 to obtain the additional advantage of higher electron purity. In this case, our experimental requirement is a (e/π) ratio of $\gtrsim 10^4$. This requirement is derived from the cross section ratio of $\sigma_{tot}(e^-p)/\sigma_{tot}(\pi^-p)$ and the desire of keeping the electron versus pion singles rate in our spectrometer system about the same. The third stage of the electron beam produces a dispersed focus F_3. We propose to have a 12 element momentum hodoscope at F_3 where we specify a momentum resolution of $\pm \Delta p/p \leq 0.3\%$. At F_3 the minimum effective spot size, within the momentum resolution, should be $\leq \pm 0.1''$ in the bending plane and $\leq \pm 0.25''$ in the non-bending plane. The beam is focussed both horizontally and vertically at F_3. Finally, at the fourth stage of the beam transport system, again momentum recombination takes place to give an achromatic focus F_4, a horizontal and vertical spot size at the experimental target. We specify that the actual spot size of the beam, including second order aberrations, should be $< \pm 0.1''$ in the horizontal bending plane and $\leq \pm 0.5''$ in the vertical plane. Also, in the fourth stage, between F_3 and F_4, the beam optics is designed such that horizontal and vertical angle measuring hodoscopes can be placed. We propose to have a pair of 12 element hodoscopes at these locations. The three 12 element hodoscope units together with the associated fast timing electronics (gated time-to-digital converters, with a resolution of 0.5 nanosec) would be part of the electron beam transport system and would be supplied by NAL.

C. EXPERIMENTAL METHOD

The unique properties of our electron and multi-gamma-ray spectrometer system encourage us to plan a program of experimental investigations where electrons and multi-gamma-ray final states are detected with precision. Briefly, our spectrometer system is based upon the use of large segments of NaI(Tl) crystal scintillators together with multi-wire proportional chambers which are instrumented to measure both position and pulse height. Together with our magnet, which was presented in the first part of this proposal, the experimental apparatus not only measures accurately the space coordinates and energy of an accepted electron or gamma-ray, but also at the same time has the ability to certify that an electromagnetic shower of known energy was generated. Further, we expect to have in our spectrometer arms a shower pair-resolution of ~ 1" . This will make it possible either to reject events when more than one electromagnetic shower is generated by incoming electrons, positrons or gamma-rays, or to analyze the properties of a multi-gamma-ray event containing up to 4 showers.

The NaI(Tl) TASC modules together with our 12" × 12" × 200" magnet form an integral spectrometer system which is ideally suited for the measurement of deep inelastic electron scattering cross sections at NAL energies.[15]

We do not wish to repeat here a description of the experimental apparatus which is common to both parts of our proposal. The details were presented earlier and include the 12" × 12" × 200" analyzing magnet, the multi-gamma-ray and electron spectrometer modules and the data acquisition system.

Our experimental arrangement is devised to detect scattered electrons with a large geometrical acceptance and energy acceptance. The magnetic and TASC elements of our spectrometer system are adequately well matched in their acceptances. As is shown in Figs. 9 and 11, the experimental arrangement can be oriented in more than one configuration to serve the needs of several experimental physics interests.

The following unique qualities are derived from the combined use of magnetic analysis and total absorption of scattered electrons. At NAL energies, the scattered electrons have an angle of $\lesssim 10^{\circ}$, so that a magnet serves to enhance greatly the azimuthal angular acceptance of scattered electrons. Also, the magnet makes the TASC element 100% sensitive to small angle scattered electrons which have suffered a large energy loss. As is shown in Fig. 10, this is the case for our configuration I, target position A (cf. Fig. 9). In view of the moderate electron beam intensities at NAL, these are very desirable qualities in our system. At a given field and target position setting, the magnet is also used to define a momentum band of scattered electrons with a resolution of better than ± 5% in $\Delta p/p$. We show below that this momentum definition is essential for the separation of electrons from other charged hadrons which could occassionally simulate an electron's signature. We find that for the purpose of electron-hadron separation, the excellent energy resolution of our TASC modules are also very essential.

A good angular resolution of scattered electrons is obtained, $\delta\theta \approx \pm 0.3$ mrad, again by the combined functions of magnetic analysis and total absorption. In this case, the accurate energy measurement of electrons by the TASC, together with a lever arm of about 4 meters, makes it possible to trace the scattered electron's orbit inside the magnet and with this definition, yields a good measurement of the electron's scattering angle at the target.

The use of this magnet makes it possible to devise a large acceptance spectrometer system having two arms, one for the detection of electrons and the other for the coincident detection of a multi-gamma-ray final state. And lastly, this magnet serves the important function of shielding our sensitive crystals from the low energy radiation (junk), generated at the experimental target by electrons.

These are the reasons why we consider it equally important to have an electron beam transport system at NAL for which the electron beam momentum resolution and beam angular resolution are matched with those of our spectrometer system. If we could achieve a comparable resolution in the electron beam, as is the case with the scattered electrons, then good resolution in the hadronic massing mass values W is also obtained.

Similarly, the resolution in Q^2 is equally improved, so that we would be able to look for interesting structure as a function of Q^2 and W. For example, there may be steps in the behavior of the structure function νW_2, as a function of the scaling variable in the deep inelastic scattering region. These are also important considerations where a distinction between electrons and muons is sought.

Figure 9 shows our experimental arrangement in a configuration which is designed to serve concurrently three experimental functions. These are: the study of deep inelastic electron scattering, the study of electron scattering in coincidence with multi-gamma-ray final states and the detection of quarks at high Q^2 values. Our signal analysis method for the detection of quarks is discussed subsequently.

Most of the apparatus functions are designated on this figure. The beam electrons which have not interacted, are bent 14.3 mrad by the magnet and stopped at the electron beam monitoring quantameter. We propose to use a quantameter which will be constructed for NAL. This is a quantameter for 200-300 GeV electrons which will be used in an experiment (cf. NAL proposal No. 87-A) that would be scheduled to run earlier than our proposed work. The results of a Monte Carlo acceptance study with this configuration are displayed in Fig. 10. We also show a second configuration of our experimental arrangement in Fig. 11. In this case, a configuration is chosen for the experimental study of the wide angle bremsstrahlung process together with concurrent measurements of deep inelastic electron scattering cross sections at larger angles. The Monte Carlo calculation results for the acceptance of this configuration is shown in Fig. 12.

CONFIGURATION I

DESIGNED FOR THREE FUNCTIONS

1) DEEP INELASTIC ELECTRON SCATTERING
2) ELECTRON-MULTI-GAMMA-RAY COINCIDENCE
3) QUARK DETECTION

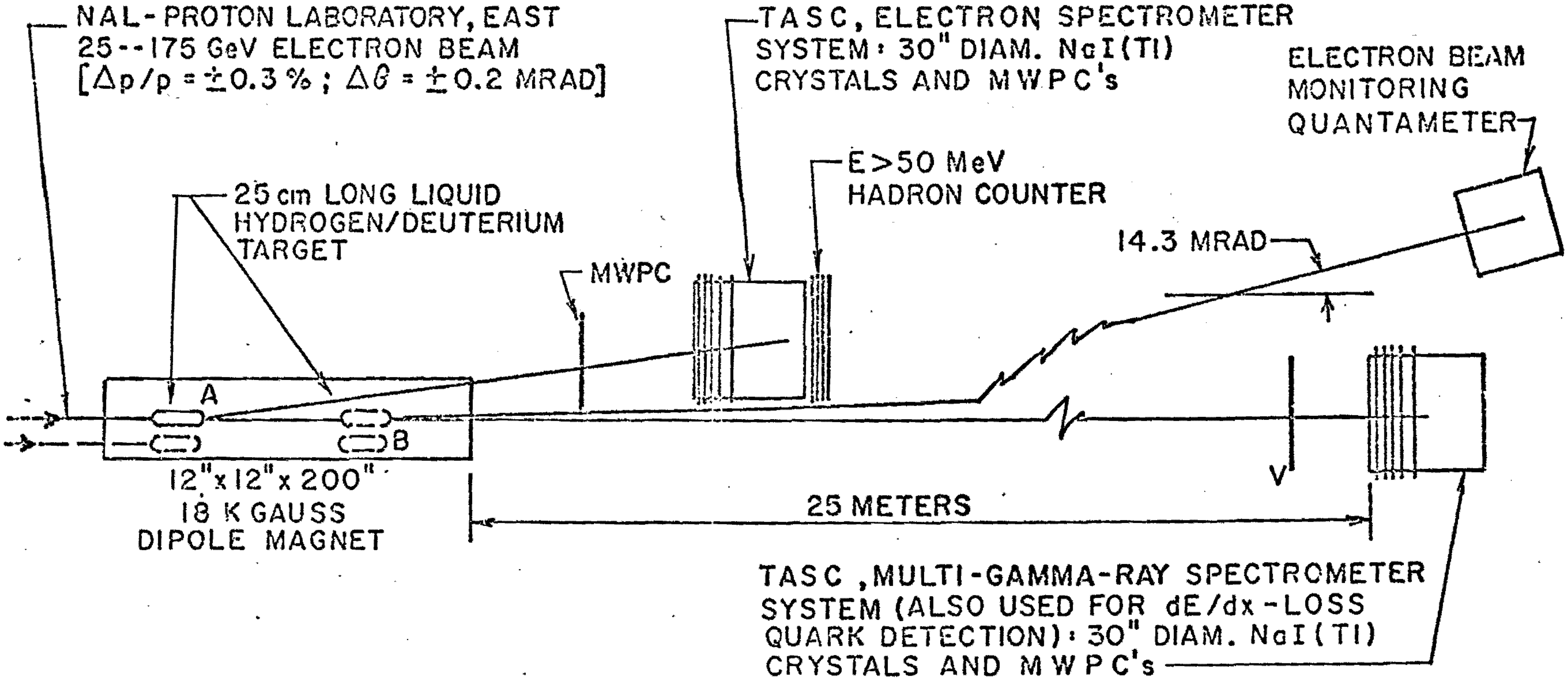

SCHEMATIC EXPERIMENTAL SETUP
(NOT TO SCALE)

FIGURE 9

electron-acceptance (B): target position

```
PHI/2PI IN PERCENT

MOMENTUM                          SCATTERING ANGLE THETA MRAD
 GEV/C  0-9.0 18.0 26.9 35.9 44.9 53.9 62.8 71.8 80.6 89.8 98.7 107.7 116.7 125.7 134.6 143.6 152.6 161.6 170.5

   1.0
  11.0   22   37   45   52   40   35   32   21   24   21   13   10   11    6    6    1    0    0    0
   1.0    0    0    0    0   18   17   26   21   26   22   20   20   21   17   14   14   11    3    0
  31.0    0    0    0    0    3   11   23   18   18   23   18   19   21   16   15   15   15    8    0
  41.0    0    0    0    0    0    7   18   16   15   18   18   17   19   16   16   15   14    9    0
  51.0    0    0    0    0    0    3    9    9   15   23   18   17   20   17   16   14   14   11    2
  61.0    0    0    0    0    0    1   10   15   16   20   19   18   20   15   15   15   14   12    4
  71.0    0    0    0    0    0    2   16   15   16   20   16   19   19   16   14   16   14   13    6
  81.0    0    0    0    0    0    0   10   14   13   20   22   19   19   16   15   14   14   11    5
  91.0    0    0    0    0    0    0    7   15   20   18   18   16   19   16   16   14   14   12    5
 101.0    0    0    0    0    0    0   11   16   15   19   19   19   19   16   15   16   15   10    6
 111.0    0    0    0    0    0    0    9   16   15   20   17   19   21   16   15   15   14   12    5
 121.0    0    0    0    0    0    0    8   11   16   15   19   18   20   16   16   15   14   12    3
 131.0    0    0    0    0    0    0    6   14   20   20   16   17   18   16   16   15   14   12    6
 141.0    0    0    0    0    0    0    7   12   20   19   16   19   17   17   16   15   15   13    6
 151.0    0    0    0    0    0    0    7   14   18   17   18   17   20   16   16   16   13   12    6

   INITIAL EVENTS=50000   FINAL EVENTS= 6022
```

electron-acceptance (A): target position

```
PHI/2PI IN PERCENT

MOMENTUM                          SCATTERING ANGLE THETA MRAD
 GEV/C   0-3.5  7.1 10.6 14.2 17.7 21.2 24.8 28.3 31.8 35.4 38.9 42.5 46.0 49.5 53.1 56.6 60.1 63.7 67.2

   1.0
  11.0     0    0    0    0    0    0    0    0    0    0    0    0    0    0    0    0    0    0    0
  21.0    40   42   17   37   18   11   11   11   10   10    5    0    0    0    0    0    0    0    0
  31.0   100  100  100   98   79   64   59   38   39   32   20    4    0    0    0    0    0    0    0
  41.0   100  100  100  100   89   77   74   66   59   45   28   11    2    1    0    0    0    0    0
  51.0   100  100  100   85   77   61   60   53   51   46   38   23    8    4    1    0    0    0    0
  61.0   100   89   77   66   66   53   46   48   45   42   39   31   18   14    6    1    0    0    0
  71.0    92   66   52   53   55   49   50   33   39   34   38   36   27   14    8    2    0    0    0
  81.0    50   54   35   38   45   47   42   41   35   41   35   36   31   18   13    6    0    0    0
  91.0     0   31   35   32   47   37   41   32   31   34   32   35   30   25   12    7    1    0    0
 101.0     0    6   36   43   30   28   35   36   31   39   34   33   30   28   18    9    3    0    0
 111.0     0    6   32   28   34   27   38   40   24   32   33   33   30   28   20    8    4    1    0
 121.0     0    0   13   29   28   37   32   33   32   34   24   33   30   28   22    9    3    2    0
 131.0     0    0    4   30   33   22   28   29   31   32   31   32   29   27   23   15    5    2    0
 141.0     0    0    5   17   29   35   33   34   36   24   21   29   30   28   23   13    7    2    0
   1.0     0    0    2   14   21   23   25   24   29   30   28   30   29   27   26   14    7    1    0

   INITIAL EVENTS=50000   FINAL EVENTS= 7984
```

FIGURE 10

CONFIGURATION I

```
0.000 4.000 3.000 0.000 0.300 0.060 0.240 1.000 1.000 0.325
151.0   1.0   0.0  18.0
0.06000 0.01500 0.06000 0.03750 0.01430 0.00000 0.07075 0.08152 0.47152
```

CONFIGURATION II

DESIGNED FOR TWO FUNCTIONS

1) DEEP INELASTIC ELECTRON SCATTERING
2) WIDE ANGLE BREMSSTRAHLUNG

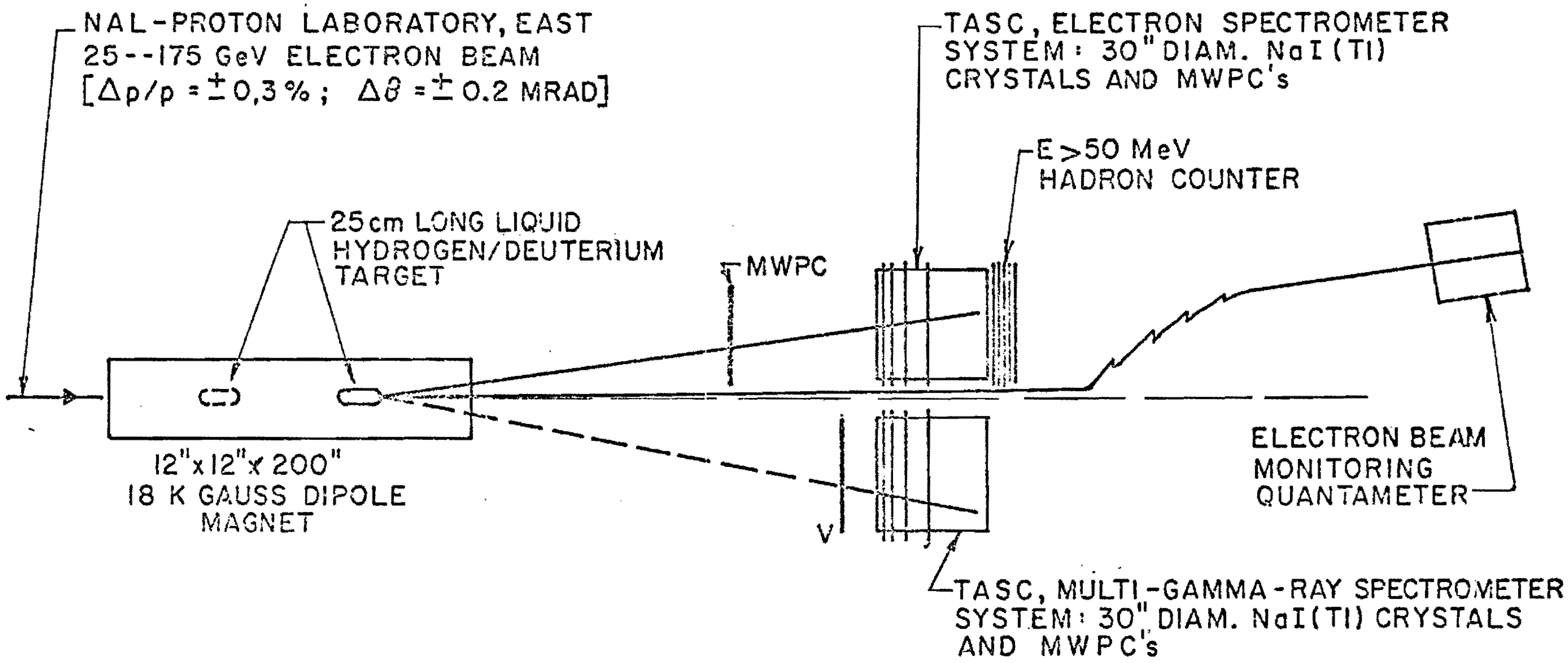

SCHEMATIC EXPERIMENTAL SETUP

(NOT TO SCALE)

FIGURE 11

θ - acceptance

```
MOMENTUM                    SCATTERING ANGLE THETA MRAD
 GEV/C   0- 5.6 11.2 16.8 22.4 28.0 33.5 39.1 44.7 50.3 55.9 61.5 67.1 72.7 78.3 83.9 89.4 95.0 100.6 106.2

   1.0 }
  11.0 }   0    3   14   26   36   33   33   31   28   23   27   27   23   22   19   17   13    7    0
  21.0 }   0    0   10   38   23   28   37   26   29   31   29   29   22   23   16   14   11    9    0
  31.0     0    0   18   30   34   27   30   33   28   30   24   27   25   20   20   17   12    8    0
  41.0     0    0   19   21   33   34   31   29   24   25   25   23   20   18   18   16   12    9    0
  51.0     0    0   21   26   25   21   35   31   18   26   30   27   20   22   16   15   12    8    0
  61.0     0    0   10   18   40   33   26   23   23   31   22   24   22   21   12   14   13    8    0
  71.0     0    0   23   23   40   33   25   31   30   27   23   22   26   21   18   15   10    7    0
  81.0     0    4   19   23   31   27   29   28   30   32   22   23   22   22   19   15   13   12    0
  91.0     0    0   25   26   27   29   31   31   28   31   27   23   22   21   20   18   15    8    0
 101.0     0    0   14   23   26   26   30   20   28   23   26   22   23   22   16   14   12   11    0
 111.0     0    0   27   22   20   36   25   27   26   26   26   24   25   20   18   16   16    9    0
 121.0     0    3   31   29   34   33   39   31   28   24   23   27   24   22   18   17   14    8    0
 131.0     0    0   20   25   27   32   24   25   26   28   27   25   25   18   20   12    9    9    0
 141.0     0    0   21   28   34   39   30   32   34   28   19   24   24   19   21   12   11    9    0
 151.0    }0    0   11   28   34   26   34   28   26   27   21   30   25   19   21   17   13    9    0

  INITIAL EVENTS=50000   FINAL EVENTS= 8487

 PHI/2PI IN PERCENT
```

electron - acceptance

```
MOMENTUM                    SCATTERING ANGLE THETA MRAD
 G    C  0- 5.6 11.2 16.8 22.4 28.0 33.5 39.1 44.7 50.3 55.9 61.5 67.1 72.7 78.3 83.9 89.4 95.0 100.6 106.2

   1.0 }
  11.0 }  75   79   71   72   61   65   58   48   33   25   14    7    6    7    2    5    1    1    0
  21.0 } 100  100   84   66   64   53   40   36   39   31   26   22   17   14    7    0    0    0    0
  31.0    87   72   42   42   50   48   36   41   33   29   34   24   17   20   12    9    0    0    0
  41.0    11   52   34   40   42   33   32   28   32   30   25   22   23   22   16   13    6    0    0
  51.0     0   37   56   29   29   31   34   27   35   29   27   24   23   19   18   10    9    0    0
  61.0     0   22   24   30   23   39   33   28   34   30   24   26   22   23   17   19    7    1    0
  71.0     0   13   25   31   29   27   38   42   29   25   30   24   22   21   20   12   11    3    0
  81.0     0   12   23   30   38   40   34   28   36   29   26   24   25   18   18   16   13    5    0
  91.0     0   12   17   32   23   29   31   33   30   27   26   23   23   24   21   16   14    4    0
 101.0     0   14   20   33   21   30   40   26   23   29   29   25   29   22   15   14   13    4    0
 111.0     0    0   11   30   26   36   34   34   32   29   27   27   27   25   18   15   12    6    0
 121.0     0    0   16   33   28   33   34   25   30   24   28   23   23   20   20   17   15    5    0
 131.0     0    0   14   17   32   35   34   31   21   23   26   23   21   21   21   16   15    7    0
 141.0     0    0   18   26   31   33   32   29   27   23   31   25   21   19   23   12   15    9    0
 151.0    }0    0   15   23   28   28   30   20   19   26   30   23   24   21   17   16   14    7    0

  INITIAL EVENTS=50000   FINAL EVENTS= 8535

0.000 1.500 5.500 0.000 0.150 0.150 0.150 1.000 1.000 0.325
151.0   1.0   0.0  10.0
0.10000 0.10000 0.10000 0.05000 0.00298 0.00000 0.11180 0.02863 0.41863
```

FIGURE 12

CONFIGURATION II

We have already made experimental tests at SLAC with the goal of understanding how to separate hadron induced signals from those induced by electrons when the momenta of these particles are the same. A single NaI(Tl) crystal assembly, 16" diameter 24" long, is exposed to an RF separated π^+ beam at 9.1 GeV. A low intensity positron beam could also be obtained by removing a lead degrader in the beam. The pulse height distribution of beam gated crystal signals is shown in Fig. 13. Using this distribution, we have derived an experimental electron versus pion separation curve as a function of the momentum measurement resolution. Figure 14 gives the separation curve. Based only on the pulse height information from a single NaI(Tl) thick crystal assembly, we conclude that, for example, a momentum measuring resolution of $\Delta p/p = \pm 5\%$ would yield a 1/2% contamination of pions in a sample of 9.1 GeV electrons.

The TASC system used in our proposal consists of six optically decoupled NaI(Tl) crystals. After calibration studies, we expect that the additional information obtained from each of the six crystal segments of our TASC module will produce an improved hadron versus electron rejection ratio. At NAL energies, we would expect that the distribution of hadron induced signals would have a peak at higher pulse heights values. However, at these energies, the electron induced signals would also have a sharper pulse height distribution. This means that the electron versus hadron separation would be independent of energy which is a favorable experimental condition.

Some time ago a quark search experiment was made at SLAC, using a single thin NaI(Tl) crystal[16] to look for the ionization energy loss response of

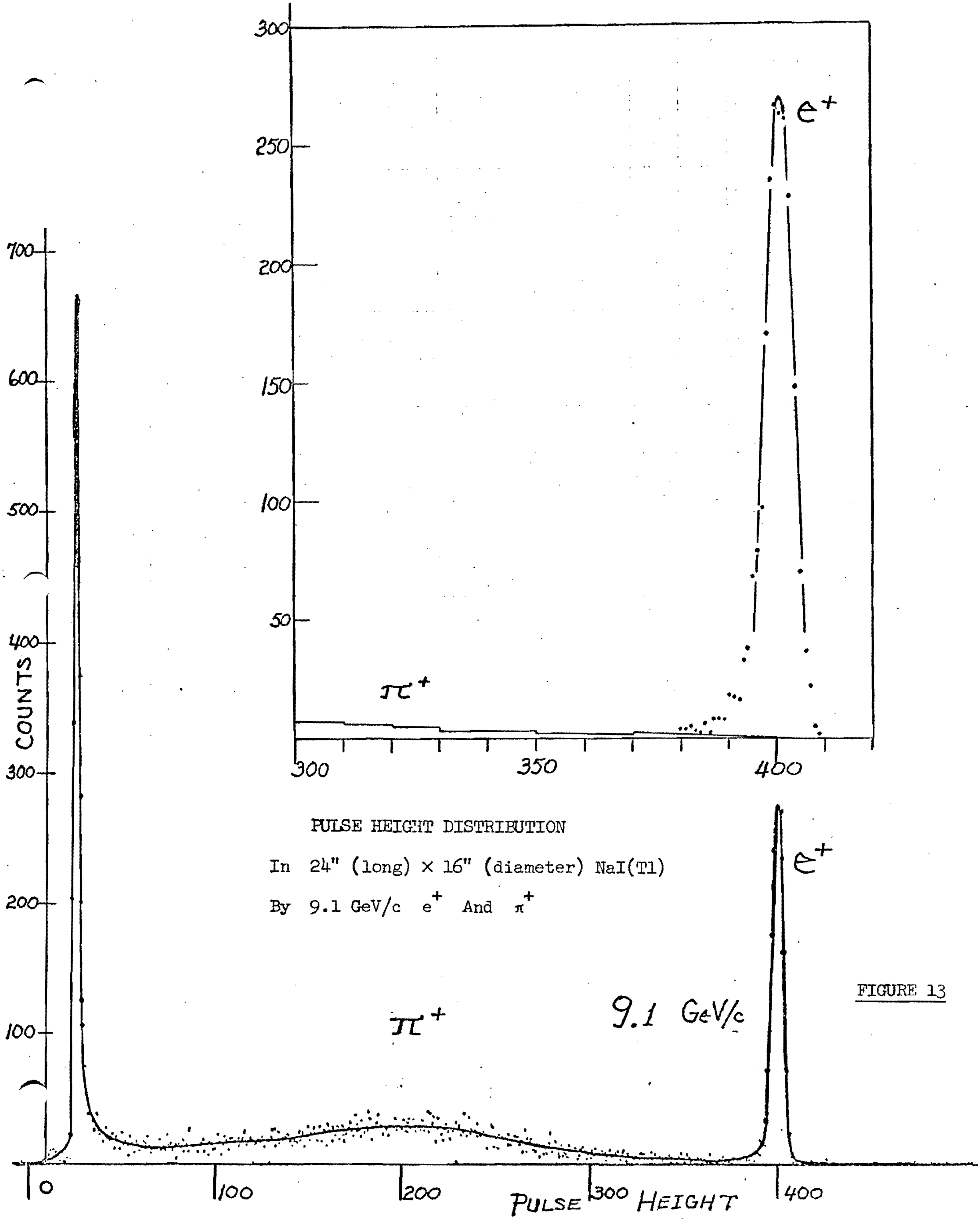

PULSE HEIGHT DISTRIBUTION

In 24" (long) × 16" (diameter) NaI(Tl)

By 9.1 GeV/c e^+ And π^+

FIGURE 13

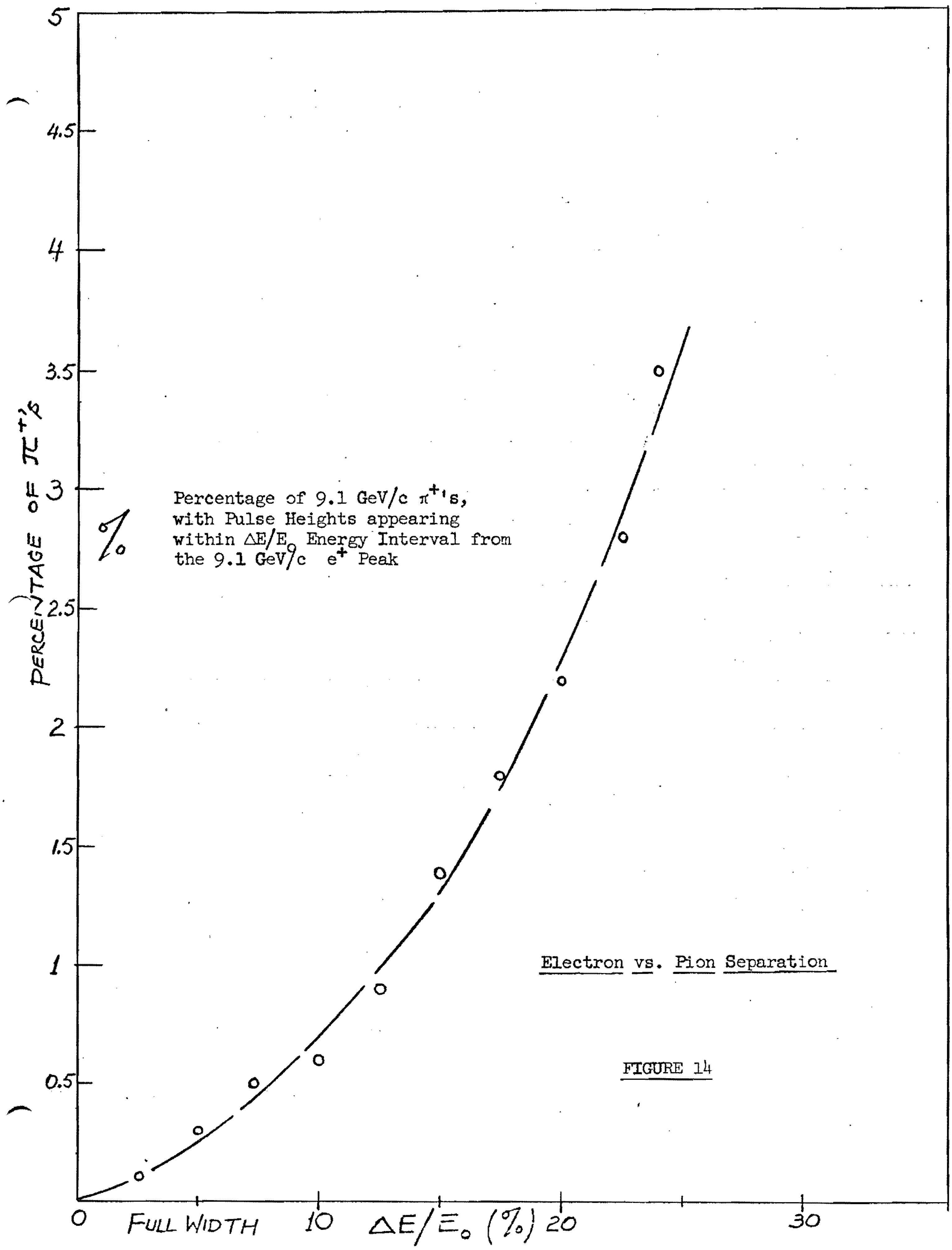

Percentage of 9.1 GeV/c π^+'s, with Pulse Heights appearing within $\Delta E/E_0$ Energy Interval from the 9.1 GeV/c e^+ Peak

<u>Electron vs. Pion Separation</u>

FIGURE 14

quarks. Also, the pulse height distribution due to energy loss and straggling of muons, in the range of 0.5 to 10.5 GeV/c was verified experimentally to follow the Landau distribution with high precision[17]. This measurement was also made with a single thin NaI(Tl) crystal. The long tail of the Landau distribution could make it difficult to distinguish a slow 2/3 e quark from a nearly minimum ionizing unit charged particle. However, an improved pulse height analysis method removes this difficulty when several scintillator elements are used and each has an independent pulse height measuring electronic system. Figure 15 shows the Landau distribution along with a calculated effective distribution, obtained by multiplying together six independent scintillator element distributions. The analysis method indicated in this figure removes entirely the tail effect and it also sharpens the peak of the effective Landau distribution. Figure 15 and 16 summarize the results of our Monte Carlo studies, with NaI(Tl) crystal scintillators, where the same geometry has been used as in our TASC spectrometer modules. In Fig. 16 the effective pulse height distributions are displayed for the assumed cases of 1/3 e and 2/3 e quarks having velocities of $\beta = 0.75$ and 0.99 . Also, for comparison we display the effective pulse height energy loss distribution for 1 GeV/c and 100 GeV/c pions. Thus, the effective quark signals would fall between 4.3 MeV and 43 MeV in energy loss deposition, for our 6 NaI(Tl) scintillators, if these fractionally charged particles lose energy only by ionization as they traverse the TASC modules.

The TASC electronic system should have a dynamic range of 10^4 to 1 to cover both the quark search and our normal measurements. This would mean an electronic sensitivity for the measurement of energy loss in the range of 4 - 40 MeV, as well as for pulse heights of electromagnetic showers in the range of 2 - 200 GeV.

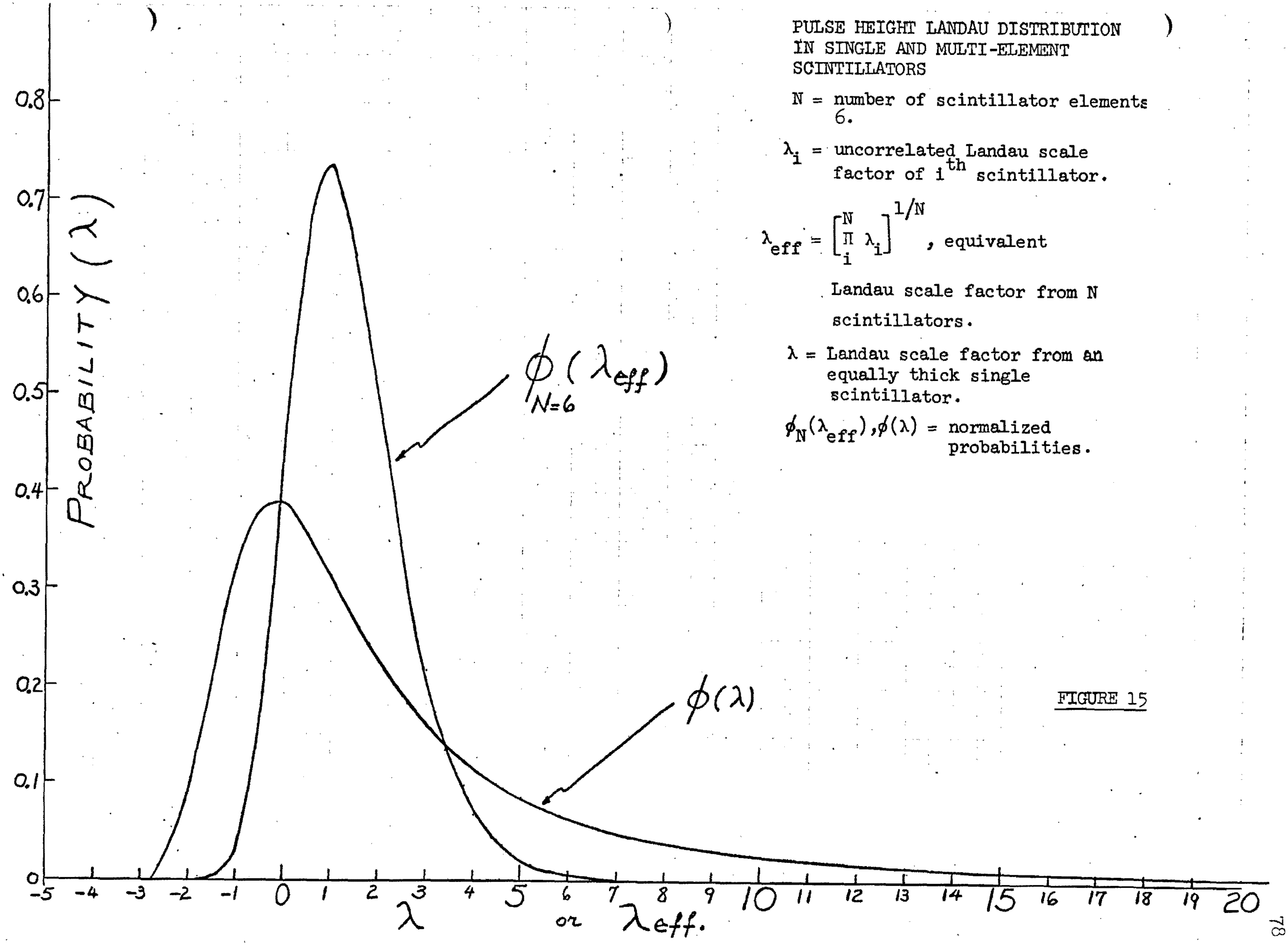

PULSE HEIGHT LANDAU DISTRIBUTION IN SINGLE AND MULTI-ELEMENT SCINTILLATORS

N = number of scintillator elements 6.

λ_i = uncorrelated Landau scale factor of i^{th} scintillator.

$\lambda_{eff} = \left[\prod_{i}^{N} \lambda_i\right]^{1/N}$, equivalent Landau scale factor from N scintillators.

λ = Landau scale factor from an equally thick single scintillator.

$\phi_N(\lambda_{eff}), \phi(\lambda)$ = normalized probabilities.

FIGURE 15

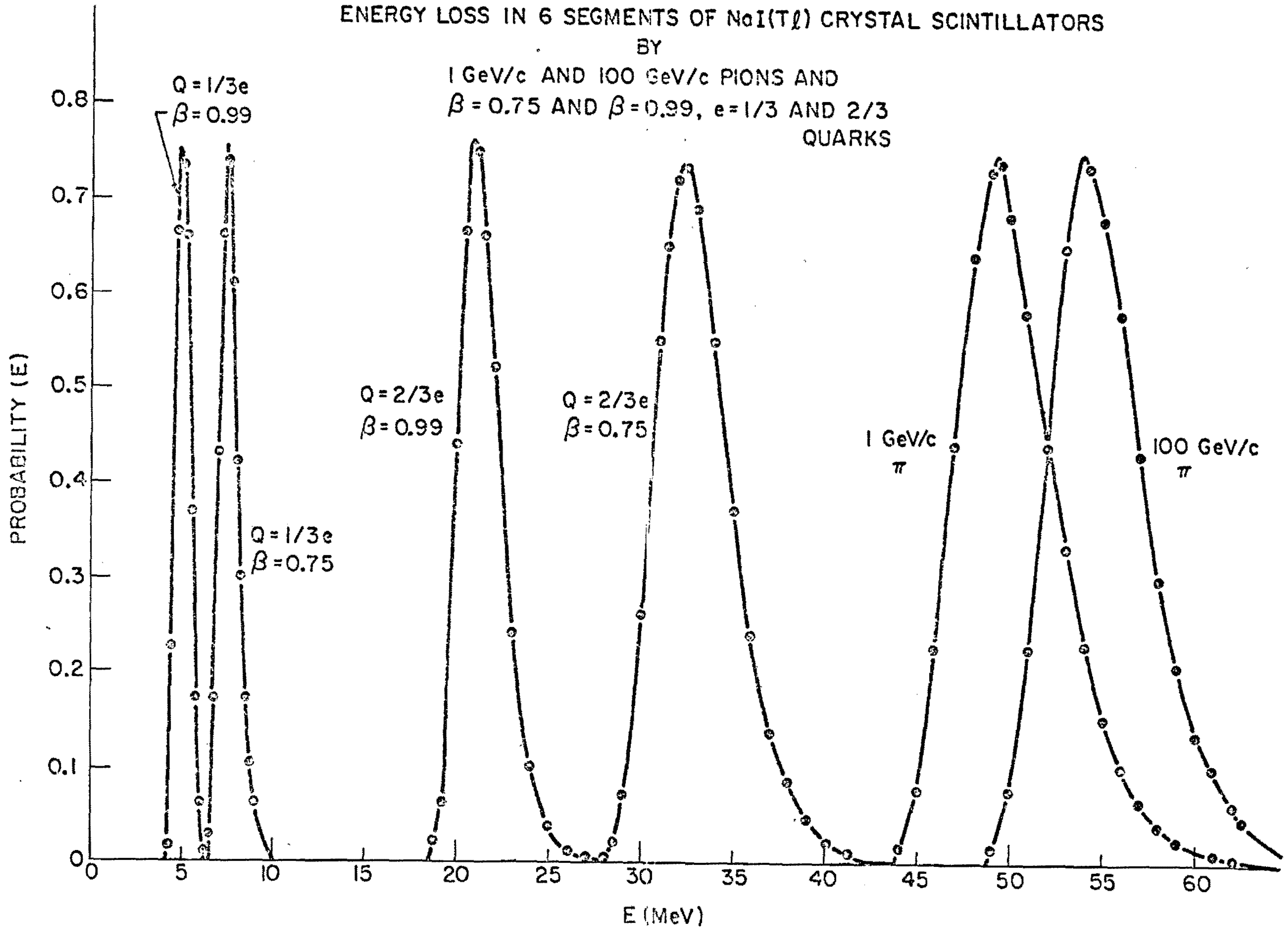

ENERGY LOSS IN 6 SEGMENTS OF NaI(Tℓ) CRYSTAL SCINTILLATORS BY 1 GeV/c AND 100 GeV/c PIONS AND β = 0.75 AND β = 0.99, e = 1/3 AND 2/3 QUARKS

FIGURE 16

The photomultiplier tubes on the TASC can be operated linearly over a range of 10^4 to 1 if the voltage divider characteristics are chosen accordingly. A convenient way of maintaining the necessary resolution in the electronics is to employ parallel amplifier systems with the photomultiplier signals gated to one system or the other on the basis of a threshold discrimination. One system would cover 1 GeV to 100 GeV for electromagnetic showers, the other system would have a factor of 100 larger gain and cover 10 MeV to 1 GeV for particles producing only ionization.

In both energy ranges it is beneficial to separately determine the energy deposited in each of the six crystals which form the TASC. In the high energy range, this information will assist in verifying that an electromagnetic shower was produced. In the low energy range, taking the product of the six individual contributions will improve the resolution of the measurement.

The necessary electronics then consist of twelve amplifiers (two per crystal) and twelve linear gates. The gain selection can be based on a threshold discriminator applied to the first 10 inch thick crystal. The presence of this discriminator signal in coincidence with a trigger event would open the gates to the six low gain amplifiers. In the absence of this signal the trigger event would open the gates to the six high gain amplifiers. In either case the amplifier outputs could be digitized by the same set of six ADC's and flags would be set in a buffer to indicate which gain was selected for that event.

REFERENCES

1. G. Miller et al, SLAC-PUB-815, J. I. Friedman et al, SLAC-PUB-907.
2. T. J. Braunstein et al, SLAC-PUB-858; W. T. Toner et al, SLAC-PUB-868.
3. M. L. Perl, SLAC-PUB-982.
4. Recent preliminary results by the MIT-SLAC collaboration are presented in the rapporteur's talk of H. W. Kendall, 1971 International Symposium on Electron and Photon Interactions at High Energies.
5. For reviews cf: Z. G. T. Guiragossián, SLAC-PUB-694; D. R. Yennie, Lecture Notes of 1970 Scottish Universities Summer School.
6. cf. Ashok suri and D. R. Yennie, SLAC-PUB-694 (and references quoted therein). Also for a different treatment based on the fragmentation concept cf. T.T. Chou and Chen Ning Yang, Hadron Momentum Distribution in Deeply Inelastic ep Collisions, SUNY preprint (1971).
7. F. E. Low, Phys. Rev. Lett. 14, 238 (1965). It should be remarked that gauge invariance would forbid the usual γ_μ charge coupling in $e^* \rightarrow e\gamma$. The existence of e^* would require a new interaction picture, for example a magnetic moment coupling. We thank A. Pais, S. B. Trieman and E. A. Paschos for an illumination discussion on the wide-angle bremsstrahlung process.
8. R. H. Siemann, W. W. Ash, K. Berkelman, D. L. Hartill, C. A. Lichtenstein and R. M. Littauer, Phys. Rev. Lett. 22, 421, (1969); see also, Phys. Rev. 1D, 825, (1970).

9. C. M.Hoffman, A. D. Liberman, E. Engels, Jr., D. C. Imrie, P. G. Innocenti, Richard Wilson, C. Zajde, W. A. Blanpied, D. G. Stairs and D. Drickey, Phys. Rev. Lett. **22**, 659, and 663, (1969).

10. M. Nauenberg, private communication and comment at the 1971 International Symposium on Electron and Photon Interactions at High Energies.

11. K. G. Wilson, rapporteur's talk at the 1971 International Symposium on Electron and Photon Interactions at High Energies.

12. For a complete formulation of radiative corrections in electron scattering cf. Yung-Su Tsai, SLAC-PUB-848; L. W. Mo and Y. S. Tsai, Rev. Mod. Phys. **41**, 205, (1969). (See also, G. Miller, SLAC Report No. 129). We are very thankful to both of our colleagues L. W. Mo and Y. S. Tsai for several illuminating discussions and for providing their computing programs on radiative corrections of deep inelastic lepton scattering.

13. A. I. Alikhanian *et al*, private communication and IHEP Report OP-CTF-70-105.

14. In this work we are very thankful to J. J. Murray for his continuing assistance and helpful insight and to K. Brown for several discussions of our problems. We are thankful to D. D. Reeder for his advice and earlier studies. In this effort, the overall coordination and capable guidance of A. L. Read is greatly appreciated and we are pleased to acknowledge S. C. C. Ting for his continuing cooperation.

15. Many technical aspects in our proposed work were elucidated further after several illuminating discussions with J. R. Sanford.

16. E. H. Bellamy, R. Hofstadter, W. L.Lakin, M. L. Perk and W. T. Toner, Phys. Rev. 166, 1391 (1968).

17. E. H. Bellamy, R. Hofstadter, W. L. Lakin, J. Cox, M. L. Perl, W. T. Toner and T. F. Zipf, Phys. Rev. 164, 417 (1967).

APPENDIX I

MULTI-GAMMA-RAY AND ELECTRON SPECTROMETER MODULES

The multi-gamma-ray and electron TASC spectrometer modules of our proposal are designed to provide the following instrumentation qualities: a high gamma-ray conversion efficiency (~ 95% for single gamma-ray), a good space resolution of ± 1.0 mm, an energy resolution which is not different than in the case of a single assembly, thick NaI(Tl) crystal, an optimized large geometric acceptance and finally the ability to measure pulse heights of showers at a given depth, with a shower pair spatial resolution of about 1".

We have devised such a TASC module which is optimized for operation in the energy range of 10 GeV - 200 GeV gamma-rays on electrons. Figure 1 displays the details of this TASC module in which the NaI(Tl) crystal thicknesses are specified and the multi-wire proportional chamber properties stated.

As a standard on the quality of total energy measurements by the NaI(Tl) TASC method, Fig. 2 shows the energy resolution obtained with 15 GeV electrons.

We have made a detailed study of shower characteristics as a function of primary energy. At HEPL an extensive library is prepared of Monte Carlo generated showers by 1 GeV gamma-rays, 8 GeV and 20 GeV electrons. Our conclusion on the geometry of NaI(Tl) crystal segmentation, shown in Fig. 1, is derived by examining shower pulse height simulations for

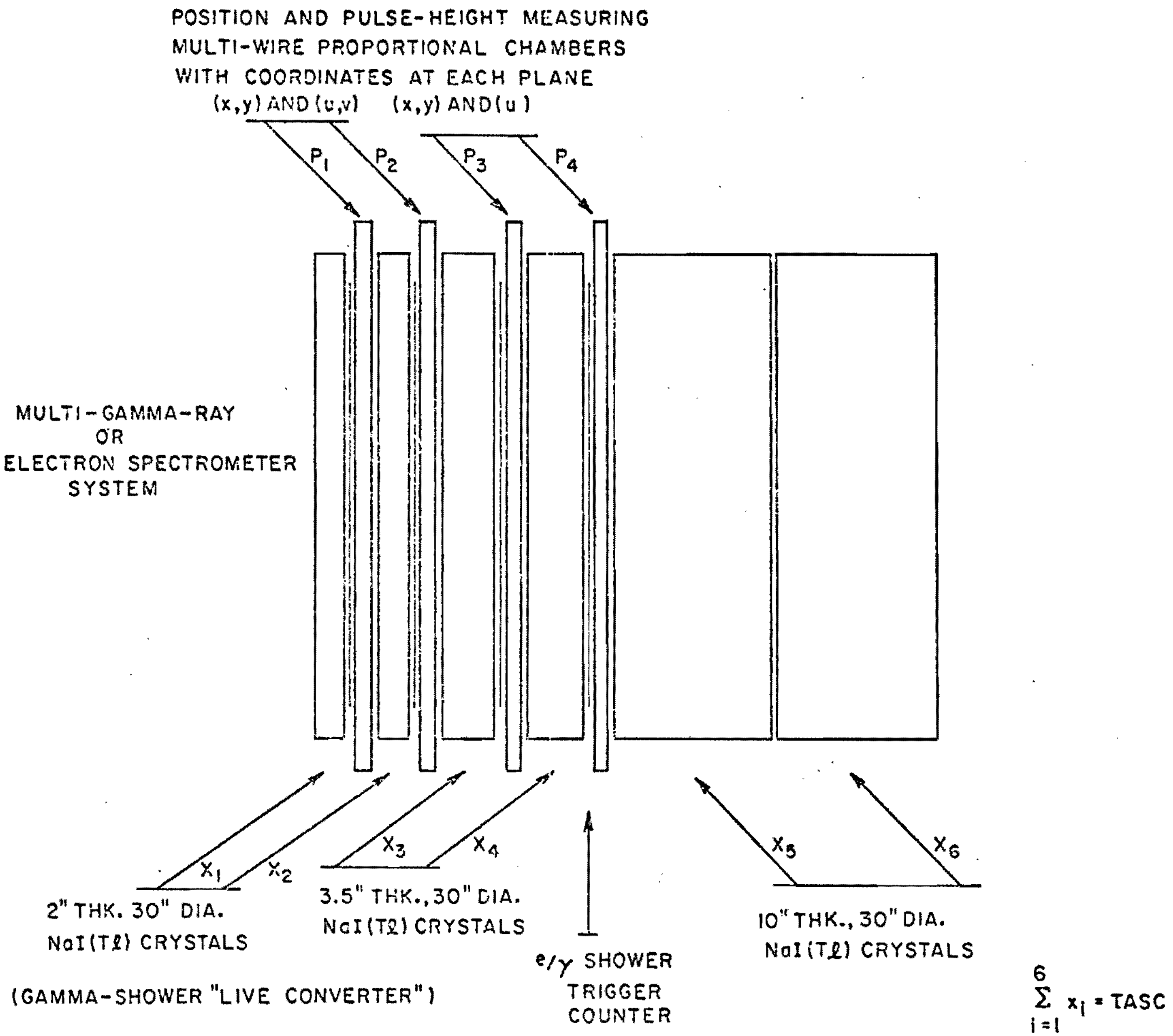
POSITION AND PULSE-HEIGHT MEASURING
MULTI-WIRE PROPORTIONAL CHAMBERS
WITH COORDINATES AT EACH PLANE
(x,y) AND (u,v)
(x,y) AND (u)
P_1
P_2
P_3
P_4
MULTI-GAMMA-RAY
OR
ELECTRON SPECTROMETER
SYSTEM
X_1
X_2
X_3
X_4
X_5
X_6
2" THK. 30" DIA.
NaI(Tℓ) CRYSTALS
3.5" THK., 30" DIA.
NaI(Tℓ) CRYSTALS
10" THK., 30" DIA.
NaI(Tℓ) CRYSTALS
(GAMMA-SHOWER "LIVE CONVERTER")
e/γ SHOWER
TRIGGER
COUNTER
$\sum_{i=1}^{6} x_i$ = TASC

FIGURE 1

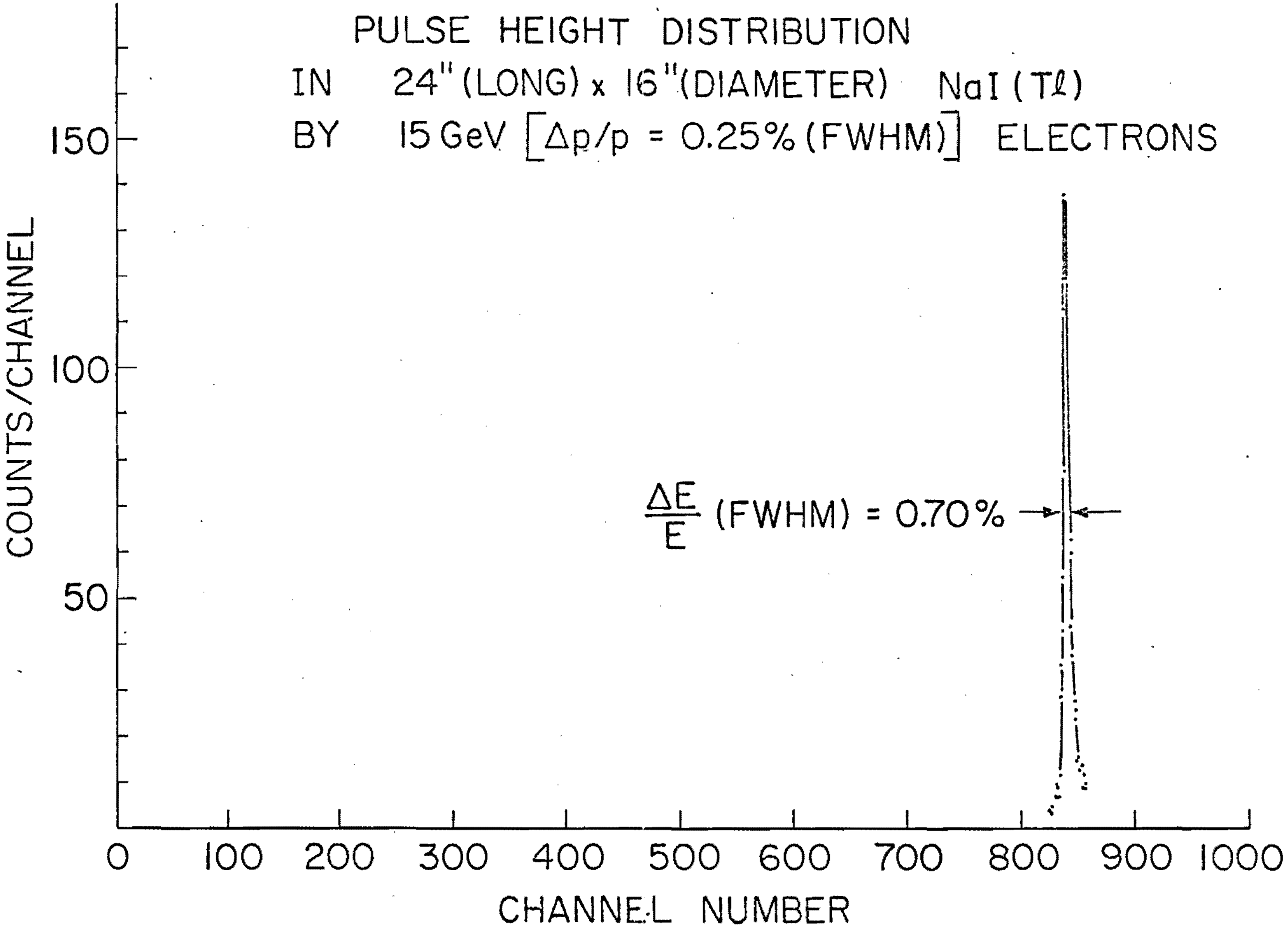
PULSE HEIGHT DISTRIBUTION
IN 24"(LONG) x 16"(DIAMETER) NaI (Tℓ)
BY 15 GeV [Δp/p = 0.25% (FWHM)] ELECTRONS
COUNTS/CHANNEL
150
100
50
ΔE/E (FWHM) = 0.70%
0
100
200
300
400
500
600
700
800
900
1000
CHANNEL NUMBER

Figure 2

several specified geometries. The Monte Carlo shower simulation library provided an excellent way of observing the effects of shower fluctuations and the statistics of fluctuations. Using this method we have observed the fluctuation in electron multiplicities as a function of shower depth positions for actually simulated experimental configurations.

The measurement of individual shower pulse heights, at a given fixed depth of absorbing material, is limited by the shower's fluctuating electron multiplicity and by the pulse height measuring apparatus inherent resolution. Above ~ 4 GeV incident energy values, the electron multiplicity's statistics is sufficiently well defined so that a Gaussian distribution of electron multiplicities is obtained. We conclude that the pulse height measuring resolution of an instrument needs to improve only as far as the shower fluctuation distribution would allow. Any further improvements in the instrument's resolution would not make the overall pulse height measuring process any better.

Figure 3 and 4 show the fluctuation characteristics of shower electron multiplicities. N^e_{max} is the maximum value of electron multiplicities in a given simulated shower in which this value is arrived at a depth of t^e_{max}. The quantities of N^e_{max} and t^e_{max} fluctuate from shower to shower, however the amount of these fluctuations decreases with increasing incident energies. In Fig. 3 the statistical distribution of these fluctuations is given for 8 GeV incident electrons and in Fig. 4, for 20 GeV electrons.

The average values of N^e_{max} and t^e_{max} agree quite well with the predictions of shower theory. These are displayed in Fig. 5 for t^e_{max} and in Fig. 6 for N^e_{max}, as a function of incident energies.

EXPECTED PERCENTAGE DEVIATION IN N^e_{max} MEASUREMENT OF INDIVIDUAL SHOWERS. SHOWER PULSE HEIGHT SAMPLINGS AT FIXED INTERVALS OF t = 2, 4, 7 and 10 rad length DEPTHS.

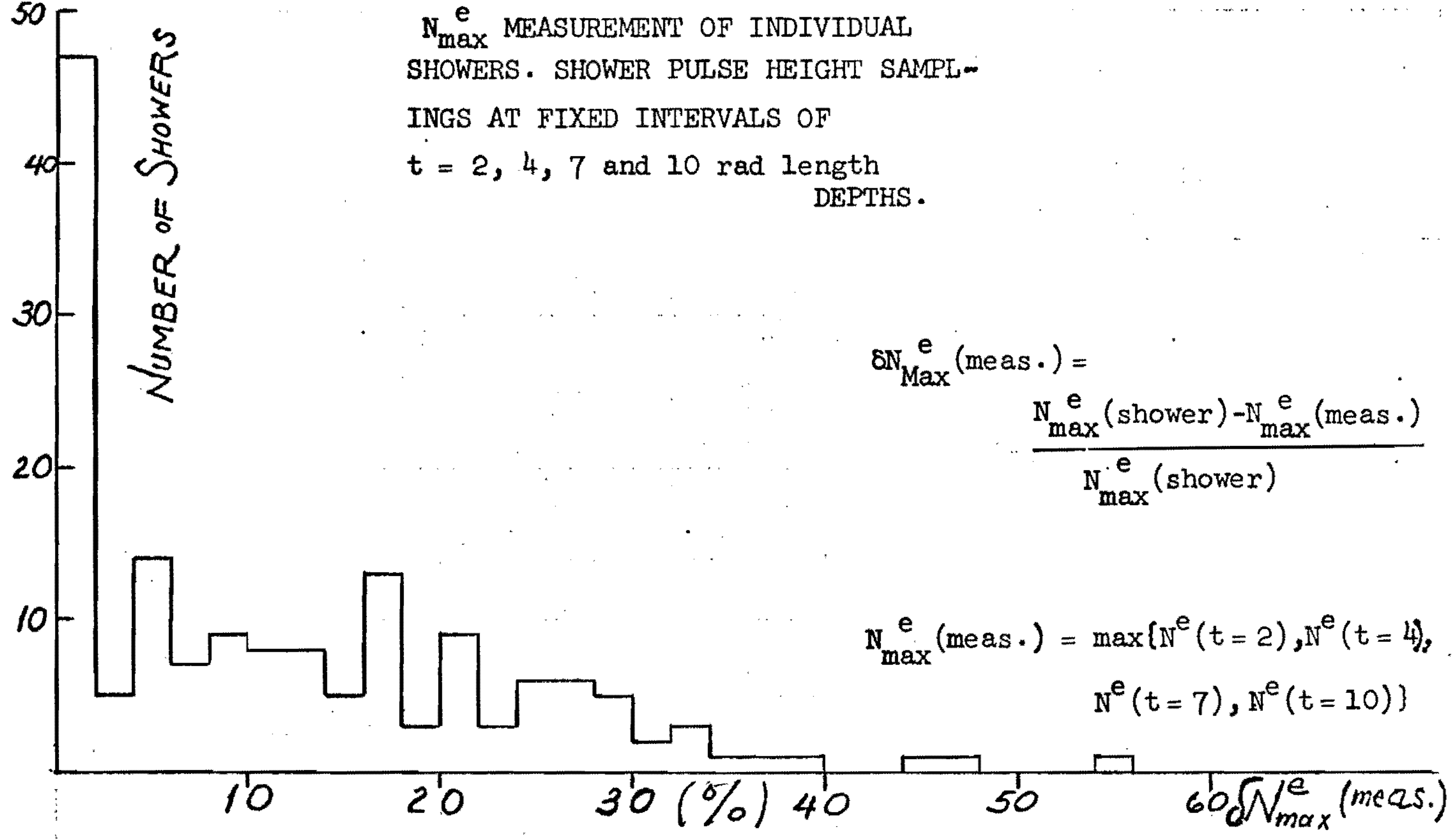

$$\delta N^e_{Max}(\text{meas.}) = \frac{N^e_{max}(\text{shower}) - N^e_{max}(\text{meas.})}{N^e_{max}(\text{shower})}$$

$$N^e_{max}(\text{meas.}) = \max\{N^e(t=2), N^e(t=4), N^e(t=7), N^e(t=10)\}$$

Figure 3

MONTE CARLO STUDY OF SHOWER FLUCTUATION CHARACTERISTICS BY 8 GeV ELECTRON SHOWERS IN LEAD.

$$\left[\frac{N^e_{max}(\text{NaI})}{N^e_{max}(\text{Pb})} = 0.587; \quad \frac{t^e_{max}(\text{NaI})}{t^e_{max}(\text{Pb})} = 0.91\right]$$

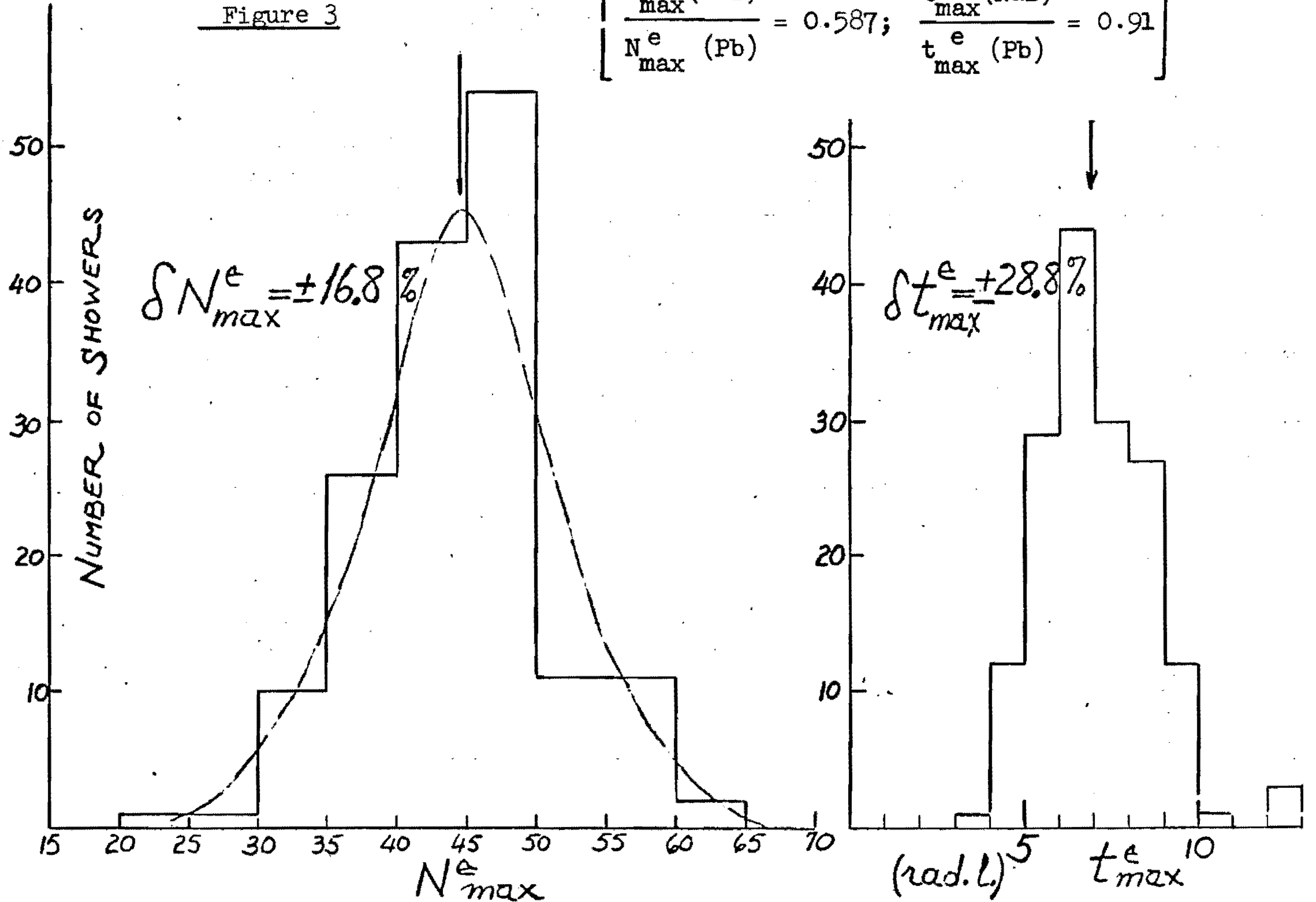

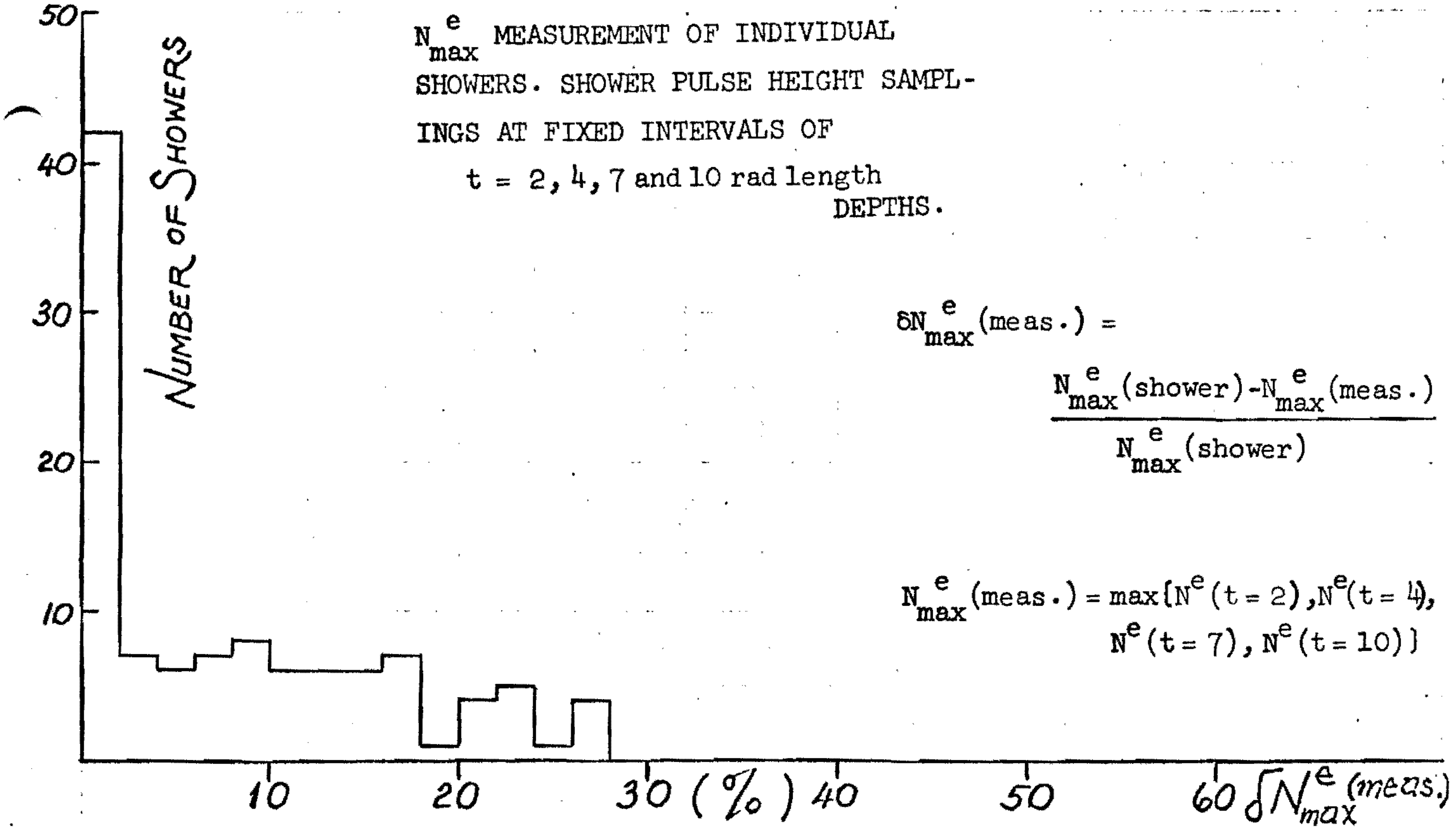
EXPECTED PERCENTAGE DEVIATION IN N^{e}_{max} MEASUREMENT OF INDIVIDUAL SHOWERS. SHOWER PULSE HEIGHT SAMPLINGS AT FIXED INTERVALS OF $t = 2, 4, 7$ and 10 rad length DEPTHS.

$$\delta N^{e}_{max}(\text{meas.}) = \frac{N^{e}_{max}(\text{shower}) - N^{e}_{max}(\text{meas.})}{N^{e}_{max}(\text{shower})}$$

$$N^{e}_{max}(\text{meas.}) = \max\{N^{e}(t=2), N^{e}(t=4), N^{e}(t=7), N^{e}(t=10)\}$$

Figure 4

MONTE CARLO STUDY OF SHOWER FLUCTUATION CHARACTERISTICS BY 20 GeV ELECTRON SHOWERS IN LEAD.

$$\left[\frac{N^{e}_{max}(\text{NaI})}{N^{e}_{max}(\text{Pb})} = 0.587; \quad \frac{t^{e}_{max}(\text{NaI})}{t^{e}_{max}(\text{Pb})} = 0.91\right]$$

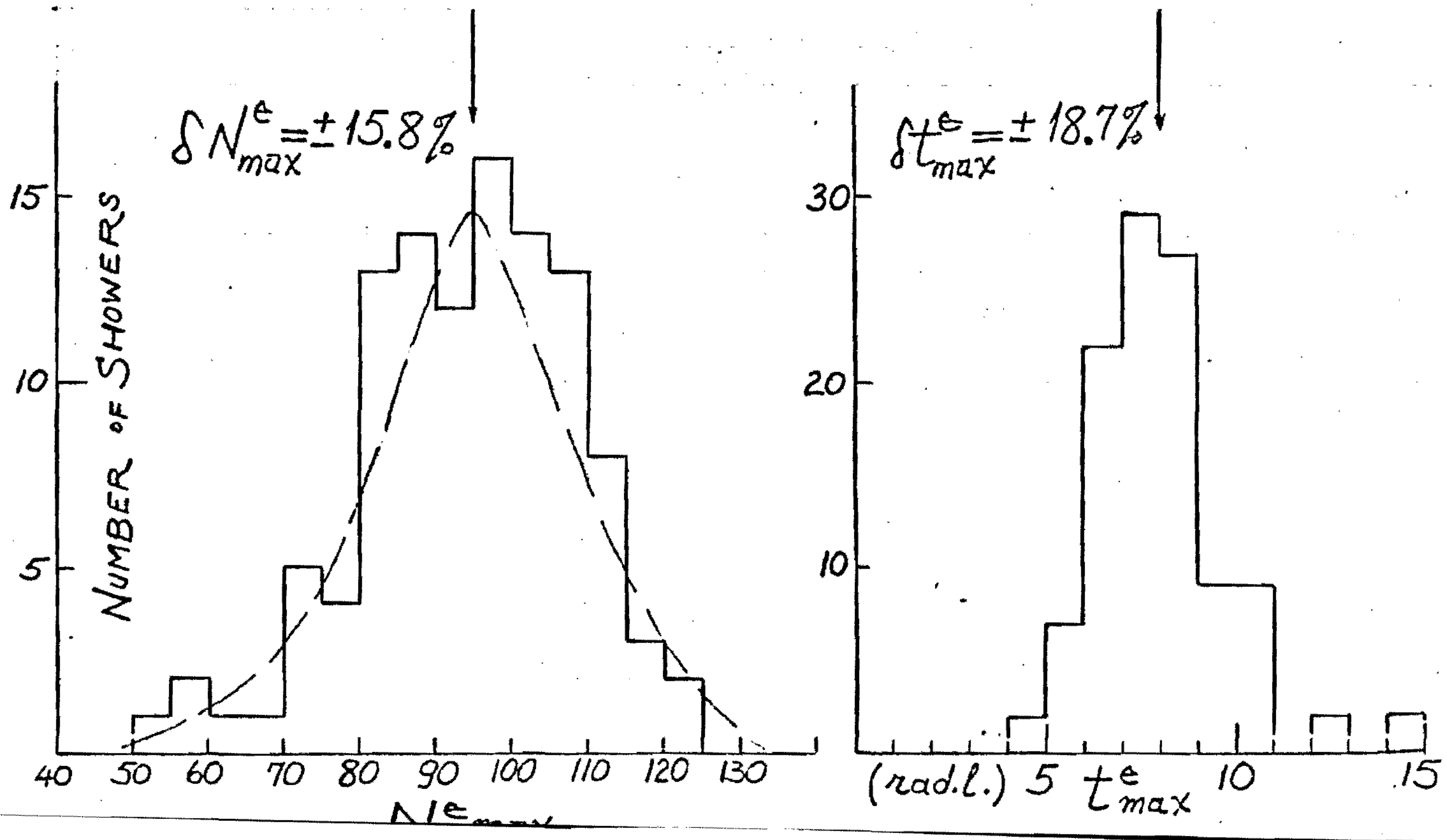

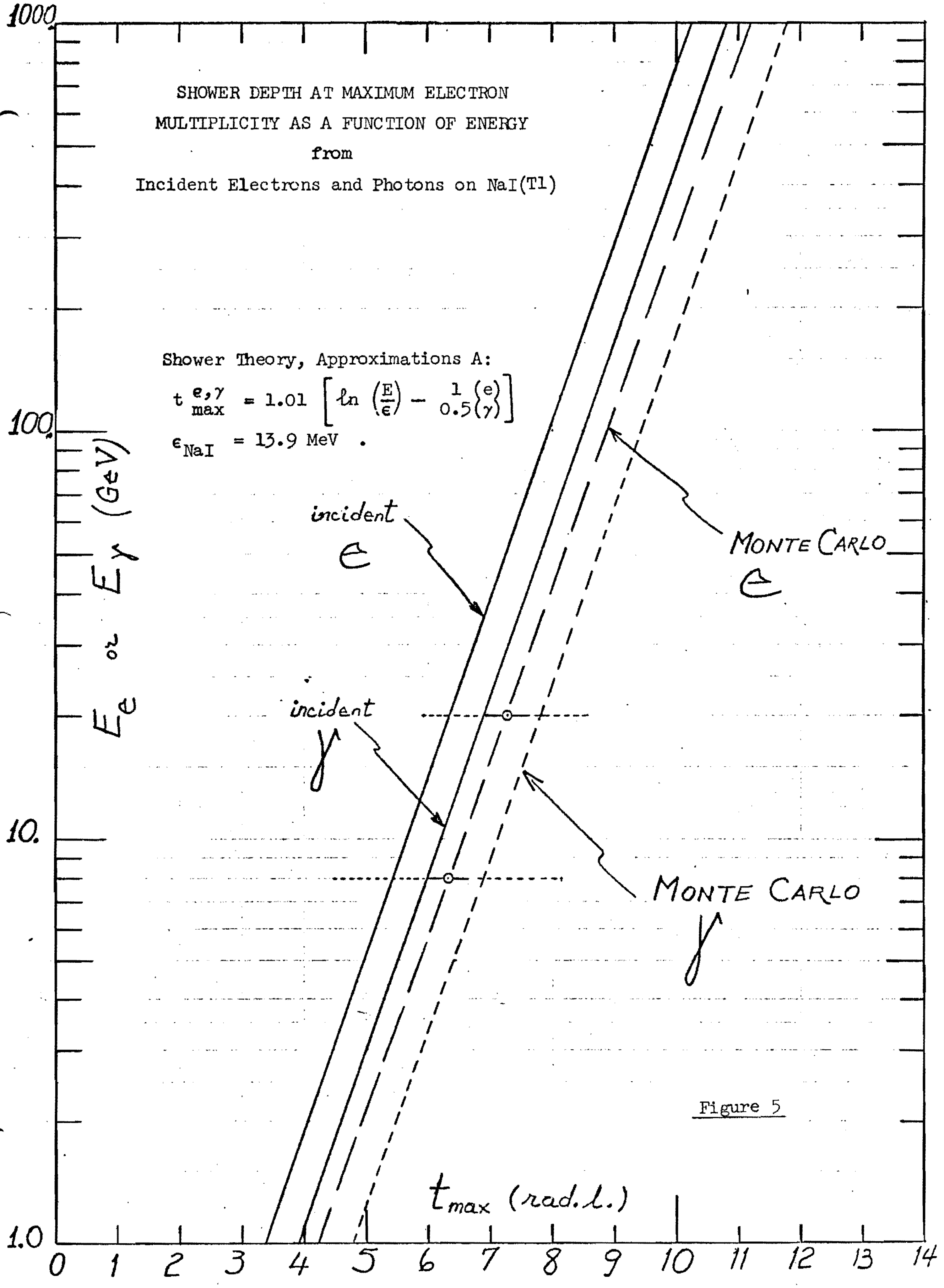

SHOWER DEPTH AT MAXIMUM ELECTRON
MULTIPLICITY AS A FUNCTION OF ENERGY
from
Incident Electrons and Photons on NaI(Tl)

Shower Theory, Approximations A:

$$t_{\max}^{e,\gamma} = 1.01 \left[\ln\left(\frac{E}{\epsilon}\right) - \begin{matrix} 1 \\ 0.5 \end{matrix} \begin{pmatrix} e \\ \gamma \end{pmatrix} \right]$$

$\epsilon_{NaI} = 13.9$ MeV .

Figure 5

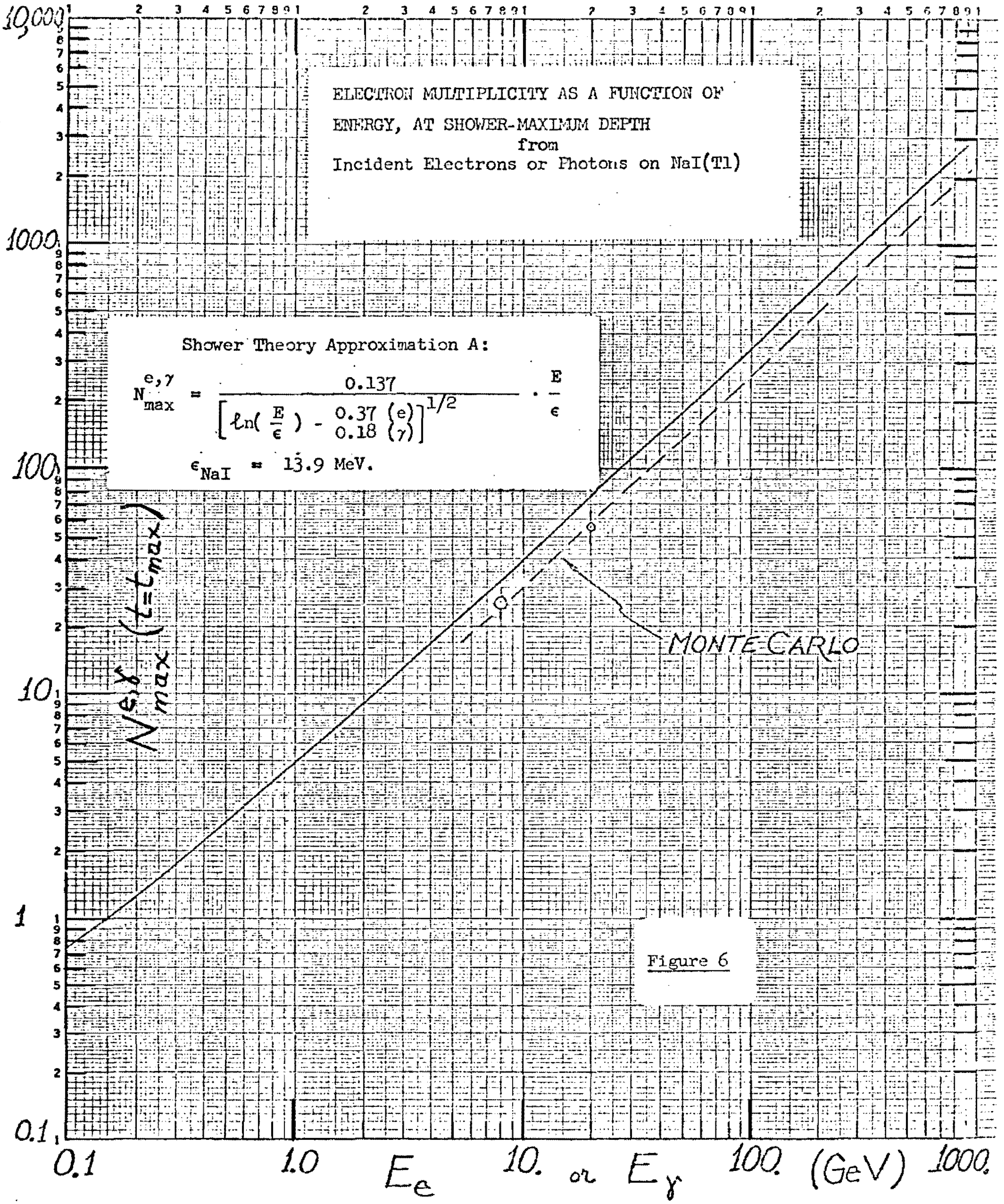

ELECTRON MULTIPLICITY AS A FUNCTION OF ENERGY, AT SHOWER-MAXIMUM DEPTH
from
Incident Electrons or Photons on NaI(Tl)

Shower Theory Approximation A:

$$N_{max}^{e,\gamma} = \frac{0.137}{\left[\ln\left(\frac{E}{\epsilon}\right) - \begin{matrix}0.37 & (e)\\ 0.18 & (\gamma)\end{matrix}\right]^{1/2}} \cdot \frac{E}{\epsilon}$$

$$\epsilon_{NaI} = 13.9 \text{ MeV.}$$

Figure 6

Finally, Fig. 7 shows the conversion efficiency of gamma-rays as a function of converter thickness. The distribution of conversion depth fluctuations is given.

Our multi-gamma-ray and electron spectrometer system's design criteria are based on statements made earlier on the characteristics of shower widths at high energies. These are substantiated in Fig. 8 which is a photograph taken with the aid of a three stage image intensifier in which scintillation light is observed, directly coming from a single 15 GeV electron induced shower. The scale is defined by the 4" x 4" x 10" NaI(Tl) crystal dimension outline. We have made similar studies using the HEPL Mark III and SLAC accelerators for 0.5 GeV and 8.0 GeV electron induced showers. Shower width broadening is clearly observed at lower energies. We conclude from these observations that with increasing energies showers do behave as well confined and narrowing cones, particularly at the depth interval between the start of showers and the region of shower maximum electron multiplicities.

Should it become necessary to remove electronic pileup effects, we would clip the NaI(Tl) scintillation signals and obtain pulses having narrower widths. There are several known techniques of clipping NaI(Tl) pulses without causing a degradation in the excellent energy resolution capability of these crystals. We remind that the energy resolution curve shown in Fig. 4 is obtained by digitizing only NaI(Tl) signal pulse heights and not the area of these pulses. Also, good timing information is derived from the fast rising leading edge behavior of these signals. The inherent rise time of NaI(Tl) scintillation light

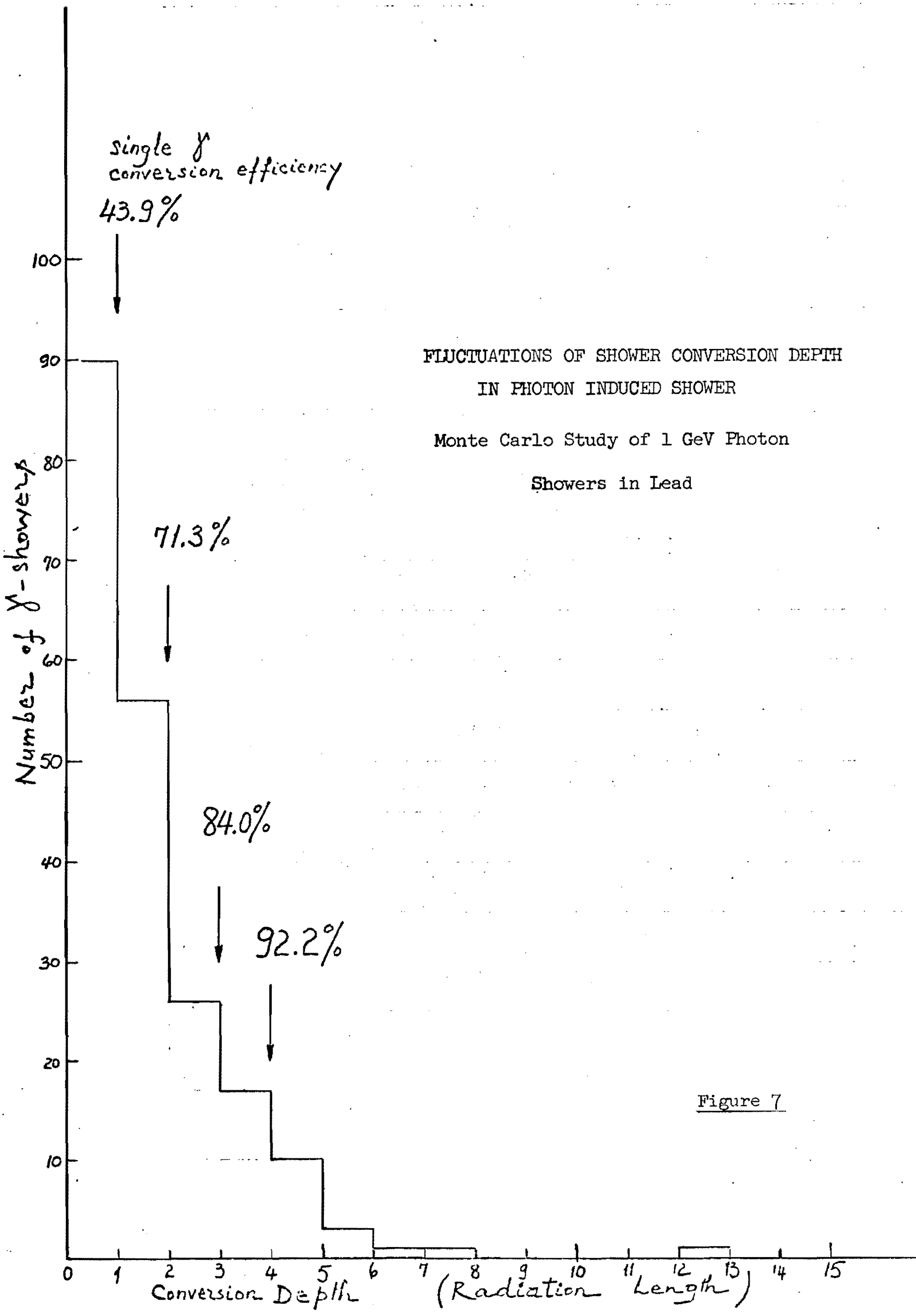

FLUCTUATIONS OF SHOWER CONVERSION DEPTH
IN PHOTON INDUCED SHOWER

Monte Carlo Study of 1 GeV Photon
Showers in Lead

Figure 7

A 15 GeV ELECTRON SHOWER IN 4" x 4" x 10" NaI(Tℓ) CRYSTAL
[SCINTILLATION LIGHT IMAGE INTENSIFIED IN THREE STAGES]

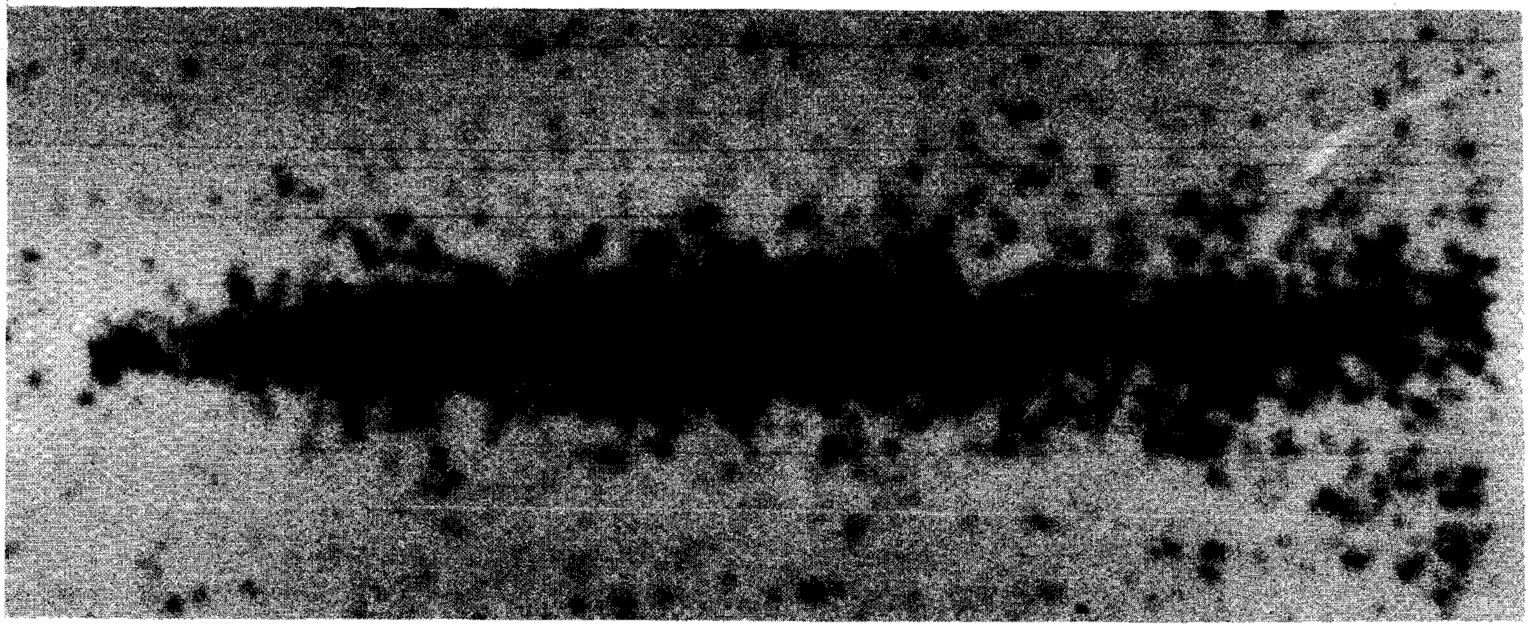

FIGURE 8

is typically ~ 3 nsec. Therefore, using fast photomultipliers, such as 56 AVP's and 58 AVP's, effectively ~ 10 nsec rise time signals are obtained where the limitation comes mainly from light transit time and multiple internal reflections in thick scintillators.

Signal clipping is accomplished by the following functions: passively splitting the mixed anode signal of the photomultipliers, delaying and attenuating the signal from one of the branches and subtracting this from the signal on the other branch. This is performed simply by the use of a coaxial stub clip which is terminated with a higher mismatched impedance. It is seen that NaI(Tl) signals could be clipped down to widths[1] of 50 nsec, yielding no perceptible degradation of energy resolution.

We conclude that the target interaction rates in both phases of our proposed experimental work and the excellent duty cycle of NAL beams are such that, there is no danger of electronics pileup, even with broad 250 nsec width clipping of NaI(Tl) signals. We expect to have good shielding around our detectors to protect these against pileup problems which could be caused by the general radiation background of the experimental area.

---

[1] C. Brassard, Nucl. Instr. Meth. 94, 301 (1971).

APPENDIX II

BEAM OPTICS DESIGN OF THE PHASE I (2 STAGE) ELECTRON BEAM, COMPATIBLE WITH A GOOD QUALITY PHASE II (4 STAGE) ELECTRON BEAM AT NAL

Electron beam considerations were discussed in Section II-B. We specified beam parameter values and described the several functions in a 4 stage beam transport system for a good quality electron beam at NAL. This appendix is presented to show a working example of the first two stages of a good quality, minimally four stage, NAL electron beam. We have developed this solution in a manner that would satisfy the experimental requirements of tagged photon proposals, (NAL No. 25, 144, 152) where a Phase I (2 stage) electron beam would be used, as well as our proposal where a good quality Phase II (4 stage) electron beam is needed.

Elsewhere, it was indicated[1] that in order to satisfy the requirements of a good quality 4 stage (Phase II) electron beam, the design of the first 2 stages (Phase I) should satisfy certain important conditions. The most essential condition is the correction of chromatic aberrations at the second focus F2 whose effect is generally larger than first order beam optical terms. A careful beam design is worked out, such that these optical corrections could be made, minimally with a pair of NAL designed sextupole elements. Moreover, we wish to stress that a beam optics design initially should be compatible with corrections by sextupoles, otherwise these elements would cause more harm than good.

---

[1] Z. G. T. Guiragossián and R. E. Rand, October 27, 1971, Memorandum to A. L. Read.

In Phase II operation, good electron beam quality conditions would be maintained only when such corrections are made at F2 without stopping down the beam at F2 or at an earlier point. In this manner the valuable electron beam intensity at NAL is saved while acceptable beam qualities are achieved with intensities of $\gtrsim 10^8$ electrons/pulse. The desirable beam qualities are summarized as follows: high electron beam purity and emittance at F2 , good momentum resolution at F3 and a smallest possible spot size at F4 . Our present design fulfills these conditions with the beam parameter values given in Table I. A momentum resolution of $\lesssim 0.5\%$ is required at F1 so that the tails of the momentum distribution, after the momentum slit, would not cause unnecessarily large charomatic aberrations in the uncorrected parts of the beam transport system. For a measure of electron beam purity, e/π improvement factors are calculated on the basis of initial spot sizes of electrons and pions. Monte Carlo calculations indicate an initial spot size of ± 0.1" for electrons, based on the expected proton beam size at the Be target and multiple scattering of electrons at the Pb radiator. Similarly, an initial spot size of ± 0.3" for pions is indicated, based on characteristic transverse momentum distribution of pions produced by interacting neutrons at the Pb radiator. Therefore, the apparent increase in emittance, due to chromatic aberrations at F2 , need be minimized in order that beam intensity would be saved in the third and fourth stages. We find that the effective use of sextupoles, together with the requirements of producing a reasonable offset in the beam line at F2 and accepting a maximum beam solid angle, constrains the nominal (FWHM) beam momentum acceptance to a value of ± 2%.

The need of beam line offset at F2 is a consequence of requiring a negligible flux of muons at F2 which arrive from the primary Be target, mainly in the forward direction.

After several trials we have become familiar with certain conditions which make successful the use of sextupole elements. (a) A pair of sextupole magnets is successfully used in a beam transport system by locating these elements at optically conjugate points with equal strengths, whereby the transfer matrix between the sextupoles is identically equal to ± unity. In this manner, even order geometrical aberrations introduced by the sextupoles cancel outside the pair locations. (b) The use of sextupole pairs in an interlaced fashion introduces serious third order aberrations. (c) As long as higher multipole magnets are not considered, for each sextupole pair, the strength is chosen to cancel only one of the second order chromatic aberrations of the beam. The above conditions imply that at least two stages are required, between fully corrected foci in a beam line, to make corrections in one of the planes and, three stages are needed to make corrections for both planes.

With the above considerations, good corrections in the first two stages of the NAL electron beam (Phase I) are made possible by a wise choice of design criteria. In the following, the standard matrix notation is used to describe first and second order beam transport optical terms. (d) Our design is based on the exact correction of the main chromatic aberration R_{126} in the horizontal bending plane x, at F2. (e) The sextupole corrections are chosen in such a way that the main geometrical aberration R_{122} which is introduced inevitably at F1, is tolerable. (f) Worsening of the chromatic aberrations in the non-bending y-plane is avoided by locating the sextupoles at foci in y where they have a negligible effect. (g) Between the true foci in y , a small spot size in y at F1 , and also at F2 , is obtained by imposing an angle focussing waist condition at these locations, $R_{33} = 0$ and $R_{44} = 0$. This arrangement also provides that chromatic aberrations in y , both at F1 and F2 , are negligible. However, there are still aberrations in terms of the vertical angle φ_o . The first focus in y designated by F1/2 , is therefore inside the first beam transport stage where chromatic aberrations are as yet small. Pions are removed from the beam by the use of a vertical slit at F1/2 .

(h) Location of the two sextupole elements at optically conjugate points requires that the beam transport structure be periodic from F1/2 to F2 . The beam acceptance defining first quadrupole doublet is separate of this structure. Therefore, the design of the first quadrupole doublet is chosen to produce a magnification in the first stage of 2.4 in the x-plane and 3.0 in the y-plane, thus increasing the acceptance of the periodic beam transport structure. This has enabled us to use a reasonable focal length for the quadrupoles, 80 ft, and it also helped to reduce the geometric aberration at F1 , introduced by the first sextupole element. (i) At the sextupole locations, the value of dispersions R_{16} are made to be equal and optimized such that the term $R_{12} \cdot \theta_o$ is just less than the term $2 \cdot R_{16} \cdot \Delta p/p$. This makes it possible that the beam acceptance is maximized while the sextupole strengths are minimized together with the geometric aberration at F1 being less than the original chromatic aberration at F2 .

However, this condition also implies that the term $R_{12} \cdot \theta_o$ is 2/3 of the available aperture, and mainly this is the compromise made for the use of sextupoles which inevitably leads to some reduction in acceptance. (j) In our arrangement also a balanced choice is made between correcting the term R_{126} at F1 and the term R_{166} at F2 . In the first case, the requirement is that the dispersion R_{16} at the first sextupole location be greater than R_{16} at the second sextupole, while in the second case, the requirement is in the opposite.

We have made calculations for magnet positions and strengths using the SLAC program TRANSPORT in first and second order beam optics. Subsequently, beam rays were traced through the final system to evaluate the design performance, using the NAL program TURTLE in all orders of beam optics. The worked out beam performance which would satisfy our electron and other photon experiment requirements is given in Table I. The beam magnet positions and strengths are listed in Table II for the case of a 300 GeV/c electron beam. The proposed Phase I electron beam would be formed using 10 NAL Beam Transfer quadrupoles 3Q120, 12 NAL Beam Transfer dipole magnets 5 - 1.5 - 120, and 2 NAL designed sextupoles 4X30.

The ray tracing program TURTLE was executed with a beam defining aperture at the first quadrupole which is horizontally, $x = \pm 0.6''$ and vertically, $y = \pm 1.2''$. The angular acceptance defined by this aperture is approximately $\theta_o = \pm 0.5$ mrad in the bending plane and $\varphi_o = \pm 1.0$ mrad in the non-bending plane.

The suggested Phase I NAL electron beam layout is displayed in Fig. 1 where the first order TRANSPORT matrix elements are also traced.

In Fig. 2 the beam envelopes, as given by second moments of distributions in TRANSPORT calculations, and the magnet apertures are shown. In the following figures some of our conclusions are clarified with the help of TURTLE generated ray tracing histograms. These are made at various foci both with and without sextupole correction elements. Figure 3 shows the expected beam profile at F1 in the bending x-plane for the idealized case of $\Delta p/p = 0\%$. The presence of sextupoles causes an asymmetry in the profile due to geometric aberrations. The expected momentum distribution at the momentum defining slit of F1 is given in Fig. 4. Again, the main effect of sextupoles at F1 is to make the momentum acceptance slightly asymmetric. Figure 5 displays the beam profile distribution at F2 in the bending x-plane. The chromatic aberration tails are evident in the case without sextupole corrections and these aberrations are fully corrected by the sextupole elements. The beam profile distribution in the non-bending y-plane at F1/2 is shown in Fig. 6(a) where the position of the pion eliminating slit is also indicated. The same profile at F2 is given in Fig. 6(b) for the case of sextupole corrected beam transport system.

In this design, the offset of the beam line at F2 , with respect to the external proton beam direction, is 19.0 ft. The beam losses in the second stage are small, typically 0.32% as given by TURTLE generated answers. These may be reduced to zero, with only a slight loss of acceptance, by stopping down further the beam aperture at the quadrupole Q7 .

TABLE I

Electron Beam Performance

Item	Electron Experiment Requirements	"Perfect" Beam	TURTLE OUTPUT (99% LIMITS)		
			Without Sextupoles	With Sextupoles	
Full Acceptance μster% $\Delta p/p$	~ 8	--	9.6	9.6	
Momentum Resltn at F1	~ 0.5%	.13%	.32%	.39%	
e/π improvement at $F\frac{1}{2}$ (y)	≥ 2.5	3.0	2.7	2.7	Assuming initial effective spot sizes for electrons ± .1" and pions ∓ .3". Collimators intercept 1% of electrons
e/π improvement at F2 (x)	≥ 2.5	3.0	2.3	3.0	
$\frac{x\theta \text{ at F2}}{x_0\,\theta_0}$	≤ 1.5	1	1.6	1.2	Calculated by adding all terms linearly to second order.
$\frac{y\phi \text{ at F2}}{y_0\,\phi_0}$	≤ 2.0	1	1.9	1.9	
Actual Spot Size at F2 ($x_2 \times y_2$)	< 1.0" × .4" (Photon expt Requirements)	.1" × .1"	.35" × .35"	.24" × .35"	
Minimum effective spot size at F3	$\leq$ .1" × .25"	.05" × .1"	.10" × .19"	.06" × .22"	Calculated from xθ at F2 assuming 1 mr acceptance at F3.
Momentum Resltn at F3	$\leq$ .3%	.07%	.13%†	.08%†	R_{16} = .75"/% assumed.
Spot Size at F_4 ($x_4 \times y_4$)	$\leq$ .1" × .5"	.1" × .1"	.20" × .38"†	-- ‡	

All quantities half width at base of distribution

† estimate

‡ not yet available

TABLE II

Magnetic Components	300 GeV/c
All Quadrupoles are	3Q 120
All Bending Magnets	5-1.5-120
Both Sextupoles	4" dia. × 2.5' long

Compt.	Field at Pole (Kg)	Position (front end)(ft.)
Aperture (± .6"× ± 1.2")	-	100
QP1,2	- 6.5640	100
QP3,4	5.4017	122
BM1,2,3,4 (Bend 0.752°)	10.792	181.5
QP5	2.4512	310
Y Slit (F 1/2) (± .36")	-	320
SXI	2.308	321
QP6	- 5.2973	390
F1	-	550
QP7	5.2973	550
BM5,6 (Bend 0.456°)	13.042	561
QP8	- 5.2973	630
BM7,8,9 (Bend 0.630°)	12.025	757
QP9	5.2973	790
SX2	2.308	801
BM10 (Bend 0.210°)	12.025	804.5
QP10	- 5.2973	870
BM11,12 (Bend 0.489°)	14.000	914.5
F2	-	1030

"TRANSPORT" MATRIX ELEMENTS

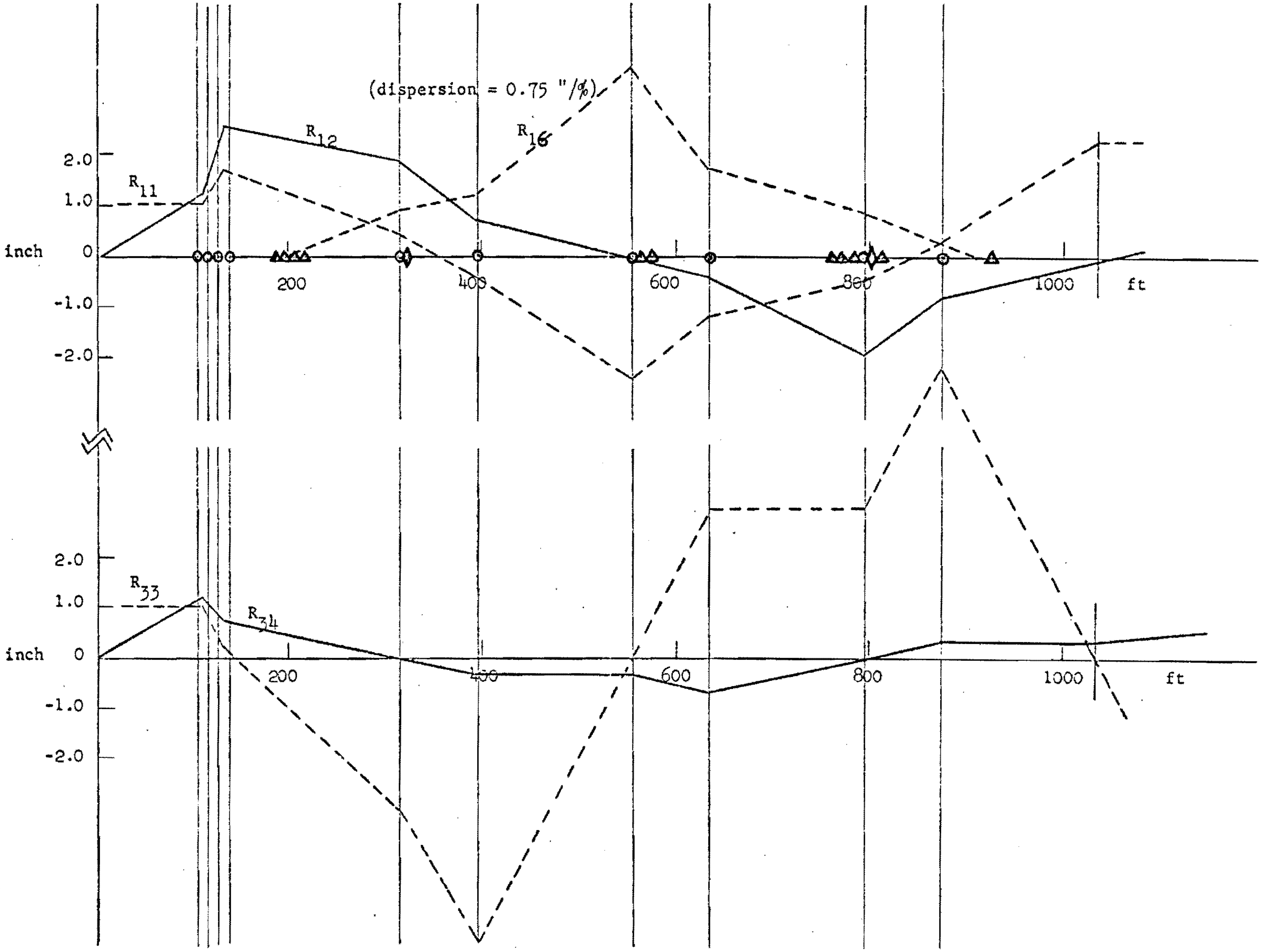

Figure 1

"TRANSPORT" BEAM ENVELOPES AND APERTURES

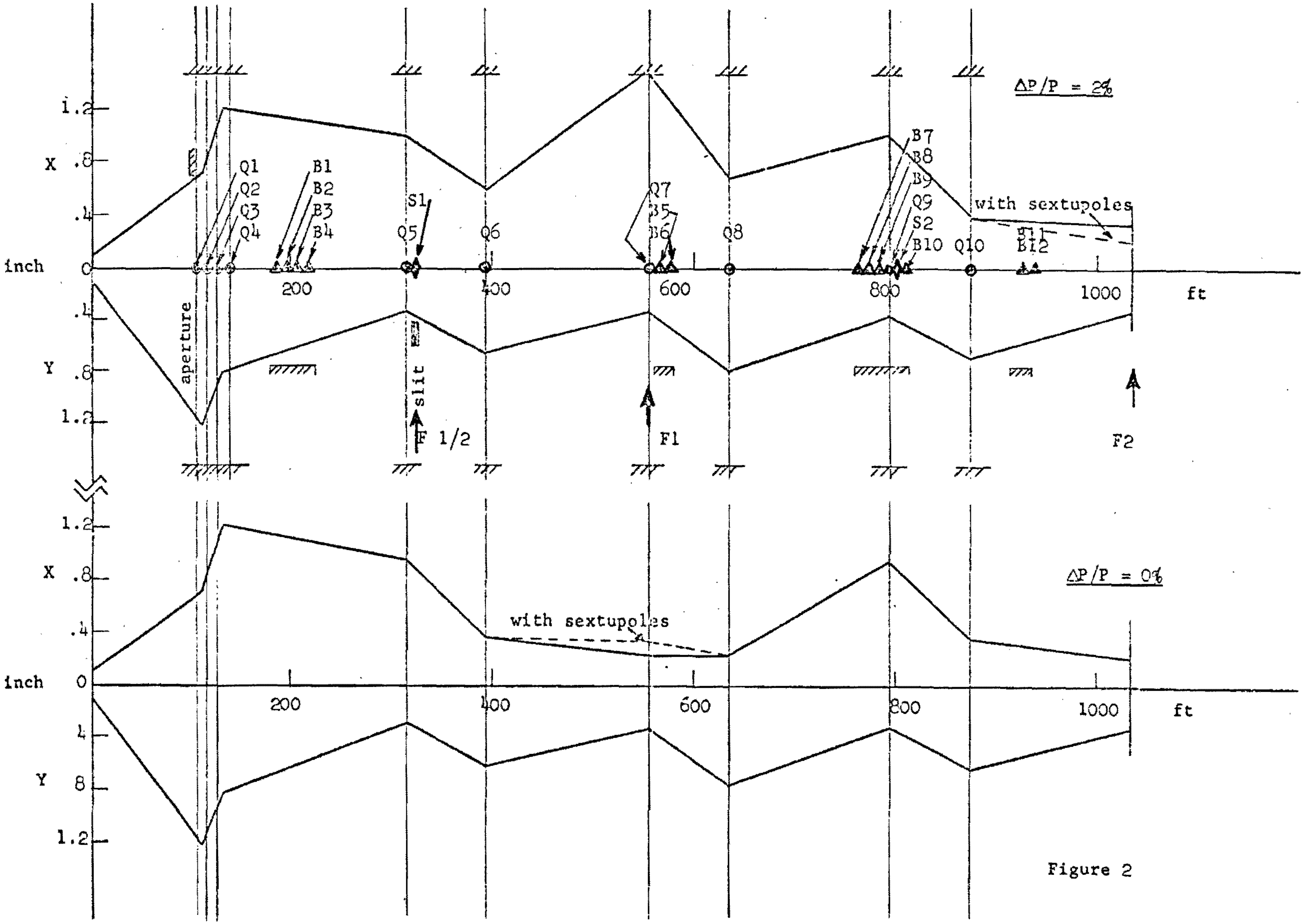

Figure 2

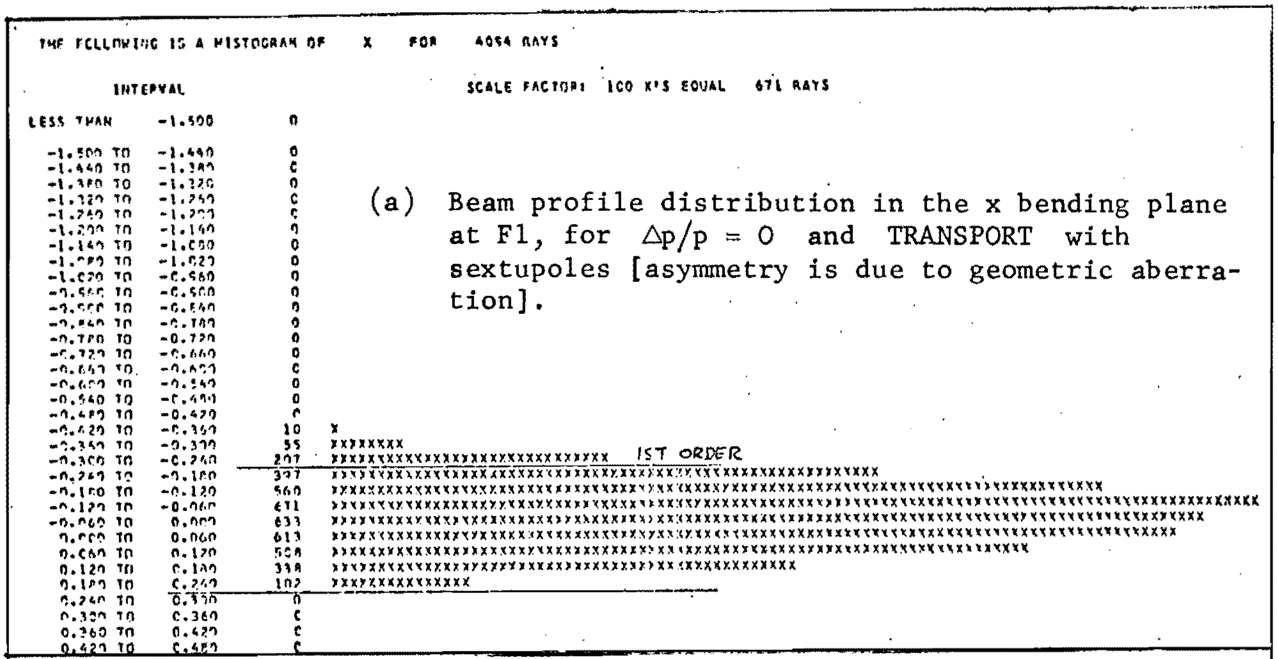

```
 THE FOLLOWING IS A HISTOGRAM OF    X    FOR    4054 RAYS

          INTERVAL                                    SCALE FACTOR: 100 X'S EQUAL   671 RAYS

LESS THAN      -1.500         0

   -1.500 TO   -1.440         0
   -1.440 TO   -1.380         0
   -1.380 TO   -1.320         0
   -1.320 TO   -1.260         0
   -1.260 TO   -1.200         0
   -1.200 TO   -1.140         0
   -1.140 TO   -1.080         0
   -1.080 TO   -1.020         0
   -1.020 TO   -0.960         0
   -0.960 TO   -0.900         0
   -0.900 TO   -0.840         0
   -0.840 TO   -0.780         0
   -0.780 TO   -0.720         0
   -0.720 TO   -0.660         0
   -0.660 TO   -0.600         0
   -0.600 TO   -0.540         0
   -0.540 TO   -0.480         0
   -0.480 TO   -0.420         0
   -0.420 TO   -0.360        10   X
   -0.360 TO   -0.300        55   XXXXXXXX
   -0.300 TO   -0.240       207   XXXXXXXXXXXXXXXXXXXXXXXXXXXXXXX
   -0.240 TO   -0.180       357   XXXXXXXXXXXXXXXXXXXXXXXXXXXXXXXXXXXXXXXXXXXXXXXXXXXXX
   -0.180 TO   -0.120       560   XXXXXXXXXXXXXXXXXXXXXXXXXXXXXXXXXXXXXXXXXXXXXXXXXXXXXXXXXXXXXXXXXXXXXXXXXXXXXXXXXXX
   -0.120 TO   -0.060       671   XXXXXXXXXXXXXXXXXXXXXXXXXXXXXXXXXXXXXXXXXXXXXXXXXXXXXXXXXXXXXXXXXXXXXXXXXXXXXXXXXXXXXXXXXXXXXXXXXXXX
   -0.060 TO    0.000       633   XXXXXXXXXXXXXXXXXXXXXXXXXXXXXXXXXXXXXXXXXXXXXXXXXXXXXXXXXXXXXXXXXXXXXXXXXXXXXXXXXXXXXXXXXXXXXX
    0.000 TO    0.060       613   XXXXXXXXXXXXXXXXXXXXXXXXXXXXXXXXXXXXXXXXXXXXXXXXXXXXXXXXXXXXXXXXXXXXXXXXXXXXXXXXXXXXXXXXXXX
    0.060 TO    0.120       508   XXXXXXXXXXXXXXXXXXXXXXXXXXXXXXXXXXXXXXXXXXXXXXXXXXXXXXXXXXXXXXXXXXXXXXXXXXXX
    0.120 TO    0.180       338   XXXXXXXXXXXXXXXXXXXXXXXXXXXXXXXXXXXXXXXXXXXXXXXXXX
    0.180 TO    0.240       102   XXXXXXXXXXXXXXX
    0.240 TO    0.300         0
    0.300 TO    0.360         0
    0.360 TO    0.420         0
    0.420 TO    0.480         0
```

(a) Beam profile distribution in the x bending plane at F1, for $\Delta p/p = 0$ and TRANSPORT with sextupoles [asymmetry is due to geometric aberration].

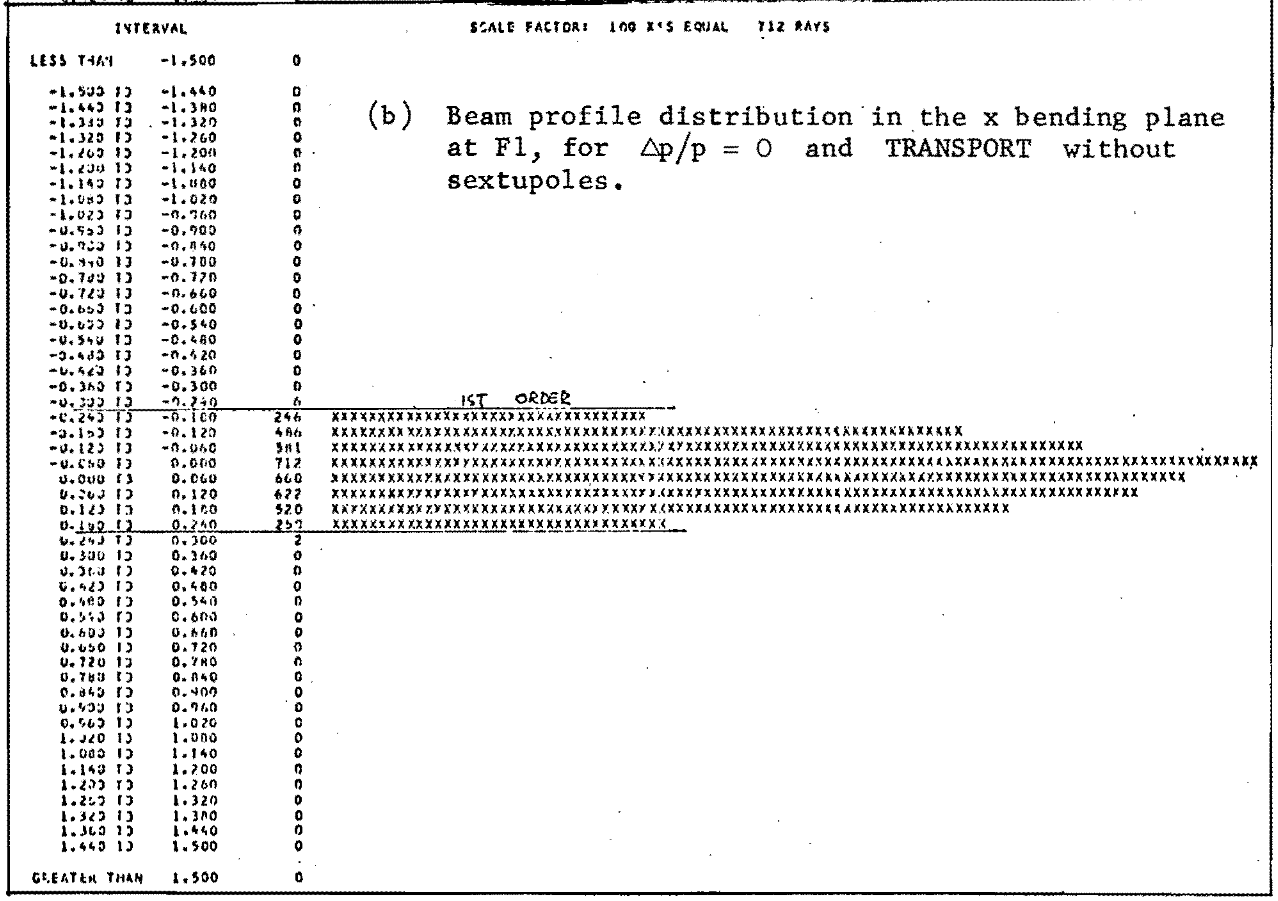

```
          INTERVAL                                    SCALE FACTOR: 100 X'S EQUAL   712 RAYS

LESS THAN      -1.500         0

   -1.500 TO   -1.440         0
   -1.440 TO   -1.380         0
   -1.380 TO   -1.320         0
   -1.320 TO   -1.260         0
   -1.260 TO   -1.200         0
   -1.200 TO   -1.140         0
   -1.140 TO   -1.080         0
   -1.080 TO   -1.020         0
   -1.020 TO   -0.960         0
   -0.960 TO   -0.900         0
   -0.900 TO   -0.840         0
   -0.840 TO   -0.780         0
   -0.780 TO   -0.720         0
   -0.720 TO   -0.660         0
   -0.660 TO   -0.600         0
   -0.600 TO   -0.540         0
   -0.540 TO   -0.480         0
   -0.480 TO   -0.420         0
   -0.420 TO   -0.360         0
   -0.360 TO   -0.300         0
   -0.300 TO   -0.240         6
   -0.240 TO   -0.180       246   XXXXXXXXXXXXXXXXXXXXXXXXXXXXXXXXXXX
   -0.180 TO   -0.120       486   XXXXXXXXXXXXXXXXXXXXXXXXXXXXXXXXXXXXXXXXXXXXXXXXXXXXXXXXXXXXXXXXXXXX
   -0.120 TO   -0.060       581   XXXXXXXXXXXXXXXXXXXXXXXXXXXXXXXXXXXXXXXXXXXXXXXXXXXXXXXXXXXXXXXXXXXXXXXXXXXXXXXXXX
   -0.060 TO    0.000       712   XXXXXXXXXXXXXXXXXXXXXXXXXXXXXXXXXXXXXXXXXXXXXXXXXXXXXXXXXXXXXXXXXXXXXXXXXXXXXXXXXXXXXXXXXXXXXXXXXXXX
    0.000 TO    0.060       660   XXXXXXXXXXXXXXXXXXXXXXXXXXXXXXXXXXXXXXXXXXXXXXXXXXXXXXXXXXXXXXXXXXXXXXXXXXXXXXXXXXXXXXXXXXXXX
    0.060 TO    0.120       622   XXXXXXXXXXXXXXXXXXXXXXXXXXXXXXXXXXXXXXXXXXXXXXXXXXXXXXXXXXXXXXXXXXXXXXXXXXXXXXXXXXXXXXX
    0.120 TO    0.180       520   XXXXXXXXXXXXXXXXXXXXXXXXXXXXXXXXXXXXXXXXXXXXXXXXXXXXXXXXXXXXXXXXXXXXXXXXX
    0.180 TO    0.240       257   XXXXXXXXXXXXXXXXXXXXXXXXXXXXXXXXXXXX
    0.240 TO    0.300         2
    0.300 TO    0.360         0
    0.360 TO    0.420         0
    0.420 TO    0.480         0
    0.480 TO    0.540         0
    0.540 TO    0.600         0
    0.600 TO    0.660         0
    0.660 TO    0.720         0
    0.720 TO    0.780         0
    0.780 TO    0.840         0
    0.840 TO    0.900         0
    0.900 TO    0.960         0
    0.960 TO    1.020         0
    1.020 TO    1.080         0
    1.080 TO    1.140         0
    1.140 TO    1.200         0
    1.200 TO    1.260         0
    1.260 TO    1.320         0
    1.320 TO    1.380         0
    1.380 TO    1.440         0
    1.440 TO    1.500         0

GREATER THAN    1.500         0
```

(b) Beam profile distribution in the x bending plane at F1, for $\Delta p/p = 0$ and TRANSPORT without sextupoles.

FIGURE 3

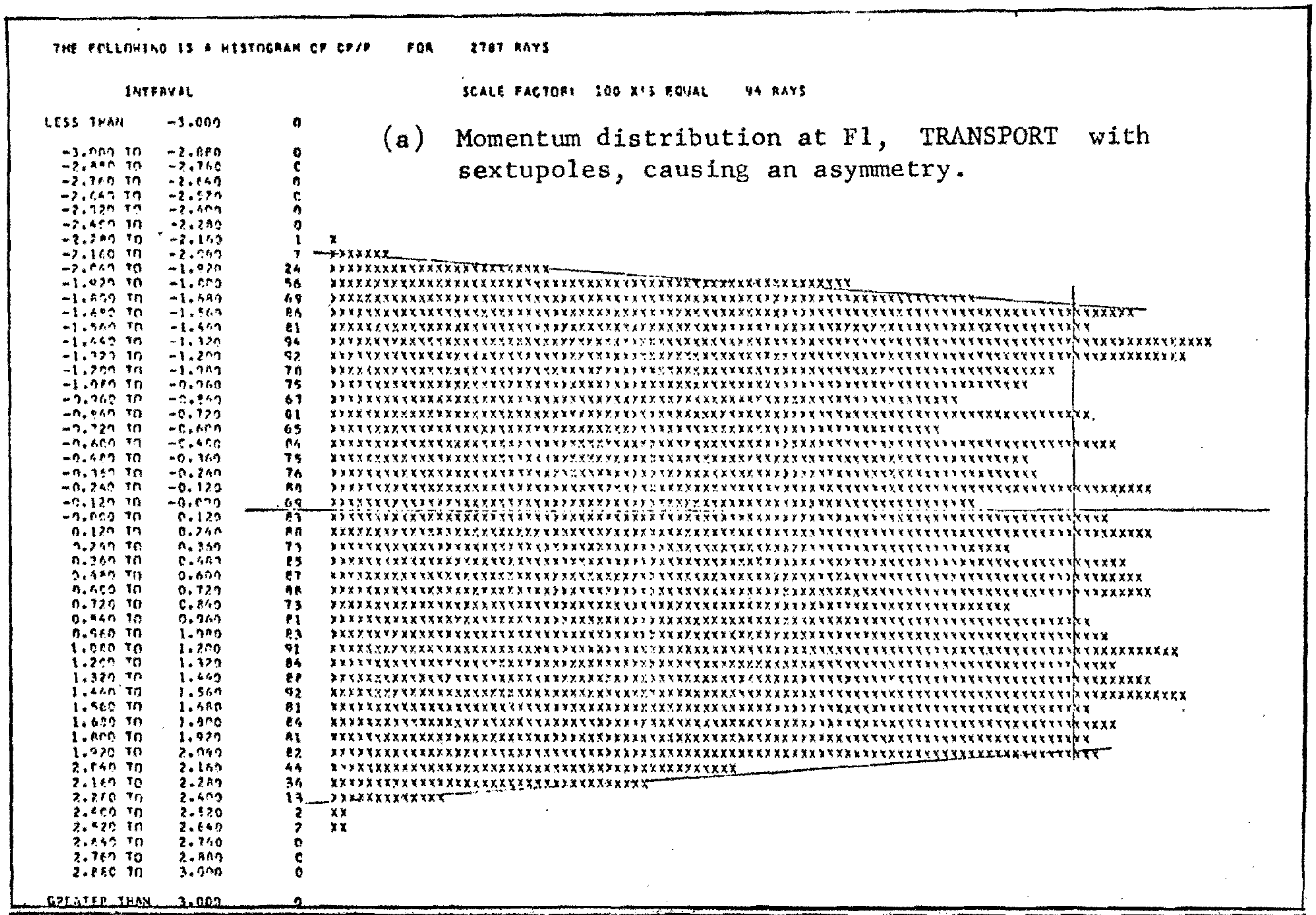

(a) Momentum distribution at F1, TRANSPORT with sextupoles, causing an asymmetry.

```
THE FOLLOWING IS A HISTOGRAM OF DP/P    FOR    2787 RAYS

          INTERVAL                          SCALE FACTOR:  100 X'S EQUAL    94 RAYS

LESS THAN     -3.000          0

   -3.000 TO    -2.880        0
   -2.880 TO    -2.760        0
   -2.760 TO    -2.640        0
   -2.640 TO    -2.520        0
   -2.520 TO    -2.400        0
   -2.400 TO    -2.280        0
   -2.280 TO    -2.160        1
   -2.160 TO    -2.040        7
   -2.040 TO    -1.920       24
   -1.920 TO    -1.800       56
   -1.800 TO    -1.680       69
   -1.680 TO    -1.560       86
   -1.560 TO    -1.440       81
   -1.440 TO    -1.320       94
   -1.320 TO    -1.200       92
   -1.200 TO    -1.080       70
   -1.080 TO    -0.960       75
   -0.960 TO    -0.840       67
   -0.840 TO    -0.720       81
   -0.720 TO    -0.600       65
   -0.600 TO    -0.480       84
   -0.480 TO    -0.360       75
   -0.360 TO    -0.240       76
   -0.240 TO    -0.120       88
   -0.120 TO    -0.000       69
   -0.000 TO     0.120       83
    0.120 TO     0.240       88
    0.240 TO     0.360       73
    0.360 TO     0.480       85
    0.480 TO     0.600       87
    0.600 TO     0.720       88
    0.720 TO     0.840       73
    0.840 TO     0.960       81
    0.960 TO     1.080       83
    1.080 TO     1.200       91
    1.200 TO     1.320       84
    1.320 TO     1.440       88
    1.440 TO     1.560       92
    1.560 TO     1.680       81
    1.680 TO     1.800       84
    1.800 TO     1.920       81
    1.920 TO     2.040       82
    2.040 TO     2.160       44
    2.160 TO     2.280       36
    2.280 TO     2.400       13
    2.400 TO     2.520        2
    2.520 TO     2.640        2
    2.640 TO     2.760        0
    2.760 TO     2.880        0
    2.880 TO     3.000        0

GREATER THAN   3.000          0
```

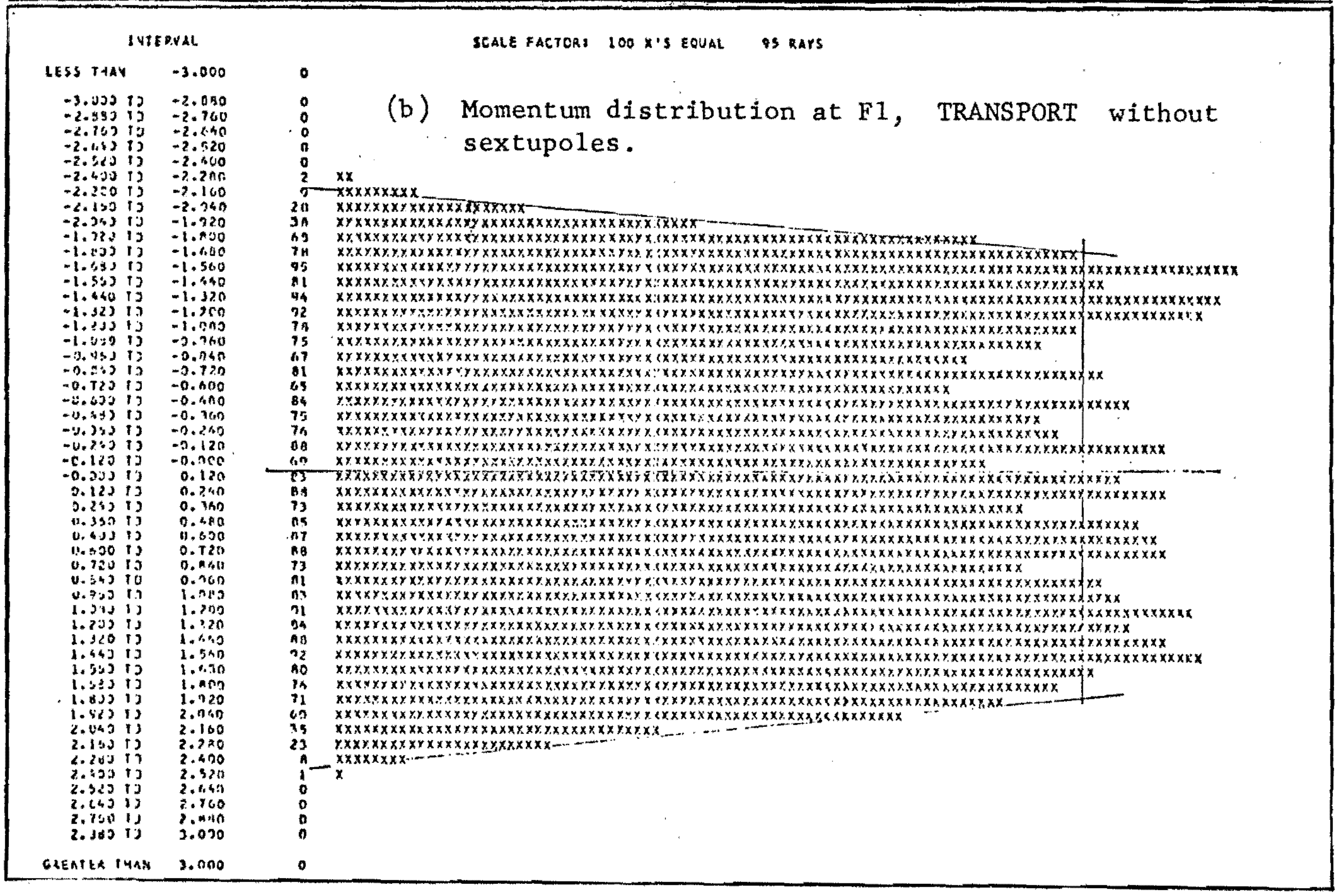

(b) Momentum distribution at F1, TRANSPORT without sextupoles.

```
          INTERVAL                          SCALE FACTOR:  100 X'S EQUAL    95 RAYS

LESS THAN     -3.000          0

   -3.000 TO    -2.880        0
   -2.880 TO    -2.760        0
   -2.760 TO    -2.640        0
   -2.640 TO    -2.520        0
   -2.520 TO    -2.400        0
   -2.400 TO    -2.280        2
   -2.280 TO    -2.160        9
   -2.160 TO    -2.040       20
   -2.040 TO    -1.920       38
   -1.920 TO    -1.800       69
   -1.800 TO    -1.680       78
   -1.680 TO    -1.560       95
   -1.560 TO    -1.440       81
   -1.440 TO    -1.320       94
   -1.320 TO    -1.200       92
   -1.200 TO    -1.080       78
   -1.080 TO    -0.960       75
   -0.960 TO    -0.840       67
   -0.840 TO    -0.720       81
   -0.720 TO    -0.600       65
   -0.600 TO    -0.480       84
   -0.480 TO    -0.360       75
   -0.360 TO    -0.240       76
   -0.240 TO    -0.120       88
   -0.120 TO    -0.000       69
   -0.000 TO     0.120       83
    0.120 TO     0.240       84
    0.240 TO     0.360       73
    0.360 TO     0.480       85
    0.480 TO     0.600       87
    0.600 TO     0.720       88
    0.720 TO     0.840       73
    0.840 TO     0.960       81
    0.960 TO     1.080       83
    1.080 TO     1.200       91
    1.200 TO     1.320       94
    1.320 TO     1.440       88
    1.440 TO     1.560       92
    1.560 TO     1.680       80
    1.680 TO     1.800       76
    1.800 TO     1.920       71
    1.920 TO     2.040       69
    2.040 TO     2.160       35
    2.160 TO     2.280       23
    2.280 TO     2.400        8
    2.400 TO     2.520        1
    2.520 TO     2.640        0
    2.640 TO     2.760        0
    2.760 TO     2.880        0
    2.880 TO     3.000        0

GREATER THAN   3.000          0
```

FIGURE 4

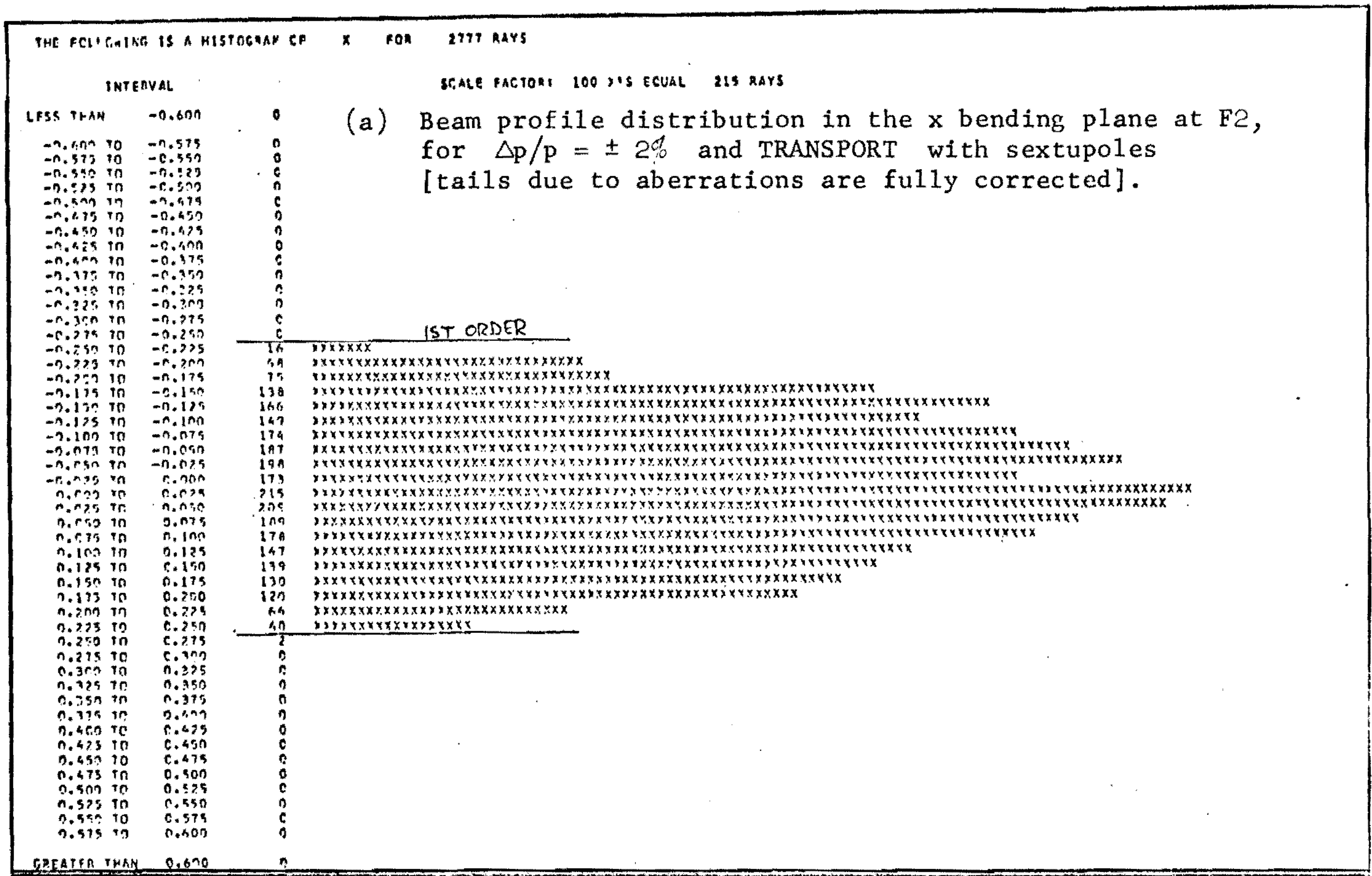

```
THE FOLLOWING IS A HISTOGRAM OF    X    FOR    2777 RAYS

      INTERVAL                          SCALE FACTOR:  100 X'S EQUAL   215 RAYS

LESS THAN      -0.600        0

  -0.600 TO    -0.575        0
  -0.575 TO    -0.550        0
  -0.550 TO    -0.525        0
  -0.525 TO    -0.500        0
  -0.500 TO    -0.475        0
  -0.475 TO    -0.450        0
  -0.450 TO    -0.425        0
  -0.425 TO    -0.400        0
  -0.400 TO    -0.375        0
  -0.375 TO    -0.350        0
  -0.350 TO    -0.325        0
  -0.325 TO    -0.300        0
  -0.300 TO    -0.275        0
  -0.275 TO    -0.250        0
  -0.250 TO    -0.225       16
  -0.225 TO    -0.200       68
  -0.200 TO    -0.175       75
  -0.175 TO    -0.150      138
  -0.150 TO    -0.125      166
  -0.125 TO    -0.100      147
  -0.100 TO    -0.075      174
  -0.075 TO    -0.050      187
  -0.050 TO    -0.025      198
  -0.025 TO     0.000      173
   0.000 TO     0.025      215
   0.025 TO     0.050      205
   0.050 TO     0.075      189
   0.075 TO     0.100      178
   0.100 TO     0.125      147
   0.125 TO     0.150      139
   0.150 TO     0.175      130
   0.175 TO     0.200      120
   0.200 TO     0.225       66
   0.225 TO     0.250       40
   0.250 TO     0.275        2
   0.275 TO     0.300        0
   0.300 TO     0.325        0
   0.325 TO     0.350        0
   0.350 TO     0.375        0
   0.375 TO     0.400        0
   0.400 TO     0.425        0
   0.425 TO     0.450        0
   0.450 TO     0.475        0
   0.475 TO     0.500        0
   0.500 TO     0.525        0
   0.525 TO     0.550        0
   0.550 TO     0.575        0
   0.575 TO     0.600        0

GREATER THAN    0.600        0
```

(a) Beam profile distribution in the x bending plane at F2, for Δp/p = ± 2% and TRANSPORT with sextupoles [tails due to aberrations are fully corrected].

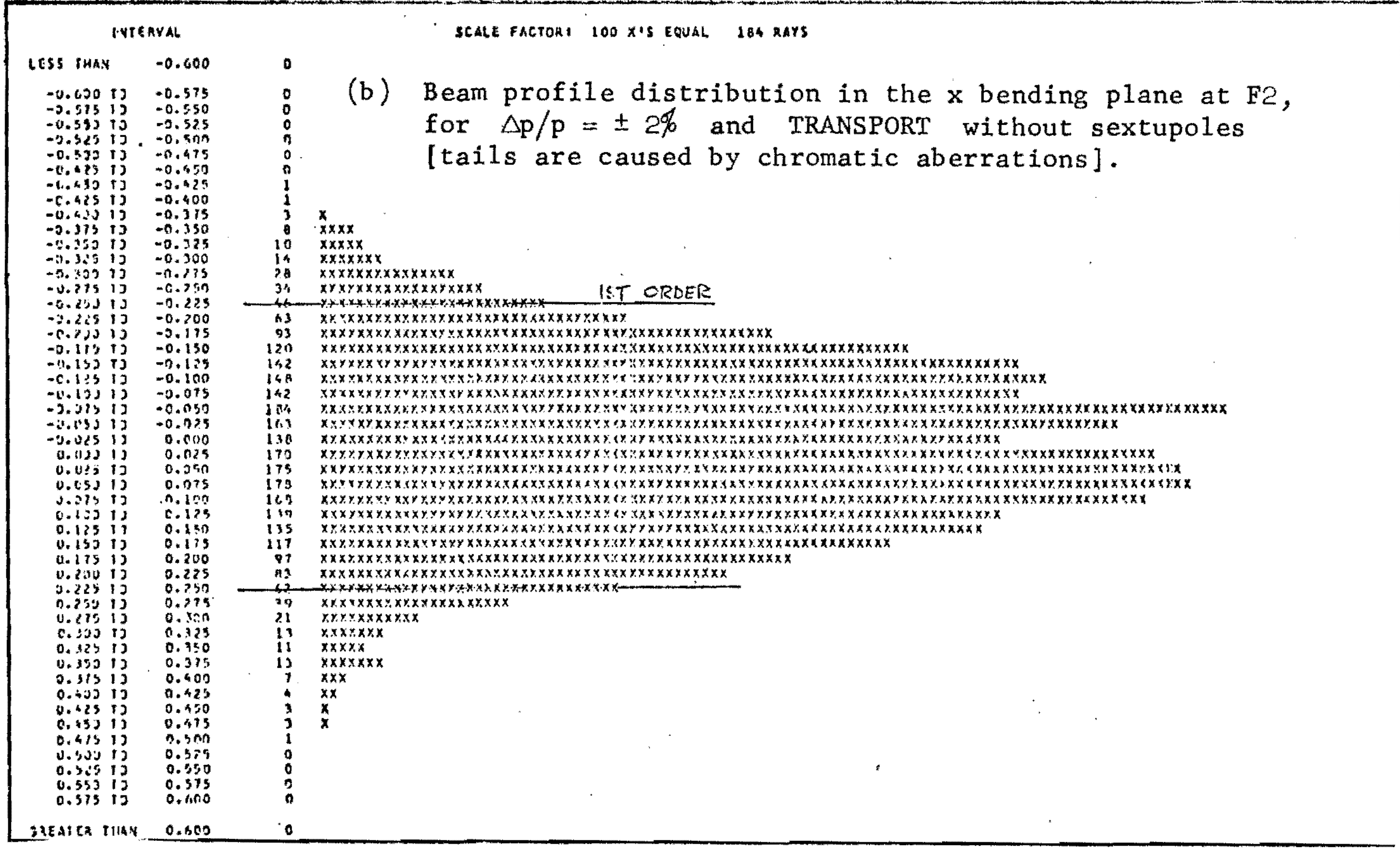

```
      INTERVAL                          SCALE FACTOR:  100 X'S EQUAL   184 RAYS

LESS THAN      -0.600        0

  -0.600 TO    -0.575        0
  -0.575 TO    -0.550        0
  -0.550 TO    -0.525        0
  -0.525 TO    -0.500        0
  -0.500 TO    -0.475        0
  -0.475 TO    -0.450        0
  -0.450 TO    -0.425        1
  -0.425 TO    -0.400        1
  -0.400 TO    -0.375        3
  -0.375 TO    -0.350        8
  -0.350 TO    -0.325       10
  -0.325 TO    -0.300       14
  -0.300 TO    -0.275       28
  -0.275 TO    -0.250       34
  -0.250 TO    -0.225       46
  -0.225 TO    -0.200       63
  -0.200 TO    -0.175       93
  -0.175 TO    -0.150      120
  -0.150 TO    -0.125      142
  -0.125 TO    -0.100      148
  -0.100 TO    -0.075      142
  -0.075 TO    -0.050      184
  -0.050 TO    -0.025      163
  -0.025 TO     0.000      130
   0.000 TO     0.025      170
   0.025 TO     0.050      175
   0.050 TO     0.075      178
   0.075 TO     0.100      165
   0.100 TO     0.125      139
   0.125 TO     0.150      135
   0.150 TO     0.175      117
   0.175 TO     0.200       97
   0.200 TO     0.225       83
   0.225 TO     0.250       62
   0.250 TO     0.275       39
   0.275 TO     0.300       21
   0.300 TO     0.325       13
   0.325 TO     0.350       11
   0.350 TO     0.375       13
   0.375 TO     0.400        7
   0.400 TO     0.425        4
   0.425 TO     0.450        3
   0.450 TO     0.475        3
   0.475 TO     0.500        1
   0.500 TO     0.525        0
   0.525 TO     0.550        0
   0.550 TO     0.575        0
   0.575 TO     0.600        0

GREATER THAN    0.600        0
```

(b) Beam profile distribution in the x bending plane at F2, for Δp/p = ± 2% and TRANSPORT without sextupoles [tails are caused by chromatic aberrations].

FIGURE 5

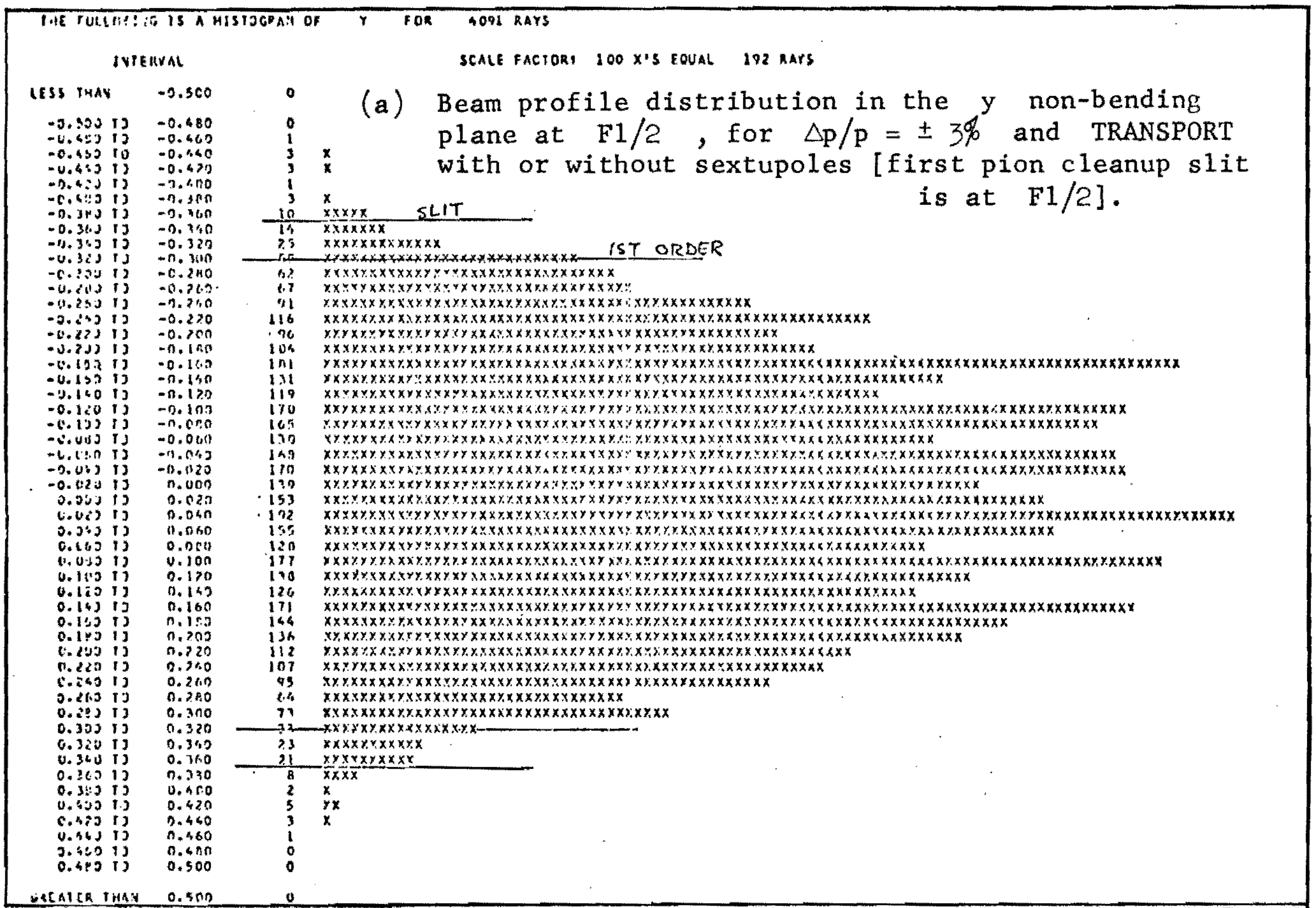

```
THE FOLLOWING IS A HISTOGRAM OF     Y     FOR     4091 RAYS

        INTERVAL                    SCALE FACTOR:  100 X'S EQUAL    192 RAYS

LESS THAN        -0.500        0

  -0.500 TO      -0.480        0
  -0.480 TO      -0.460        1
  -0.460 TO      -0.440        3
  -0.440 TO      -0.420        3
  -0.420 TO      -0.400        1
  -0.400 TO      -0.380        3
  -0.380 TO      -0.360       10
  -0.360 TO      -0.340       14
  -0.340 TO      -0.320       25
  -0.320 TO      -0.300       56
  -0.300 TO      -0.280       62
  -0.280 TO      -0.260       67
  -0.260 TO      -0.240       91
  -0.240 TO      -0.220      116
  -0.220 TO      -0.200       96
  -0.200 TO      -0.180      104
  -0.180 TO      -0.160      101
  -0.160 TO      -0.140      131
  -0.140 TO      -0.120      119
  -0.120 TO      -0.100      170
  -0.100 TO      -0.080      165
  -0.080 TO      -0.060      130
  -0.060 TO      -0.040      149
  -0.040 TO      -0.020      170
  -0.020 TO       0.000      139
   0.000 TO       0.020      153
   0.020 TO       0.040      192
   0.040 TO       0.060      155
   0.060 TO       0.080      120
   0.080 TO       0.100      177
   0.100 TO       0.120      130
   0.120 TO       0.140      126
   0.140 TO       0.160      171
   0.160 TO       0.180      144
   0.180 TO       0.200      136
   0.200 TO       0.220      112
   0.220 TO       0.240      107
   0.240 TO       0.260       95
   0.260 TO       0.280       64
   0.280 TO       0.300       71
   0.300 TO       0.320       33
   0.320 TO       0.340       23
   0.340 TO       0.360       21
   0.360 TO       0.380        8
   0.380 TO       0.400        2
   0.400 TO       0.420        5
   0.420 TO       0.440        3
   0.440 TO       0.460        1
   0.460 TO       0.480        0
   0.480 TO       0.500        0

GREATER THAN      0.500        0
```

(a) Beam profile distribution in the y non-bending plane at F1/2 , for Δp/p = ± 3% and TRANSPORT with or without sextupoles [first pion cleanup slit is at F1/2].

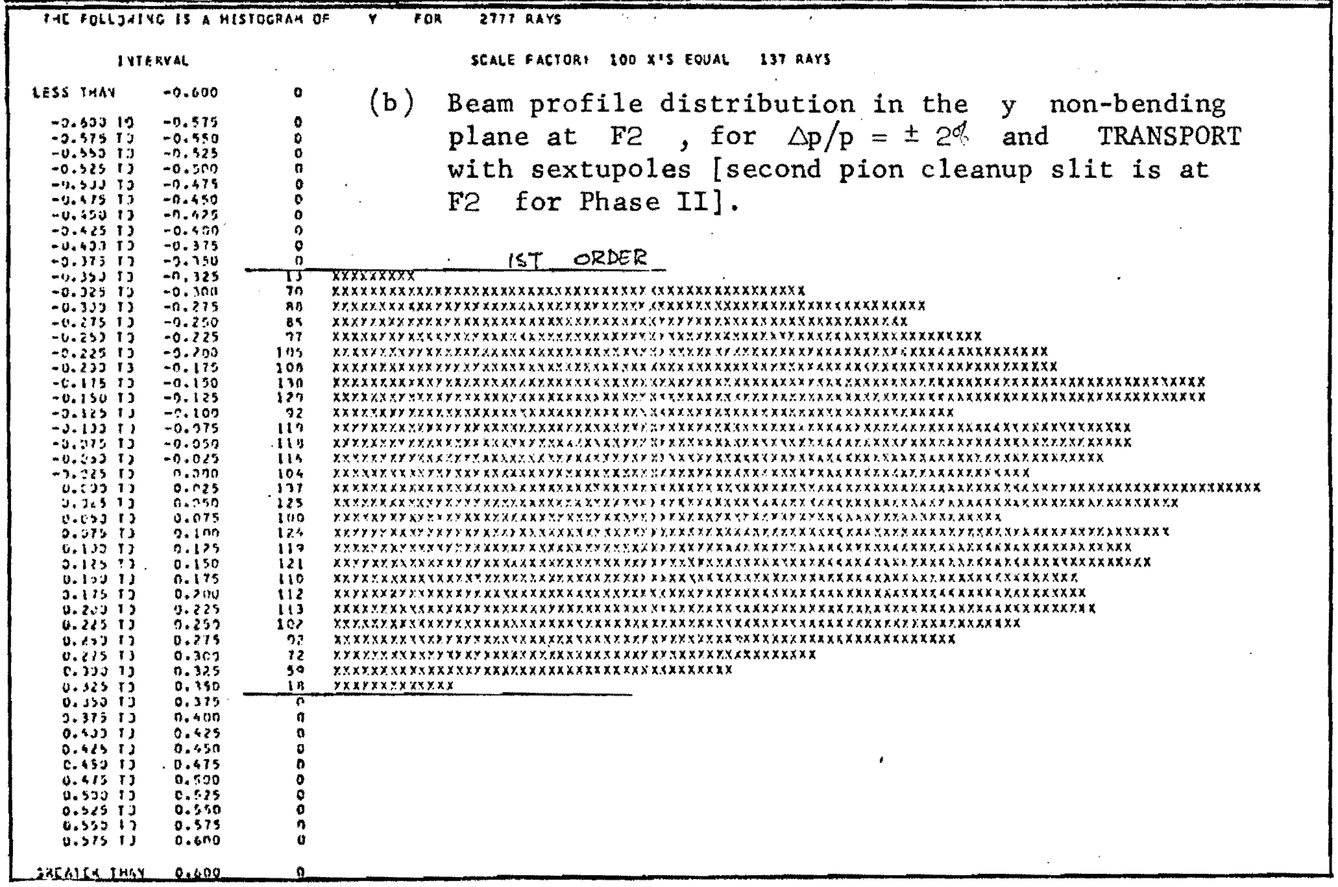

```
THE FOLLOWING IS A HISTOGRAM OF     Y     FOR     2777 RAYS

        INTERVAL                    SCALE FACTOR:  100 X'S EQUAL    137 RAYS

LESS THAN        -0.600        0

  -0.600 TO      -0.575        0
  -0.575 TO      -0.550        0
  -0.550 TO      -0.525        0
  -0.525 TO      -0.500        0
  -0.500 TO      -0.475        0
  -0.475 TO      -0.450        0
  -0.450 TO      -0.425        0
  -0.425 TO      -0.400        0
  -0.400 TO      -0.375        0
  -0.375 TO      -0.350        0
  -0.350 TO      -0.325       13
  -0.325 TO      -0.300       70
  -0.300 TO      -0.275       88
  -0.275 TO      -0.250       85
  -0.250 TO      -0.225       97
  -0.225 TO      -0.200      105
  -0.200 TO      -0.175      108
  -0.175 TO      -0.150      130
  -0.150 TO      -0.125      129
  -0.125 TO      -0.100       92
  -0.100 TO      -0.075      119
  -0.075 TO      -0.050      118
  -0.050 TO      -0.025      114
  -0.025 TO       0.000      104
   0.000 TO       0.025      137
   0.025 TO       0.050      125
   0.050 TO       0.075      100
   0.075 TO       0.100      124
   0.100 TO       0.125      119
   0.125 TO       0.150      121
   0.150 TO       0.175      110
   0.175 TO       0.200      112
   0.200 TO       0.225      113
   0.225 TO       0.250      107
   0.250 TO       0.275       92
   0.275 TO       0.300       72
   0.300 TO       0.325       59
   0.325 TO       0.350       18
   0.350 TO       0.375        0
   0.375 TO       0.400        0
   0.400 TO       0.425        0
   0.425 TO       0.450        0
   0.450 TO       0.475        0
   0.475 TO       0.500        0
   0.500 TO       0.525        0
   0.525 TO       0.550        0
   0.550 TO       0.575        0
   0.575 TO       0.600        0

GREATER THAN      0.600        0
```

(b) Beam profile distribution in the y non-bending plane at F2 , for Δp/p = ± 2% and TRANSPORT with sextupoles [second pion cleanup slit is at F2 for Phase II].

FIGURE 6